



Delft University of Technology

## Atrial fibrillation fingerprinting

Abdi, Bahareh

**DOI**

[10.4233/uuid:af53215c-69ea-4c18-8761-d5cf2c6e186](https://doi.org/10.4233/uuid:af53215c-69ea-4c18-8761-d5cf2c6e186)

**Publication date**

2021

**Document Version**

Final published version

**Citation (APA)**

Abdi, B. (2021). *Atrial fibrillation fingerprinting*. [Dissertation (TU Delft), Delft University of Technology]. <https://doi.org/10.4233/uuid:af53215c-69ea-4c18-8761-d5cf2c6e186>

**Important note**

To cite this publication, please use the final published version (if applicable).  
Please check the document version above.

**Copyright**

Other than for strictly personal use, it is not permitted to download, forward or distribute the text or part of it, without the consent of the author(s) and/or copyright holder(s), unless the work is under an open content license such as Creative Commons.

**Takedown policy**

Please contact us and provide details if you believe this document breaches copyrights.  
We will remove access to the work immediately and investigate your claim.

# **ATRIAL FIBRILLATION FINGERPRINTING**



# **ATRIAL FIBRILLATION FINGERPRINTING**

## **Proefschrift**

ter verkrijging van de graad van doctor  
aan de Technische Universiteit Delft,  
op gezag van de Rector Magnificus, prof. dr. ir. T.H.J.J. van der Hagen,  
voorzitter van het College voor Promoties,  
in het openbaar te verdedigen op woensdag 27 oktober 2021 om 12:30 uur

door

**Bahareh ABDIKIVANANI**

Master of Science in Biomedical Engineering,  
University of Tehran, Tehran, Iran,  
geboren te Tehran, Iran.

Dit proefschrift is goedgekeurd door de promotoren.

Samenstelling promotiecommissie bestaat uit:

Rector Magnificus,	voorzitter
Dr. ir. R. C. Hendriks,	Technische Universiteit Delft, promotor
Prof. dr. ir. A. J. van der Veen,	Technische Universiteit Delft, promotor
Prof. dr. N. M.S. de Groot,	Erasmus University Medical Center,
	Technische Universiteit Delft, promotor

*Onafhankelijke leden:*

Dr. J.M.H.Karel	Maastricht University
Prof. dr. J.-M. Vesin	École polytechnique fédérale de Lausanne, Zwitserland
Prof. dr. V. Zarzoso	Université Côte d'Azur, Frankrijk
Prof. dr. ir. W.A. Serdijn	Technische Universiteit Delft
Prof. dr. ir. G.J.T. Leus	Technische Universiteit Delft, reservelid



*Acknowledgement:* This research has been made possible by the Dutch Heart Foundation and the Netherlands Organization for Scientific Research (NWO), as part of their joint strategic research program: "Earlier recognition of cardiovascular diseases". This project is partially financed by the PPP Allowance made available by Top Sector Life Sciences & Health to the Dutch Heart Foundation to stimulate public-private partnerships.

*Keywords:* atrial fibrillation, atrial electrograms, atrial mapping, fractionation, local activation time estimation, electrogram model, transmembrane current, conductivity estimation, electrophysiological model, inverse problem, reaction-diffusion equation, deconvolution, electrode size, electrogram morphology, activation map, electrogram interpolation.

Copyright © 2021 by B. Abdikivanani

ISBN 978-94-6384-260-0

An electronic version of this dissertation is available at  
<http://repository.tudelft.nl/>.

*To my family*



# CONTENTS

<b>Summary</b>	<b>xi</b>
<b>Samenvatting</b>	<b>xiii</b>
<b>1 Introduction</b>	<b>1</b>
1.1 Research motivation . . . . .	1
1.2 Research objectives . . . . .	2
1.3 Dissertation Outline and Contribution. . . . .	3
1.3.1 Chapter 2: Background and Fundamentals . . . . .	4
1.3.2 Chapter 3: Ventricular activity removal . . . . .	4
1.3.3 Chapter 4: A compact matrix model for atrial electrograms for tissue conductivity estimation . . . . .	4
1.3.4 Chapter 5: Improved local activation time annotation of fractionated atrial electrograms for atrial mapping . . . . .	5
1.3.5 Chapter 6: Analyzing the Effect of Electrode Size on Electrogram and Activation Map Properties . . . . .	5
1.3.6 Chapter 7: Conclusion . . . . .	6
1.4 List of Papers. . . . .	6
<b>2 Background and Fundamentals</b>	<b>9</b>
2.1 The heart and Its Physiology . . . . .	9
2.1.1 The Heart . . . . .	9
2.1.2 Cardiac Conduction System . . . . .	9
2.1.3 Measuring the Heart Electrical Activity . . . . .	10
2.2 Atrial fibrillation . . . . .	12
2.2.1 What is Atrial Fibrillation? . . . . .	12
2.2.2 Pathophysiological mechanisms underlying AF . . . . .	13
2.2.3 AF treatment: Ablation . . . . .	14
2.3 Atrial Mapping and electrogram recording . . . . .	15
2.4 EGM pre-processing and analysis. . . . .	15
2.4.1 EGM Preprocessing . . . . .	15
2.4.2 Electrogram Analysis . . . . .	16
2.5 AP and EGM models . . . . .	19
2.5.1 Action Potential Model. . . . .	19
2.5.2 Action Potential Propagation Model . . . . .	20
2.5.3 Electrogram Model . . . . .	21
2.5.4 Simulated tissue and Activation Maps . . . . .	22
2.5.5 Developing a Simplified Electrogram Model . . . . .	23

<b>3</b>	<b>Ventricular activity removal</b>	<b>25</b>
3.1	Introduction . . . . .	25
3.2	Method . . . . .	26
3.2.1	Electrogram Model . . . . .	26
3.2.2	Data Matrix Formation . . . . .	27
3.2.3	VA and AA Separation . . . . .	27
3.3	Results . . . . .	29
3.3.1	Experiments on Clinical Data . . . . .	30
3.3.2	Performance Evaluation . . . . .	30
3.4	Conclusion . . . . .	33
<b>4</b>	<b>A compact matrix model for atrial electrograms for tissue conductivity estimation</b>	<b>35</b>
4.1	Introduction . . . . .	35
4.2	Electrogram Model . . . . .	37
4.2.1	Action Potential Propagation and Electrogram Models . . . . .	37
4.2.2	Simplified Electrogram Model . . . . .	38
4.2.3	Compact Matrix Model for Electrograms Based on Conductivity . . . . .	39
4.3	Conductivity Estimation . . . . .	40
4.4	Simulation Results . . . . .	42
4.5	Experiments on Clinical Data . . . . .	46
4.6	Discussion and Conclusions . . . . .	48
<b>5</b>	<b>Improved local activation time annotation of fractionated electrograms</b>	<b>51</b>
5.1	Introduction . . . . .	52
5.2	Method . . . . .	53
5.2.1	Action Potential Propagation . . . . .	53
5.2.2	Electrogram Model . . . . .	53
5.2.3	Transmembrane Current Estimation . . . . .	54
5.3	Simulation Results . . . . .	56
5.3.1	Strategies for generation of fractionated electrograms . . . . .	56
5.3.2	Transmembrane Currents . . . . .	58
5.3.3	LAT estimation . . . . .	60
5.3.4	Electrode height $z_0$ . . . . .	61
5.3.5	Spatial sampling resolution . . . . .	63
5.3.6	Electrode size . . . . .	65
5.3.7	Regularization Parameter $\lambda$ . . . . .	65
5.4	Clinical Results . . . . .	66
5.4.1	Turning a smooth propagation into a non-smooth propagation . . . . .	67
5.4.2	Changing the location of the line of collision or (functional) conduction block . . . . .	67
5.4.3	Introduction of more distinct wavefronts in the mapping area . . . . .	69
5.4.4	Providing more consistent maps over succeeding beats . . . . .	70

---

5.5	<b>Discussion and Conclusion . . . . .</b>	70
5.5.1	<b>Summary . . . . .</b>	70
5.5.2	<b>Limitations of the proposed method. . . . .</b>	71
5.5.3	<b>Future Work . . . . .</b>	71
<b>6</b>	<b>Analysing the Effect of Electrode Size on Electrogram and Activation Map Properties</b>	<b>73</b>
6.1	<b>Introduction . . . . .</b>	74
6.2	<b>Method. . . . .</b>	75
6.2.1	<b>Atrial tissue computer model . . . . .</b>	75
6.2.2	<b>Electrode's transfer function model . . . . .</b>	76
6.2.3	<b>Modeling abnormal tissue . . . . .</b>	77
6.2.4	<b>Clinical Studies . . . . .</b>	79
6.2.5	<b>Electrogram analysis . . . . .</b>	80
6.3	<b>Simulation Results . . . . .</b>	81
6.3.1	<b>Effect of electrode size on electrogram properties . . . . .</b>	81
6.3.2	<b>Effect of electrode size on the activation map . . . . .</b>	83
6.3.3	<b>Optimal electrode diameter and inter-electrode distance . . . . .</b>	84
6.3.4	<b>Maximum electrode size for recording scarred tissue . . . . .</b>	85
6.4	<b>Clinical Results . . . . .</b>	86
6.4.1	<b>Statistical analysis . . . . .</b>	87
6.4.2	<b>changes in activation maps . . . . .</b>	88
6.4.3	<b>Scaling electrograms' amplitude . . . . .</b>	88
6.5	<b>Discussion and Conclusion . . . . .</b>	89
6.5.1	<b>Study limitations . . . . .</b>	90
<b>7</b>	<b>Conclusion</b>	<b>93</b>
7.1	<b>Conclusion . . . . .</b>	93
7.1.1	<b>Simplified electrogram model for tissue parameter estimation . . . . .</b>	93
7.1.2	<b>Estimation of underlying tissue parameters . . . . .</b>	94
7.1.3	<b>The effect of electrode size on electrogram properties . . . . .</b>	95
7.2	<b>Study Limitations and Future Work . . . . .</b>	96
7.3	<b>Closing Remarks . . . . .</b>	98
	<b>References . . . . .</b>	101
	<b>Acknowledgements</b>	<b>111</b>
	<b>Curriculum Vitæ</b>	<b>113</b>



# SUMMARY

Atrial fibrillation (AF) is a common age-related cardiac arrhythmia. AF is characterized by rapid and irregular electrical activity of the heart leading to a higher risk of stroke and heart failure. During AF, the upper chambers of the heart, called atria, experience chaotic electrical wave propagation. However, despite the various mechanisms introduced in the literature, there is still an ongoing debate on a precise and consistent mechanism underlying the initiation and perpetuation of AF. Some studies show that AF is rooted in impaired electrical conduction and structural damage of atrial tissue, known as electropathology. Atrial electrograms (EGMs) recorded directly from heart's surface, provide an important diagnostic tool to localize and quantify the degree of electropathology in the tissue. However, the analysis of the electrograms is currently constrained by the lack of suitable methods that can reveal the hidden electrophysiological parameters of the tissue. These parameters can be used as local indication of electropathology in the tissue.

We believe that understanding AF and improving AF therapy starts with developing a proper forward model that is accurate enough (from a physiological point of view) and simultaneously simple enough to allow for subsequent parameter estimation. Therefore, the main focus of this thesis is on developing a simplified forward model that can efficiently explain the observed EGM based on AF relevant tissue parameters.

An initial step before performing any analysis on the data is to remove noise and artefacts. All atrial electrogram recordings suffer from strong far-field ventricular activities (VA). Therefore, as the first step, we propose a new framework for removal of VA from atrial electrograms, which is based on interpolation and subtraction followed by low-rank and sparse matrix decomposition. The proposed framework is of low complexity, does not require high resolution multi-channel recordings, or a calibration step for each individual patient.

In the next step, we develop a simplified electrogram model. We represent the model in a compact matrix form and show its linear dependence on the conductivity vector, enabling the estimation of this parameter from the recorded electrograms. The results show that despite the low resolution and all simplifying assumptions, the model can efficiently estimate the conductivity map and regenerate realistic electrograms, especially during sinus rhythm.

In the next contribution of this dissertation, we propose a new approach for a better estimation of local activation times for atrial mapping by reducing the spatial blurring effect that is inherent to electrogram recordings using deconvolution. Employing sparsity based regularization and first-order time derivatives in formulating the deconvolution problem, improved performance of transmembrane current estimation is obtained.

In the final part, we focus on translating our findings from research to clinical application. Therefore, we studied the effect of electrode size on electrogram properties including the length of the block line observed on the resulting activation map, percentage of observed low voltage areas, percentage of electrograms with low maximum steepness, and the number of deflections in the recorded electrograms.



# SAMENVATTING

Atriumfibrilleren (AF, ook wel boezemfibrilleren genoemd) is een veelvoorkomende leeftijdsgerelateerde hartritmestoornis. AF wordt gekarakteriseerd door snelle en onregelmatige elektrische activiteit van het hart en geeft een hogere kans op een beroerte (herseninfarct) en hartfalen. Tijdens AF vertonen de bovenste kamers van het hart (de atria) een chaotische elektrische golfgeleiding. Verschillende mechanismen worden in de literatuur beschreven. Desondanks is er nog steeds discussie over een nauwkeurig en consistent mechanisme dat ten grondslag ligt aan de initiatie en bestendiging van AF. Sommige onderzoeken tonen aan dat AF gebaseerd is op een verminderde elektrische geleiding en structurele schade aan atriumweefsel, bekend als elektropathologie. Atriale elektrogrammen (EGM's) die direct op het hartoppervlak worden opgenomen, bieden een belangrijk diagnostisch hulpmiddel om de mate van elektropathologie in het weefsel te bepalen en te lokaliseren. De analyse van elektrogrammen wordt momenteel echter beperkt door een gebrek aan geschikte methoden om de onderliggende elektrofisiologische parameters van het weefsel te schatten. Deze parameters kunnen worden gebruikt als een lokale indicatie van de elektropathologie van het weefsel.

Wij menen dat het begrijpen van AF en het verbeteren van AF-therapie begint bij het ontwikkelen van een wiskundig voorwaarts model dat nauwkeurig genoeg is (vanuit fysiologisch oogpunt) en tegelijkertijd eenvoudig genoeg om een latere parameterschatting mogelijk te maken. Daarom is de belangrijkste focus van dit proefschrift gericht op het ontwikkelen van een vereenvoudigd voorwaarts model dat efficiënt de waargenomen EGM kan verklaren op basis van AF-relevante weefselparameters.

Voordat een analyse van de gegevens wordt uitgevoerd, is een eerste stap het verwijderen van ruis en artefacten. Alle atriale elektrogramregistraties hebben last van sterke verreeld ventriculaire activiteiten (VA). Daarom stellen we als eerste stap een nieuw raamwerk voor voor het verwijderen van VA uit atriale elektrogrammen, gebaseerd op interpolatie en aftrekking gevolgd door bepaalde lage-rangs matrixontbindingen. Het voorgestelde algoritme heeft een lage complexiteit en heeft geen hoge-resolutie meerkanaalsopnames nodig, of een kalibratiestap voor elke individuele patient.

In de volgende stap ontwikkelen we een vereenvoudigd elektrogrammodel. We gieten het model in een compacte matrixvorm die de lineaire afhankelijkheid van de geleidbaarheidsvector zichtbaar maakt, waardoor de schatting van deze parameter uit de opgenomen elektrogrammen mogelijk wordt. De resultaten laten zien dat ondanks de lage resolutie en alle vereenvoudigingen het model efficiënt de geleidbaarheidskaart kan schatten en realistische elektrogrammen kan regenereren, vooral tijdens sinusritme.

Vervolgens richten we ons op een nieuwe en betere aanpak voor de schatting van de lokale activeringstijden in EGM's. Het probleem hierbij is dat bij het opnemen van elektrogrammen deze vervaagd worden door een convolutie met een (ruimtelijk) laagdoorlaatfilter. Het onderliggende deconvolutieprobleem kan geformuleerd worden met behulp van op sparsity gebaseerde regularisatie en eerste-orde tijdsafgeleiden, en hierdoor wordt een

betere schatting van de transmembraanstroom verkregen.

In het laatste deel richten we ons op het vertalen van onze bevindingen naar klinische toepassingen. Hiertoe hebben we het effect van de elektrode grootte op elektrogrammeigenschappen bestudeerd, waaronder de lengte van de blokkades waargenomen in de resulterende activeringskaart, het percentage waargenomen gebieden met lage spanningen, het percentage elektrogrammen met een lage maximale steilheid, en het aantal deflecties in de opgenomen elektrogrammen.

# 1

## INTRODUCTION

### 1.1. RESEARCH MOTIVATION

The heart is a muscular organ that pumps blood containing oxygen and nutrients throughout the body in each cardiac cycle or heartbeat. The number of heartbeats per minute (i.e., the speed of the heartbeat) is called heart rate. A group of conditions known as cardiac arrhythmia can affect the heart normal activity. As a result, the heart might beat faster, slower or irregular. In general, cardiac arrhythmia refers to any abnormality in the heart rate or heart rhythm and ranges from harmless disorders to potentially fatal problems, including cardiac arrest and stroke.

A common age-related type of arrhythmia is atrial fibrillation (AF). AF originates from the atria, the upper chambers of the heart, and causes irregular and often rapid heart beats. Initially, patients experience short episodes of AF that come and go. However, due to the progressive nature of AF, typically the frequency as well as the episode length increase, which increases the chance of stroke and heart failure [1]. Patients with AF have five times higher risk of strokes, especially ischemic stroke with higher death rate [2, 3].

In a normal heart, the electrical activity that causes the heart muscles to contract, is initiated by the sinoatrial (SA) node. The generated activity then propagates throughout the whole atria in regular pathways and then reaches the atrioventricular (AV) node. After a short delay in the AV node, the electrical impulses propagate through the ventricles, the lower heart chambers, and causes them to contract and to pump the blood throughout the body [4]. However, during atrial fibrillation the regular cardiac conduction pathways are disrupted and as a result the electrical wave breaks into several smaller waves that propagate in highly irregular patterns. Once one of these waves reaches the AV node, it initiates ventricular activation. This results in the irregular and often rapid heart beats observed in AF patients [5].

Although many studies have investigated the pathological mechanisms that are responsible for the initiation and the maintenance of AF [6–9], its main cause(s) are not yet completely discovered. Most common pathological mechanisms that can explain the initiation and maintenance of AF to some extent are: ectopic foci, reentry, rotor, breakthroughs, and multiple wavelets [6].

The inhomogeneity and complexity in defining the causes of AF consequently hampers the success rate of atrial fibrillation treatments, ranging from medication to surgical intervention.

Some studies have shown that the development and progression of AF is rooted in impaired electrical conduction and structural damage of atrial tissue, known as electropathology [5, 10]. Gaining more understanding on the electropathology starts with studying electrical wave propagation in the atrial tissue. The recording of atrial electrical activity can be done through atrial mapping. Atrial mapping provides a strong diagnostic tool to investigate the wave propagation in the tissue. During this procedure, an array of electrodes is positioned on the heart surface to record the electrical activity of the heart. The resulting signal per electrode is called an electrogram. As shown in previous studies, electrograms can help to localize and quantify the degree of electropathology and to stage AF [5, 10, 11].

However, the analysis of electrograms is currently constrained by the lack of suitable methods that can reveal the hidden electrophysiological parameters of the tissue. These parameters can be used as a local indication of electropathology in the tissue. Currently, cardiologists mostly analyze the electrical propagation and electropathology based on local activation times (LATs) and local conduction velocities (CVs), defined as the distance traveled by the depolarization wavefront in a unit of time. However, the interpretation of these propagations, due to the interaction of many parameters, is quite complex, needs expert intervention, and is time varying (from beat-to-beat during AF). The changes in CVs may have multiple causes of both pathologic and non-pathologic origin; even pathological causes might not be local and might originate from a different area in the atrium.

The electrical propagation in the tissue is governed by electrophysiological models and is directly connected to its underlying parameters [12]. Many studies have successfully employed these detailed models to show the effect of tissue properties like anisotropy and heterogeneity on the resulting electrograms [13, 14]. However, using such models in the inverse problem of extracting tissue properties from electrograms is nearly impossible due to the complexity of these models and the large number of parameters that need to be estimated.

Our hypothesis is that understanding atrial fibrillation and improving AF therapy starts by developing a proper forward model that is accurate enough (from a physiological point of view) and simultaneously simple enough to allow for subsequent parameter estimation. The main focus of this study is, therefore, to develop a simplified forward model that can efficiently explain the observed electrogram morphology based on the tissue properties, and its application in estimating such parameters. These parameters, which are indicators of electropathology, can potentially unravel the mechanisms underlying atrial fibrillation.

## 1.2. RESEARCH OBJECTIVES

The studies presented in this dissertation are done as part of "Atrial Fibrillation Finger-Printing: Spotting bio-electrical markers to early recognize atrial fibrillation by the use of a bottom-up approach (AFFIP)" project. This project, carried out by a multidisciplinary team involving medical doctors, technical engineers and molecular biologists, thereby enables integration of basic, translational and technological science into daily clinical practice. The main goal of this project is to develop age and gender based, bio-electrical diagnostic tests, the invasive and non-invasive AF Fingerprint, which consists of electrical atrial signal

profiles and levels of atrial specific tissue/blood biomarkers. In daily clinical practice, this novel diagnostic instrument can be used for early recognition or progression of AF by determination of the stage of the electropathology. As such, AF Fingerprinting enables optimal AF treatment, thereby improving patients' outcome.

As part of the AFFIP project, the studies in this dissertation are done towards our final goal of early recognition or progression of AF. Many other studies, e.g. [6, 7, 9, 15, 16], also focus on this goal. However, despite the improvements made and the various mechanisms introduced, there is still an ongoing debate on a precise and consistent mechanism. Our main focus, however, is to provide a better understanding of atrial fibrillation by providing signal processing algorithms for analyzing wave propagation and electrogram generation in the atrial tissue.

We believe that in order to provide a better understanding of AF, we need to start with the electrophysiological models that govern the electrical wave propagation in the atrial tissue. By analyzing these models and estimating their underlying parameters, we can identify and investigate electropathological mechanisms that disrupt normal wave propagation in the tissue. However, application of the detailed and precise models that are already introduced in literature, e.g. [13, 14], in inverse problems that aim to estimate AF relevant tissue parameters, is nearly impossible. This is due to the large number of unknown parameters and nonlinear dependencies of electrograms on these parameters.

To overcome these issues, we narrowed down the focus of this dissertation in order to answer the following research questions:

**Q1.** Can we simplify the underlying electrophysiological models of electrograms to facilitate accurate tissue parameter estimation using well-known signal processing approaches?

Subsequently, we would like to know whether we can use such a simplified model for estimation of underlying tissue properties. This has led to two more specific questions focusing on two important parameters: conductivity and LATs, as:

**Q2.1.** Can we use these simplified models for the estimation of tissue conductivity?

**Q2.2.** Can we use these models for a better estimation of LAT in fractionated electrograms?

As the next step, we are interested in translating our findings from research to clinical application. Therefore, we pose the following question that is of high importance in clinical applications:

**Q3.** Can we use the electrogram model to simulate clinical electrograms recorded by different electrode sizes and use them to analyze the effect of the electrode size on electrogram properties?

Although providing an answer to these questions will not bring us to our final goal of early recognition or progression of AF, they are the initial steps towards our goal.

### 1.3. DISSERTATION OUTLINE AND CONTRIBUTION

In this section, we present the outline of this dissertation and summarize its contributions per chapter. A summary of these contributions is also shown in Fig. 1.1. To answer the research questions discussed in Section 1.2, we start with EGM recordings and move towards our final goal, which is analysing electropathology as a mechanism underlying AF.

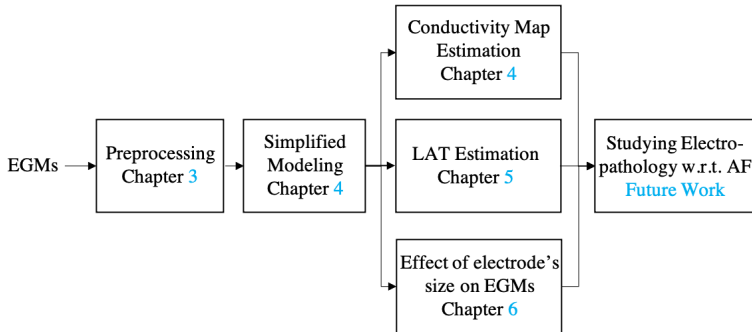


Figure 1.1: Analysing EGM recordings for studying electrophysiological mechanisms underlying atrial fibrillation, based on the contributions of this dissertation.

### 1.3.1. CHAPTER 2: BACKGROUND AND FUNDAMENTALS

In this chapter we provide the background necessary for reading this dissertation. We start with a brief review of the heart physiology and anatomy, its electrical conduction system, and diagnostic tools to measure its electrical activity. Next, we introduce atrial fibrillation, the pathological mechanisms underlying atrial fibrillation, and its treatments. Furthermore, we discuss the atrial mapping and electrogram recording procedure in clinical setting. We provide a review of the preprocessing approaches performed on electrograms and finally provide a review of the electrophysiological models for action potential propagation and electrogram arrays.

### 1.3.2. CHAPTER 3: VENTRICULAR ACTIVITY REMOVAL

In this chapter, we develop a framework for removing ventricular activities (VAs) from the recorded unipolar electrogram while preserving the components with atrial activity (AA). We first remove the VA-containing segments and interpolates the remaining samples. This will also partly remove the atrial components that overlap with VA signals, e.g., during atrial fibrillation. To reconstruct the AA components, we estimate them from the removed VA-containing segments based on a low-rank and sparse matrix decomposition and add them back to the electrograms. The presented framework is of rather low complexity, preserves AA components, and requires only a single EGM recording. Instrumental comparison to template matching and subtraction and independent component analysis shows that the proposed approach leads to smoother results with better similarity to the true atrial signal. Although this does not answer any of our research questions, it is a necessary step before performing any analysis on the data.

### 1.3.3. CHAPTER 4: A COMPACT MATRIX MODEL FOR ATRIAL ELECTROGRAMS FOR TISSUE CONDUCTIVITY ESTIMATION

To answer research questions Q1 and Q2.1, we first develop in this chapter a simple but effective forward model to replace the computationally intensive reaction-diffusion equations that we will discuss in Chapter 4 governing the electrical propagation in tissue. Using this simplified model, we present a compact matrix model for electrograms including conduc-

tivity. Subsequently, we exploit the simplicity of the compact model to solve the ill-posed inverse problem of estimating tissue conductivity. The algorithm is demonstrated on simulated data as well as on clinically recorded data. The results show that the model allows to efficiently estimate the conductivity map. In addition, based on the estimated conductivity, realistic electrograms (limited to 2D tissue) can be regenerated demonstrating the validity of the model.

### **1.3.4. CHAPTER 5: IMPROVED LOCAL ACTIVATION TIME ANNOTATION OF FRACTIONATED ATRIAL ELECTROGRAMS FOR ATRIAL MAPPING**

To answer research question Q2.2, we exploit in this chapter multi-electrode electrogram recordings to amplify the local activity in each electrogram and subsequently improve the annotation of LATs. An electrogram array can be modeled as a spatial convolution of per cell transmembrane currents with an appropriate distance kernel, which depends on the cells' distances to the electrodes. By deconvolving the effect of the distance kernel from the electrogram array, we undo the blurring and estimate the underlying transmembrane currents as our desired local activities. However, deconvolution problems are typically highly ill-posed and result in unstable solutions. To overcome this issue, we propose to use a regularization term that exploits the sparsity of the first-order time derivative of the transmembrane currents. We perform experiments on simulated two-dimensional tissues, as well as clinically recorded electrograms during paroxysmal atrial fibrillation. The results show that the proposed approach for deconvolution can improve the annotation of the true LAT in the electrograms. We also discuss, in summary, the required electrode array specifications for an appropriate recording and subsequent deconvolution. By ignoring small but local deflections, algorithms based on steepest descent are prone to generate smoother activation maps. However, by exploiting multi-electrode recordings, we can efficiently amplify small but local deflections and reveal new details in the activation maps that were previously missed.

### **1.3.5. CHAPTER 6: ANALYZING THE EFFECT OF ELECTRODE SIZE ON ELECTROGRAM AND ACTIVATION MAP PROPERTIES**

To answer research question Q3, we use in this chapter, the electrode transfer function to model and analyze the effect of electrode size on the properties of measured electrograms. To do so, we use both simulated as well as clinical data. To simulate electrogram arrays we use a two-dimensional (2D) electrogram model as well as an action potential propagation model. For clinical data, however, we first estimate the transmembrane current for a higher resolution 2D modeled cell grid and later use these values to model electrograms with different electrode sizes. We simulate electrogram arrays for 2D tissues with 3 different levels of heterogeneity in the conduction and stimulation pattern to model the inhomogeneous wave propagation observed during atrial fibrillation. Five measures are used to characterize the properties of the simulated electrogram arrays of different electrode sizes. The results show that increasing the electrode size increases the error in LAT estimation and decreases the estimated length of conduction block lines. Moreover, visual inspection also shows that the activation maps generated by larger electrodes are more homogeneous with a lower

number of observed wavelets. The increase in electrode size also increases the low voltage areas in the tissue while decreasing the maximum steepness of the atrial activities and the number of detected deflections. The effect is more pronounced for tissue with higher level of heterogeneities in the conduction pattern. Similar conclusions hold for the measures performed on clinical data. The electrode size affects the properties of recorded electrogram arrays, which can subsequently complicate our understanding of atrial fibrillation. This needs to be considered while performing any analysis on the electrograms or comparing the results of different electrogram arrays.

### 1.3.6. CHAPTER 7: CONCLUSION

In this chapter, we conclude this dissertation by summarizing our contributions and discussing some practical open questions and our suggested approach for addressing these challenges.

## 1.4. LIST OF PAPERS

In this section, all papers submitted and published during the course of this PhD project are listed.

### JOURNALS

1. **B. Abdi**, R.C. Hendriks, A.-J. van der Veen, N.M. de Groot, *A compact matrix model for atrial electrograms for tissue conductivity estimation*, Journal of Computers in Medicine and Biology (2019).
2. **B. Abdi**, R.C. Hendriks, A.-J. van der Veen, N.M. de Groot, *Improved local activation time annotation of fractionated atrial electrograms for atrial mapping*, Journal of Computers in Medicine and Biology (2020).
3. **B. Abdi**, M.S. van Schie, N.M. de Groot, R.C. Hendriks, *Analyzing the Effect of Electrode Size on Electrogram and Activation Map Properties*, Journal of Computers in Medicine and Biology (2021)

### CONFERENCES

1. **B. Abdi**, R.C. Hendriks, A.-J. van der Veen, N.M. de Groot, *Ventricular Activity Signal Removal in Atrial Electrograms of Atrial Fibrillation*, BIOSIGNALS 12th International Conference on Bio-inspired Systems and Signal Processing (2019).
2. **B. Abdi**, A.-J. van der Veen, N.M. de Groot, R.C. Hendriks, *Local Activation Time Estimation in Fractionated Electrograms of Cardiac Mappings*, IEEE Engineering in Medicine and Biology Society (EMBC) (2019).
3. **B. Abdi**, R.C. Hendriks, A.-J. van der Veen, N.M. de Groot, *Local activation time annotation in atrial electrogram arrays using deconvolution*, Computing in Cardiology (CinC) (2019).
4. **B. Kolling**, B. Abdi, N.M.S. de Groot, R.C. Hendriks, *Local Activation Time Estimation in Atrial Electrograms Using Cross-Correlation over Higher-Order Neighbors*, European Signal Processing Conference (EUSIPCO) (2020).

**SYMPOSIA**

1. **B. Abdi**, A.-J. van der Veen, N.M. de Groot, R.C. Hendriks, 32. *Estimating Tissue Conductivity from Atrial Electrograms*, WIC/IEEE SP Symposium on Information Theory and Signal Processing in the Benelux (2018).
2. **B. Abdi**, A.-J. van der Veen, N.M. de Groot, R.C. Hendriks, 10. *Estimating Source-to-Electrode Transfer Functions in Atrial Electrograms*, WIC/IEEE SP Symposium on Information Theory and Signal Processing in the Benelux (2019).



# 2

## BACKGROUND AND FUNDAMENTALS

### 2.1. THE HEART AND ITS PHYSIOLOGY

#### 2.1.1. THE HEART

The heart pumps blood containing oxygen and nutrients throughout the body. It is a muscular organ located between the lungs behind and slightly to the left of the breastbone. The heart consists of four chambers, two upper chambers, the atria, and two lower chambers, the ventricles shown in Fig. 2.1 (a). With these four chambers, the heart pumps blood via a system of blood vessels, called the circulatory system, in successive cardiac cycles. The right and left chambers of the heart are separated. The right chambers pump the oxygen-poor blood to the lungs and the left chambers pump the oxygen-rich blood to the body. Each cardiac cycle starts with the atria (upper chambers) and the ventricles (lower chambers) being in a relaxed state. In this state the atria get refilled with blood. This is followed by a contraction in the atrial muscles that ejects the blood into the ventricles. Ventricular contraction occurs with a short delay afterwards and pumps the blood through the body. This cycle lasts on average 0.8 seconds in a human heart [4].

#### 2.1.2. CARDIAC CONDUCTION SYSTEM

The cardiac cycle occurs as a result of the generation and conduction of a series of electrical impulses by the cardiac conduction system as shown in Fig. 2.1 (b). These electrical impulses are generated by a group of cells at the sinoatrial (SA) node (anatomical pacemaker) located in the wall of the right atrium. These impulses travel to the left atrium through Bachman's bundle (BB) and to the atrioventricular (AV) node via specific electrical pathways (shown by the red arrows in Fig. 2.1). The propagation of these electrical impulses causes the atrial muscles to contract. The impulses are then delayed at the AV node for about a tenth of a second. This brief delay is enough to ensure that the blood is completely ejected from the atria into the ventricles. The electrical signal then propagates through the ventricles, which causes them to contract next [19].

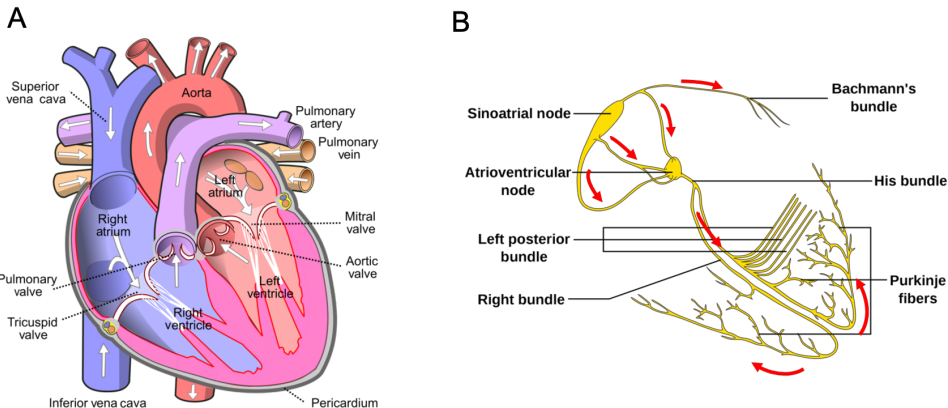


Figure 2.1: (A) The diagram of the heart as well as (B) the cardiac conduction system . The red arrows shows the direction of electrical wave propagation in normal heart (adapted from [17] and [18]).

The electrical activity in the heart arises from the pacemaker cells at the SA node that can automatically generate an action potential (AP). An AP is a sequence of changes in the cell membrane potential from its resting potential (around  $-90\text{mV}$ ). It starts with a rapid rise in the potential membrane (depolarization phase) followed by a plateau and a fall in the potential membrane (repolarization phase). The depolarization phase of the pacemaker cells initiates the AP generation in the neighboring cardiomyocytes, the cells that make up the heart muscles. This leads to the contraction of these cells as well as the initiation of the AP in their neighboring cells. This results in the propagation of the depolarization wave through the whole heart. Fig. 2.2 (a) shows different APs generated by different type of heart cells [19].

Fig. 2.2 (b) shows a zoomed version of an example atrial AP. There are two important parameters that characterize an AP and that are of higher importance in our study. These are the activation time and the refractory period. The activation time of a cell is annotated as the time when the cell's potential reaches a threshold value of  $-40\text{mV}$  in the depolarization phase of its AP. This ensures that the AP is triggered in the cell, otherwise no action potential will be fired by the cell. The refractory period is the minimum period that is required for a cardiac cell before another AP can be fired. This is around 250 ms, which is a bit shorter than the duration of an AP and helps to protect the heart from generating very rapid heart beats [19].

### 2.1.3. MEASURING THE HEART ELECTRICAL ACTIVITY

Measuring the electrical activity of the heart provides important information about the functioning of the heart. The most common way for recording this activity is by placing electrodes on a patient's body surface. The measured electrical activity of the heart over time at the electrode location, is called an electrocardiogram (ECG or EKG) which is actually the spatial average activity of all heart cells. Fig. 2.2 (a) shows an example ECG of a normal heart rhythm, also called sinus rhythm (SR). As can be seen, it consists of three different

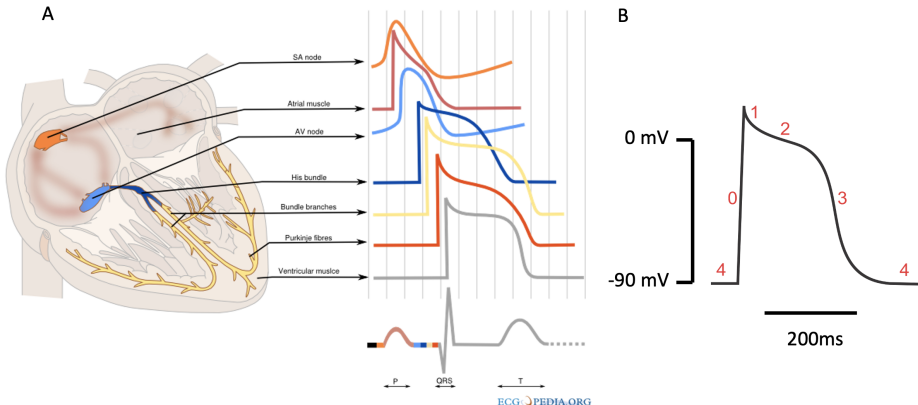


Figure 2.2: (A) Different APs generated by different cardiac cells during one complete cardiac cycle as well as the resulting ECG recorded from the body surface (adapted from [20]). (B) The zoomed version a standard atrial action potential.

waves. The P wave, which is associated with atrial depolarization, the QRS complex, which is associated with ventricular depolarization, and the T wave, which is associated with ventricular repolarization [19]. The morphology and the timing of these waves with respect to each other provides important diagnostic tools for detection and analysis of many types of cardiac disorders.

More detailed information about the electrical activity of the heart is obtained by placing the electrodes directly on the heart tissue instead of on the body surface. This can be done during open chest or open heart surgeries, or by using a catheter inside the heart. The measured signals are called atrial or ventricular electrograms (EGMs) [21]. The signals that are recorded from the outer layer of the heart surface are called epicardial EGMs, while the signals that are recorded from the inner layer of the heart surface are called endocardial EGMs. Compared to body surface measurements, electrograms provide more local and higher spatial resolution recordings of the depolarization wave propagation through the heart tissue and are less affected by different structures that surround the heart. Fig. 2.3 (a) shows an example of a normal unipolar EGM, which records the difference between the electrical activity at one electrode and a reference electrode. As can be seen, it is composed of a positive spike followed by a sharp negative deflection. As the depolarization wave moves towards the electrode, it measures the positive potentials, when the depolarization wave is exactly under the electrode it measure a zero potential. This coincides with the activation time of the cells that are under the electrode and is annotated as the local activation time (LAT) of the electrogram. As the wave moves away from the electrode, it measures a negative potential [21].

Another type of electrogram recording, used more often in practice, is the bipolar electrogram. Bipolar electrograms are computed by subtracting two closely spaced unipolar electrograms. Fig. 2.3 (b) shows an example of a normal unipolar and a bipolar electrogram. Due to the subtraction (which acts as high-pass spatial filtering), bipolar EGMs are

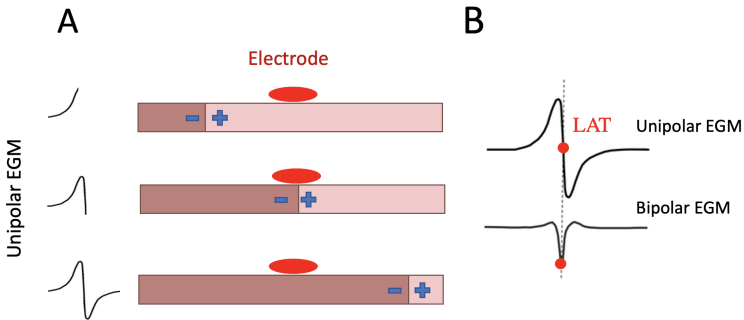


Figure 2.3: (A) generation of a normal unipolar EGMs. (B) An example of simultaneously recorded unipolar and bipolar EGM.

less affected by artifacts and nonlocal activities and provide a sharper representation (higher frequency information) of the depolarization wave propagation. This makes them more favorable in practice. However, these recordings suffer from serious drawbacks including sensitivity to propagation direction and speed, inter-electrode distances, and potential strength distribution. This is because of the loss of information as a result of the subtraction.

In this study, we are focusing on developing a simplified model for an array of electrograms and will use the model in more advanced signal processing algorithms (than only the subtraction in the bipolar case) to extract useful information from the array of electrograms. Therefore, we will only use unipolar electrograms without the subtraction performed on them.

## 2.2. ATRIAL FIBRILLATION

### 2.2.1. WHAT IS ATRIAL FIBRILLATION?

The electrical abnormalities that may be present in the heart activity are called arrhythmia. Some arrhythmias are not directly life threatening, but can cause many different problems to the patient. Among these is atrial fibrillation (AF), which is caused by chaotic and irregular depolarization of the atrial tissue. This could lead to irregular and rapid beats in the ventricles too. The cause of these chaotic and irregular depolarization waves is not yet well-known. However, AF is one of the most common age-related cardiac arrhythmia. In Europe, 1–3% of the population (more specifically the elderly) suffers from AF [2]. Patients may initially experience spontaneous short episodes of AF that come and go, which is not dangerous by itself. However, in some cases the episodes get longer, happen more often and may become continuous over time. Accordingly, AF is classified in four categories: paroxysmal, persistent, long-standing persistent, and permanent AF. The progression of AF can lead to blood clots, stroke, heart failure and other heart-related complications and requires treatment [3].

Although the main cause of AF is not known, it is more common among elderly and people with some pre-existing conditions that cause abnormalities or damage to the heart

structure. Common conditions are high blood pressure, a previous heart attack, abnormal heart valves, and congenital heart diseases. However, sometimes none of the conditions that can be related to AF are observed in a patient, a condition called lone atrial fibrillation [22].

An ECG test is the most common diagnostic tool to confirm whether a patient suffers from AF. An example of an ECG during SR and AF is shown in Fig. 2.4. As can be seen, AF can be characterized by irregular heart beats as indicated from irregular intervals between successive QRS complexes and the absence of P waves that happens due to unsynchronized atrial electrical activities [15].



Figure 2.4: recorded ECG during atrial fibrillation (top) and sinus rhythm (bottom). The purple arrow indicates a P wave, which is lost in atrial fibrillation [23].

### 2.2.2. PATHOPHYSIOLOGICAL MECHANISMS UNDERLYING AF

Many studies have been performed to explain the initiation and maintenance of AF in atrial tissue. Despite the various mechanisms introduced in the literature by different studies, there is still an ongoing debate on a precise and consistent mechanism. Most common pathological mechanisms that can explain the initiation and maintenance of AF to some extent are: ectopic foci, reentry, rotor, breakthroughs, and multiple wavelets [6].

Some studies have shown that AF initiation and sustenance can be correlated to spontaneously firing pulmonary vein (PV) and non-PV foci that interfere with sinus activity (Fig. 2.5(a)) [6, 9]. Reentry happens due to a circuit within the myocardium, where the activation wave propagates in a circular path and fails to die out. This can for example happen around a scar in the tissue. Rotors, on the other hand, are regions of functional reentry, which drive AF [9]. Since rotors are not related to anatomical structures, they can move through the tissue (Fig. 2.5(b)). Endo-epicardial breakthroughs that happen due to asynchronous wave propagation in endocardial and epicardial surface can also lead to atrial fibrillation (Fig. 2.5(c)) [8]. Another mechanism that mainly contributes to maintenance of AF is the multiple wavelet mechanism. As the propagating wave moves through the tissue, it may break into multiple wavelets when going through an anatomical barrier like a vein or a scarred tissue. The resulting wavelets may spread out in different directions and with different velocities and may also break into other wavelets. This can result in the chaotic and irregular wave propagation observed during AF (Fig. 2.5(d)) [7].

Note that the previously mentioned mechanisms are not always contradictory to each

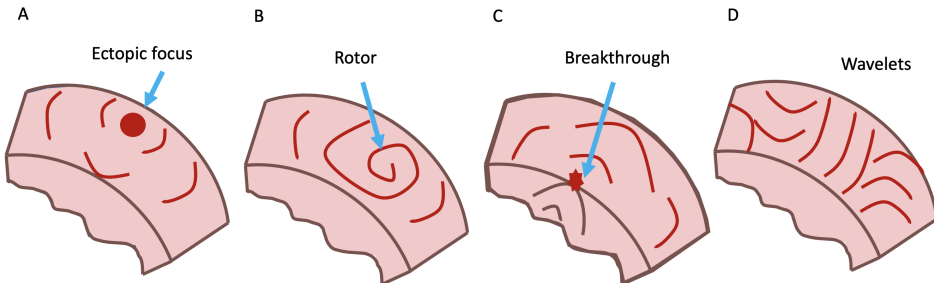


Figure 2.5: Different AF mechanisms.

other but can be complementary on providing a comprehensive description of the overall mechanism underlying AF. Moreover, differences in measurement methods and equipment, and the analysis performed on the data can result in different interpretation of the same process. For example, a breakthrough can be mistaken as a reentry due to lack of measurements from underlying tissue. Regardless of the mechanism underlying AF, studies have shown that its development and progression is, to a large extent, rooted in impaired electrical conduction and structural damage of atrial tissue, known as electropathology. Therefore, localizing and quantifying the degree of electropathology in the atrial tissue can help to provide a better understanding of atrial fibrillation.

### 2.2.3. AF TREATMENT: ABLATION

The earlier AF is diagnosed, the higher the chance of a successful treatment will be. These treatments can be categorized in three groups: (i) medication to prevent blood clots or to restore normal heart rate and rhythm, (ii) non-surgical procedures including electrical cardioversion, radiofrequency catheter ablation, (iii) surgical procedures including pacemakers and the open-heart maze procedure.

Ablation therapy is a minimally invasive treatment for atrial fibrillation and is performed using catheters that are guided through the blood vessels into the heart. The catheter can also be used for recording endocardial electrograms that will be used for localization of areas in the tissue that may be initiating AF or may be creating irregular electrical pathways. Next, the catheter is used to scar or destroy these areas and to disrupt AF. If the therapy is successful, a normal heart rhythm will be restored. However, in some cases AF may return.

There are four common types of catheter ablation including: (i) pulmonary veins isolation ablation, which scars the tissue where the pulmonary veins are connected to isolate AF triggers [24]. This type of ablation is also performed together with other types of ablations. (ii) atrioventricular (AV) node ablation, that prevents the irregular atrial signals to propagate to the ventricles [25]; (iii) linear atrial ablation, ablation that creates long lines of scarred tissue in the atria [26], and (iv) electrogram guided ablation, where the vulnerable tissue that is mostly correlated with complex fractionated electrograms or low voltage areas are first identified using the recorded electrograms and then ablated [27].

Despite the progress in developing ablation therapies, the overall success rate is yet lim-

ited. This is mainly due to the lack of understanding about the mechanisms initiating and maintaining AF as discussed in Section 2.2.2. This also holds for other types of AF treatment. Therefore, to improve the success rate of AF treatment procedures, a comprehensive understanding of the mechanisms underlying AF is necessary.

## 2.3. ATRIAL MAPPING AND ELECTROGRAM RECORDING

Although ECG recordings are non-invasive, they provide rather limited information on what is actually going on in the atria. The large distance to the heart results in a spatially smoothed signal. On the other hand, recording the electrical activity of the atria using closely spaced electrodes directly positioned on the atria, known as atrial mapping, can help to improve our understanding of atrial fibrillation [5]. This provides a spatio-temporal recording of the wavefront propagation in the tissue, which can potentially be used for the localization of patient specific substrates that initiate or perpetuate AF. They can also help to localize and quantify the degree of electropathology and to stage AF in patients.

During the mapping procedure used in this study, epicardial electrograms were recorded using a 192-unipolar flexible electrode array ( $8 \times 24$ ) with 2 mm inter-electrode distance and 0.45 mm electrode diameter. The electrogram array and some sample electrogram recordings are shown in Fig. 2.6 A. The electrode array is sequentially positioned on 9 locations using the anatomical borders, visually by the surgeon (shown in Fig. 2.6 B), to cover the whole right and left atria including Bachman's bundle (shown in Fig. 2.6 C).

The array records 5 seconds of sinus rhythm (SR) signals and 10 seconds of induced atrial fibrillation. AF is induced by fixed rate pacing at the right atrial free wall, which starts at a rate of 200 beats per minute (bpm). If an AF induction attempt is not successful after three burst attempts, the rate is increased by 50 bpm, up to maximal 400 bpm until AF occurs. The acquired signals are amplified, filtered (bandwidth 0.5 to 400 Hz), sampled (1 kHz), analogue to digital converted (16 bits) and recorded on a hard disk.

## 2.4. EGM PRE-PROCESSING AND ANALYSIS

### 2.4.1. EGM PREPROCESSING

As mentioned in Section 2.3, our electrograms are band-pass filtered (bandwidth 0.5 to 400 Hz) and notch filtered at 50 Hz (to cancel out power-line interference) by the recording device. However, we still need to perform noise and artifact removal before performing any analysis on the data. Three important preprocessing steps for atrial electrograms include: (i) high-pass filtering for baseline wander removing, (ii) low-pass filtering for removing high frequency noise, and (iii) removing strong far-field ventricular artifacts.

Baseline wander is a low frequency noise mostly caused by patient's movement and respiration. On the other hand, high frequency noise mostly includes additive white Gaussian noise. To remove these noises we perform low-pass and high-pass filtering of EGMs using a wavelet decomposition. Each electrogram is first decomposed using order N=10 (length of  $2N=20$ ) Daubechies wavelet at level 9. For high-pass filtering the approximation coefficients at level 9 having the frequency range of 0 to  $500/512=0.98$  Hz are removed from the signal. Next, a standard wavelet shrinkage denoising method is used for low-pass filtering [28]. Fig. 2.7 shows an example of two EGMs, one recorded during SR and one recorded during AF, before and after high-pass and low-pass filtering. Note that throughout

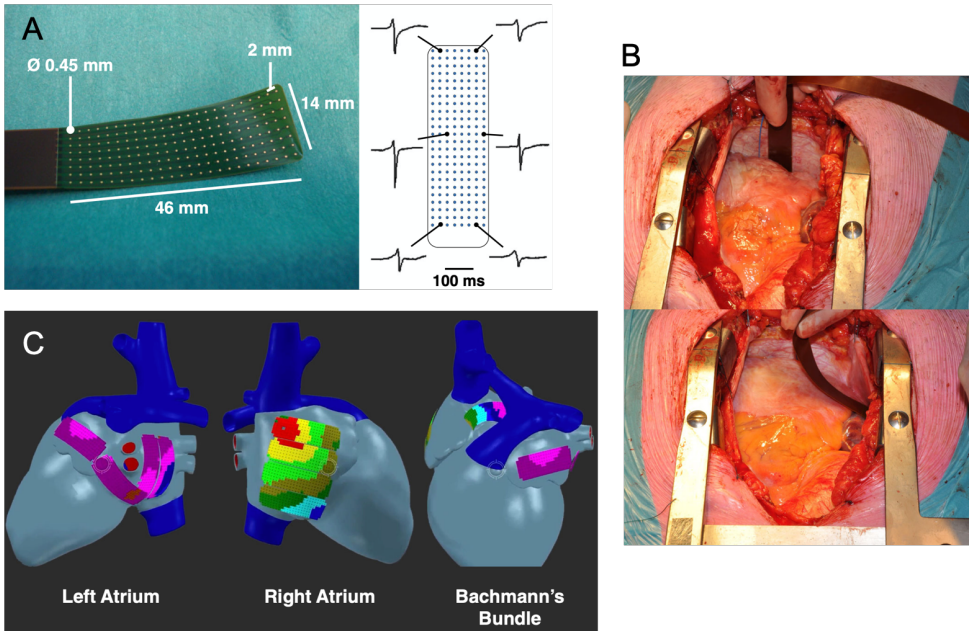


Figure 2.6: Electrode array and some sample electrogram recordings (A), The positioning of the electrogram on atria during open chest surgeries by the surgeon (B), and the 9 successive locations where the electrode array is positioned (C) [5].

this study, we visually selected clean electrograms and avoided noisy recordings. Therefore this simple filtering approach will suffice for our application and we did not focus on extensive filtering approaches.

Electrograms also suffer from a strong artifact caused by far-field ventricular activities (VAs) as a result of ventricular depolarization. Although during SR, atrial activity (AA) and VA are separated in time due to the brief delay at the AV node, they might overlap during AF. As an example, Fig. 2.7 shows the onset and offset of VAs denoted by red vertical lines. When overlapping with AAs, these strong VAs distort the morphology of the pure AAs, complicate their further analysis, and affect their final interpretation. Therefore, a step required before any further processing of the recorded electrograms is to estimate the pure atrial activities by removing the VAs. In this dissertation, we developed a new framework for removing VA which is based on a sparse and low rank matrix decomposition. The approach is discussed in detail in Chapter 3.

### 2.4.2. ELECTROGRAM ANALYSIS

In clinical practice, various measures are estimated from a single electrogram or an array of electrograms to characterize its properties, investigate wave propagation in the tissue, or study AF and electropathology. In this section, we introduce some of the common measures that are used in our study.

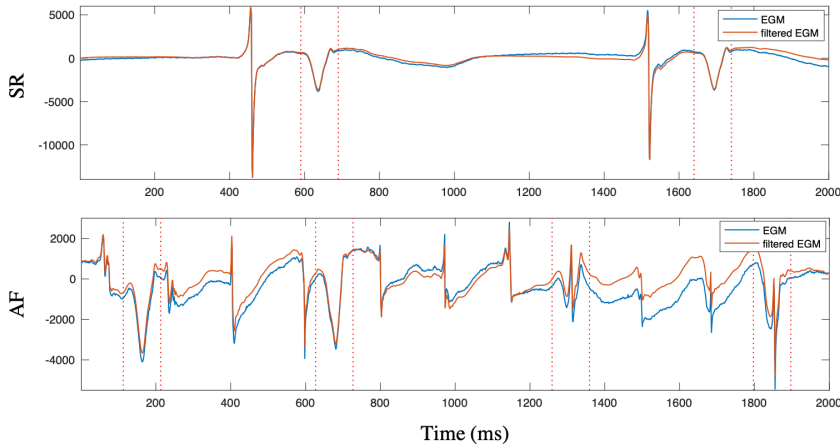


Figure 2.7: Two electrograms, recorded during SR and AF respectively, before and after high-pass and low-pass filtering. Segments containing the onset and offset of a VA are denoted by red vertical lines.

**Local Activation Time (LAT)** In a normal electrogram, the activation time of the cells that are under the electrode coincides with the point having the steepest descent in a single atrial beat [29]. Fig. 2.8 shows and example of a normal electrogram with its LAT.

**Activation map (AM)** For an array of electrograms, the activation map is an image of similar size as the array, where each pixel color corresponds to a value that equals the LAT of its corresponding electrode on the array in each atrial beat<sup>1</sup>. The LATs are color coded from red (small values) to purple (larger values) to better visualize wave propagation through the array. Fig. 2.8 shows two examples of AMs recorded during SR and AF. The black arrows show the direction of the depolarization wave propagation.

**Slow conduction zone and conduction block** If the absolute difference between the LAT of two neighboring cells is larger than a defined threshold value, the border between them will be considered as a slow conduction zone or a conduction block. The threshold values differ between studies and are mostly defined with respect to application and inter-electrode distances. Thick lines in activation maps shown in Fig. 2.8, denote the estimated conduction blocks.

**Deflections and fractionation** Deflections are the steep descents in an electrogram that have an average negative slope smaller than a defined threshold value. A normal electrogram has one main deflection. However, due to inhomogeneous activations, remote activations, and/or artifacts, electrograms may have multiple deflections [31] (shown in Fig. 2.9). Such an electrogram is called a fractionated electrogram. Fig. 2.10 shows an example of a

<sup>1</sup>By atrial beat we mean a time window in which all the cells, in the recording area, get activated once. The time window is selected such that all the cells are at their resting potentials in the beginning, get activated once and go back again to their resting potential at the end.

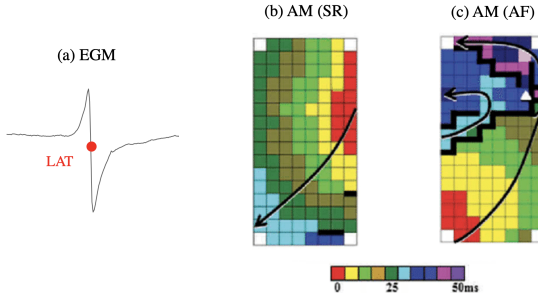


Figure 2.8: a normal electrogram with its local activation time (a). Activation maps recorded during SR and AF, (a) and (b) respectively. The black arrows show the direction of depolarization waves and thick lines in the AMs show the conduction blocks [30].

fractionated electrogram and some of its parameters. Fractionated electrograms are of high importance in studying AF because their pathological causes can help to study the initiation and maintenance of AF. Fractionated electrograms are also observed in normal hearts and during SR, however their occurrence and complexity increase during AF.

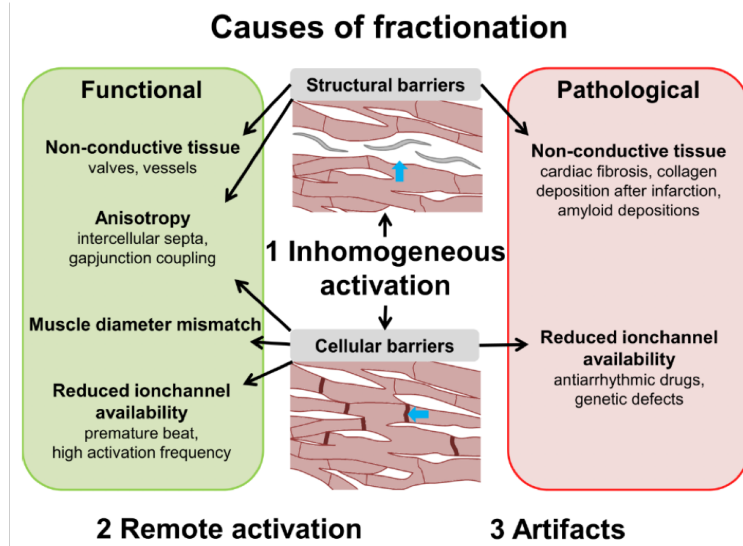
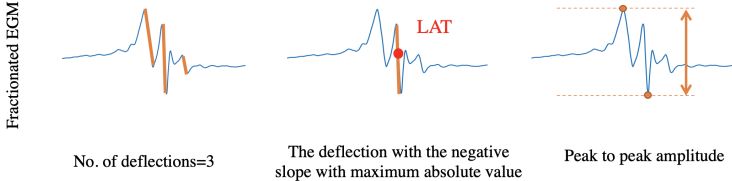


Figure 2.9: Causes of fractionation [31].

**Low voltage electrograms** If the peak-to-peak amplitude of an electrogram (shown in Fig. 2.10) is smaller than a defined threshold value, the electrogram is considered as a low voltage electrogram and the recording site is indicated as a low voltage area in the tissue. Low voltage electrograms do not show a distinct steep deflection and are mostly associated



2

Figure 2.10: An example of a fractionated electrogram and its different measures.

with complex fractionated (atrial) electrograms (CFAE) with no distinct resting zero potential in between atrial beats [32]. Fig. 2.11 (B) shows an example of low voltage fractionated electrogram together with a normal electrogram for comparison. These locations are also of high importance in studying electropathology and atrial fibrillation, and also as targets for EGM guided ablation therapies as locations that help to maintain AF (see ).

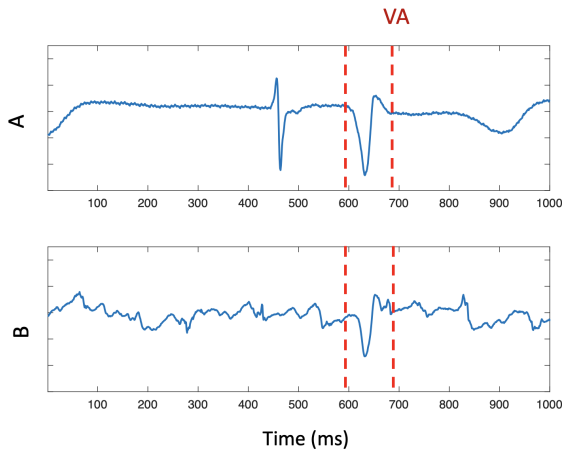


Figure 2.11: (A) An example of a normal electrogram, (B) An example of low voltage fractionated electrogram. The red vertical dashed lines show the start and end of ventricular activity.

## 2.5. AP AND EGM MODELS

### 2.5.1. ACTION POTENTIAL MODEL

To understand what is actually being measured by an electrogram, we first need to introduce the electrophysiological model of the action potential. The cell membrane, separating intracellular and extracellular spaces, can be modelled as a capacitor connected in parallel to variable resistances and voltage sources which represent the ionic channels and driving forces [33]. Fig. 2.12 shows the simplified equivalent electrical circuit of the cell model, where  $V(t)$  is the transmembrane potential at time instant  $t$ ,  $C \approx 1 \mu\text{F cm}^{-2}$  is the total membrane capacitance,  $I_{st}$  is the external stimulus current, and  $I_{ion}$  is the total ionic current. The

total ionic current includes all ionic and pump currents through the membrane and is calculated based on the Courtemanche model in [33]. The capacitive current through the cell membrane, which is equal to  $C\partial V/\partial t$ , is given by

$$2 \quad C \frac{\partial V(t)}{\partial t} = I_{st}(t) - I_{ion}(t, V). \quad (2.1)$$

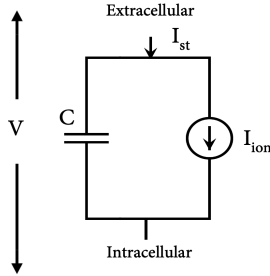


Figure 2.12: Equivalent electrical circuit of the action potential model.

### 2.5.2. ACTION POTENTIAL PROPAGATION MODEL

To develop the action potential model in Eq. (2.1) to include the flow of current and action potential in the atrial tissue, we use the generalized cable theory or the mono-domain approach [13]. In this approach the tissue is discretized on a two (or three) dimensional grid and the electrical propagation (from cell-to-cell) is governed by a reaction-diffusion equation. Let  $V(\mathbf{x}, t)$  be the transmembrane potential of the cell at location  $\mathbf{x}$  and time instant  $t$ , then the capacitive current through the cell membrane is given by the reaction-diffusion equation which models the membrane current as a function of three currents,

$$C \frac{\partial V(\mathbf{x}, t)}{\partial t} = I_{tm}(\mathbf{x}, t) + I_{st}(\mathbf{x}, t) - I_{ion}(\mathbf{x}, t, V), \quad (2.2)$$

where  $I_{tm}(\mathbf{x}, t)$  is the cell transmembrane current per unit area that accounts for the spatial evolution (diffusion) of the transmembrane potential. It is given by

$$I_{tm}(\mathbf{x}, t) = S_v^{-1} \nabla \cdot (\Sigma(\mathbf{x}) \nabla V(\mathbf{x}, t)), \quad (2.3)$$

where  $S_v = 0.24 \mu\text{m}^{-1}$  is the cellular surface to volume ratio,  $\nabla$  is the gradient operator, and  $\nabla \cdot$  is the divergence operator.  $\Sigma(\mathbf{x}) = [\sigma_{xx}, \sigma_{xy}; \sigma_{yx}, \sigma_{yy}]$  is a location-dependent conductivity tensor containing the tissue's electrical conductivity at location  $\mathbf{x}$ , in different directions (see Section 4.2.3 for more details). Eq. (2.2) can be discretized and solved with no flux boundary conditions (sealed ends by setting  $\partial V/\partial x = 0$  at boundaries), using various approaches including a finite difference method (FDM) for regular rectangular meshes, or using a finite element method (FEM) or finite volume method (FVM) for irregular triangular meshes and curved surfaces.

### 2.5.3. ELECTROGRAM MODEL

An electrogram is a record of changes in the electrical potential of the (many) cells in the neighborhood of an electrode that is positioned on the heart surface, denoted by  $\Phi(\mathbf{y}, t)$ , where  $\mathbf{y}$  is the location vector of the electrode. The electrogram can be modeled using a current source approximation for a large volume conductor [13], i.e.,

$$\Phi(\mathbf{y}, t) = \frac{1}{4\pi\sigma_e} \int_{A_0} \frac{I_{tm}(\mathbf{x}, t)}{\|\mathbf{y} - \mathbf{x}\|} dA(\mathbf{x}), \quad (2.4)$$

where the modeled cells are located within the area  $A_0$ ,  $\sigma_e$  is the constant extra-cellular conductivity, and  $I_{tm}(\mathbf{x}, t)$  is the trans-membrane current per unit area as defined in Eq. (2.3).

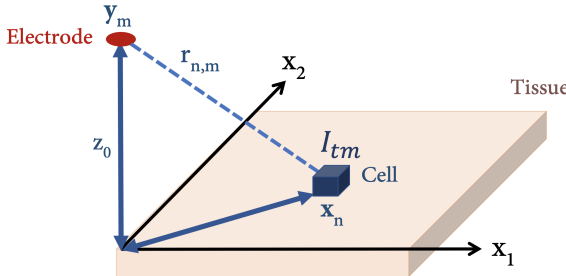


Figure 2.13: The space-discretized representation of the 2D modelled tissue and the electrode.

To model the measurement process, we develop a space-discretized representation of Eq. (2.4) for an electrode array. Consider an array of  $M$  electrodes, and let  $\mathbf{y}_m$  be the location of an electrode with index  $m \in \{1, 2, \dots, M\}$ . Also let  $\mathbf{x}_n$  denote a  $\Delta l$ -by- $\Delta l$  discretization of  $\mathbf{x}$  with  $a = (\Delta l)^2$  the area of each element of the grid and  $n$  the index of an element (modeled cell) in the grid. This is shown in Fig. 2.13 for a modeled cell at  $\mathbf{x}_n$  and an electrode at distance  $r_{m,n}$  from the cell. The space-discretized representation of Eq. (2.4) on a two-dimensional (2D) gridded tissue is

$$\Phi_m(t) = \frac{1}{4\pi\sigma_e} \sum_{n=1}^N \frac{I_{tm}(\mathbf{x}_n, t)}{r_{m,n}} a \quad (2.5)$$

where  $\Phi_m(t) \equiv \Phi(\mathbf{y}_m, t)$ . In Eq. (2.5),  $r_{m,n}$  denotes the distance between the electrode with index  $m$  and the cell with index  $n \in \{1, 2, \dots, N\}$  where  $N = r_c \times c_c$  is the total number of modeled cells or the elements of the grid with  $r_c$  rows and  $c_c$  columns. We will assume that the electrodes are also located on a 2D grid parallel to the tissue surface at a height that equals  $z_0$ . If we neglect for simplicity the electrode diameter,<sup>2</sup> we can write

$$r_{m,n} = \sqrt{\|\mathbf{y}_m - \mathbf{x}_n\|^2 + z_0^2} \quad (2.6)$$

and we define  $\mathbf{r}_m = [1/r_{m,1}, 1/r_{m,2}, \dots, 1/r_{m,N}]^T$  to contain the inverse of the distances of all cells to electrode  $m$ .

<sup>2</sup>Later in Section 6.2.2 we consider the effect of the electrode diameter. However, since in most of our simulations a relatively large spatial step size  $\Delta l$  is considered, the electrode diameter which is smaller than  $\Delta l$  can be ignored.

A space-discretized representation of all cellular transmembrane currents in Eq. (2.3) is then given by

$$\begin{aligned} I_{\text{tm}}(\mathbf{x}_n, t) &= S_v^{-1} \nabla \cdot \boldsymbol{\Sigma}_n \nabla V_n(t) \\ &= S_v^{-1} \left( \frac{\partial}{\partial x} \left( \sigma_{xx,n} \frac{\partial V_n}{\partial x} \right) + \frac{\partial}{\partial x} \left( \sigma_{xy,n} \frac{\partial V_n}{\partial y} \right) \right. \\ &\quad \left. + \frac{\partial}{\partial y} \left( \sigma_{yx,n} \frac{\partial V_n}{\partial x} \right) + \frac{\partial}{\partial y} \left( \sigma_{yy,n} \frac{\partial V_n}{\partial y} \right) \right) \end{aligned} \quad (2.7)$$

where  $\boldsymbol{\Sigma}_n \equiv \boldsymbol{\Sigma}(\mathbf{x}_n)$  and  $V(\mathbf{x}_n, t) \equiv V_n(t)$ .

#### 2.5.4. SIMULATED TISSUE AND ACTIVATION MAPS

The models introduced in Eqs. (2.2) and (2.7) can be used in a forward approach to simulate electrical wave propagation in 2D tissues. First the 2D tissue and its conductivity map  $\boldsymbol{\Sigma}_n$  should be defined. An example conductivity map is shown in Fig. 2.14 where the inhomogeneity in the tissue is introduced by random lines of blocks (having zero conductivity), denoted by dark blue lines. The red circles show the location of electrode array on the tissue. Eq. (2.2) is then used to estimate AP wave propagation in the tissue. Note that the tissue is stimulated with a stimulation current injected to the cell at the left bottom of the tissue for 1 ms. The total ionic current is also calculated based on the detailed Courtemanche model in [33]. The resulting activation map is also shown in the figure. Finally, Eqs. (2.5) and (2.7) are used to compute the electrograms. As can be seen, due to the inhomogeneity in the tissue, the resulting electrograms are fractionated. More details on the simulated tissue parameters and employed inhomogeneity patterns can be found in Chapters 4 to 6.

One important observation in simulated fractionated electrograms is that the steepest descent, that is commonly annotated as the LAT, can provide an inaccurate LAT estimate. This happens due to the strong inhomogeneous activations in neighbouring cells that can still be recorded by the electrode. These strong activities can over-impose the main small, but local deflections. Therefore, more sophisticated algorithms are needed for a better estimation of LATs. This will be discussed in detail in Chapter 5.

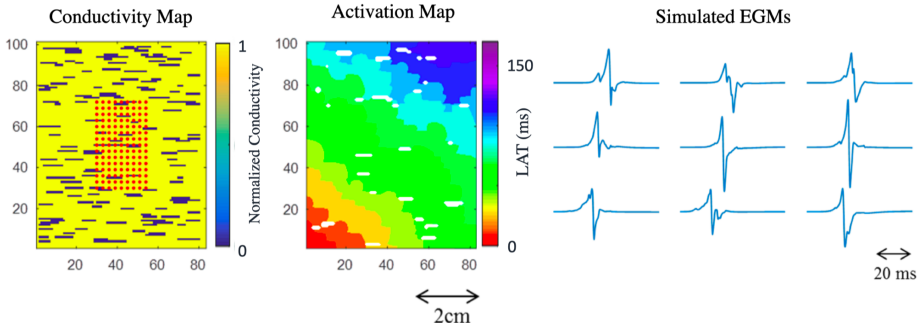


Figure 2.14: Conductivity map of a 2D model tissue (only showing  $\sigma_{xx}$ , with  $\sigma_{xx} = \sigma_{yy}$  and  $\sigma_{xy} = \sigma_{yx} = 0$ ) and its simulated activation map and some representative simulated electrograms. The red circles on the conductivity map show the electrode array location.

### 2.5.5. DEVELOPING A SIMPLIFIED ELECTROGRAM MODEL

As can be seen, the models governing electrophysiological wave propagation in the tissue, i.e., Eq. (2.2) and Eq. (2.7) are too complicated to be used in inverse problems that aim to estimate AF relevant tissue parameter. Therefore, to perform well-known signal processing approaches on these models, the first step is to simplify the models and present them in a compact matrix model based on the parameters of interest. To do so, we exploit the observation that, once activated, all cells produce almost the same stereotype AP, denoted by  $V_0(t)$  [34, 35]. As a result, the depolarization wavefront can be modelled as a series of delayed Dirac delta functions temporally convolved with the stereotype  $V_0(t)$ . The delay equals the activation time  $\tau_n$  of the cell with index  $n$  that fires an AP. To simplify the model further, we can rewrite the summation in Eq. (2.5) as a 2D spatial convolution, assuming that the electrode height  $z_0$  is constant in the recording area. This concept is demonstrated in Fig. 2.15. Since the stereotype  $V_0(t)$  and the electrode transfer function are known, the electrograms can be modelled based on two parameters, the cell activation time  $\tau_n$  and the cell conductivity in its main direction  $\sigma_n$ . More detail on the derivation of these simplified models is presented in Chapters 4 and 5.

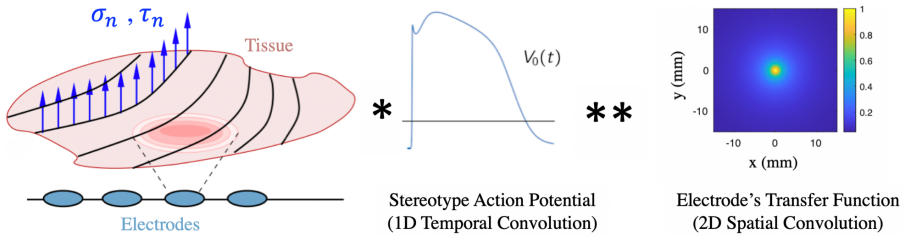


Figure 2.15: The concept of developing a simplified electrogram model. Note that for simplicity the effect of gradient and divergence operators on  $V_0(t)$  has been ignored in the picture.



# 3

## VENTRICULAR ACTIVITY REMOVAL

Diagnosis and treatment of atrial fibrillation can benefit from various signal processing approaches employed on atrial electrograms. However, the performance and interpretation of these approaches get highly degraded by far-field ventricular activities (VAs) that distort the morphology of the pure atrial activities (AAs). In this chapter, we aim to remove VAs from the recorded unipolar electrogram while preserving the AA components. To do so, we have developed a framework which first removes the VA-containing segments and interpolates the remaining samples. This will also partly remove the atrial components that overlap with VA signals, e.g., during atrial fibrillation. To reconstruct the AA components, we estimate them from the removed VA-containing segments based on a low-rank and sparse matrix decomposition and add them back to the electrograms. The presented framework is of rather low complexity, preserves AA components, and requires only a single channel EGM recording. Instrumental comparison to template matching and subtraction and independent component analysis shows that the proposed approach leads to smoother results with better similarity to the true atrial signal.

### 3.1. INTRODUCTION

Atrial fibrillation (AF) is one of the most common age related cardiac arrhythmia whose persistence and progression is rooted in impaired electrical conduction known as electropathology. Atrial electrograms (EGMs), i.e. a record of changes in the electrical potential of the (many) cells in the neighborhood of an electrode that is positioned on the heart surface, play an important role in the analysis of AF and examining the level of electropathology in human tissue [5]. However, these electrograms suffer from far-field ventricular activities (VAs) caused by ventricular depolarizations. Although during sinus

---

This chapter is based on the article published as "Ventricular Activity Signal Removal in Atrial Electrograms of Atrial Fibrillation" by B. Abdi, R.C. Hendriks, A.-J. van der Veen, N.M. de Groot in the 12th International Conference on Bio-inspired Systems and Signal Processing BIOSIGNALS, pp. 179-184, 2019.

rhythm (SR), atrial activity (AA) and VA are separated in time, they might overlap during AF. These strong VAs distort the morphology of the pure AAs, complicate their further analysis and affect their final interpretations. Therefore, a required step before any further processing of the recorded electrograms is to estimate the pure atrial activities by removing the VAs.

Rieta et al. in [36] categorizes the developed algorithms for VA removal into three groups. The first group of algorithms is based on template matching and subtraction (TMS) [37]. A second group is based on adaptive filtering using a VA reference [15], which is obtained using a reference ECG lead. The third group of VA removal algorithms is based on blind source separation approaches that try to separate the components based on the assumption that VA and AA are uncorrelated, orthogonal, or statistically independent from beat to beat over time or over space in multichannel recordings. Independent component analysis (ICA) is one of the most widely used approaches from this group [38]. None of above mentioned approaches results in a pure AA estimate. A perfect performance is hampered by the fact that these signals share overlapping components in both time and frequency domain and are also partially correlated over time and space.

In this study we develop a new framework for removing VA which is based on a sparse and low rank matrix decomposition. Initially, VA-containing segments are detected, removed and replaced with subsequent spline interpolation. However, the performance of this approach is limited during AF, as VAs might overlap with the depolarization phase of AAs. In our approach, we propose to reconstruct AAs in the removed segments and add them back to the interpolated signal. Finally, using simulations, we compare the performance of the proposed algorithm with two other approaches, TMS and ICA.

The remainder of this chapter is as follows. In Section 3.2 we formulate the ventricular and atrial activity separation problem and present our proposed framework for solving the problem. In Section 3.3 we present the results and compare them with two other methods. Finally, in Section 3.4, conclusions are drawn.

## 3.2. METHOD

### 3.2.1. ELECTROGRAM MODEL

We consider a sampled unipolar atrial electrogram  $\mathbf{m} \in \mathbb{R}^{N \times 1}$  with  $N$  the number of time samples. We assume that  $\mathbf{m}$  is the summation of AAs and VAs, modeled as

$$\mathbf{m} = \mathbf{a} + \mathbf{v}, \quad (3.1)$$

where vectors  $\mathbf{a}$  and  $\mathbf{v}$  contain the AA and VA samples produced by atrial and ventricular sources respectively. From the physiological point of view, the AA is composed of two phases, the depolarization phase and the repolarization phase. The depolarization phase, is of most interest and consists of a predominantly positive spike followed by a sharp negative deflection. It mostly contains high frequency AA components and shows a sparse representation in time. The repolarization phase on the other hand, changes very smoothly in time and contains very low frequency components. These repolarization activities are often viewed as baseline wandering and may even fade out in some recordings. The first row in Fig. 3.1 shows an example electrogram including some examples of the depolarization phase (sharp deflections) followed by the repolarization phase of the AAs with some over-

lapping VAs denoted by red vertical lines. Depending on the homogeneity of the depolarization wavefront and the speed of the electrical propagation in the tissue, the morphology of these two components (AA and VA) may vary from activity to activity even during SR, and they cannot be simply considered as a shifted version of each other, especially during AF.

### 3.2.2. DATA MATRIX FORMATION

To overcome the unnecessary introduction of artifacts, we use the concept of minimal processing and process only VA-containing segments. In this study, we used a simultaneously recorded ECG as reference signal to specify the VA-containing segments in the electrogram which coincide with the QRS complexes in ECG. Since the QRS complex or the R peak is easily detectable, any simple detection algorithm could be used. A rectangular window centered at each detected R peak with a fixed width  $W$  is used to mark the onset and offset of the VA and to denote the VA-containing segments that might also contain AA during AF.

The baseline wandering of the electrogram is mainly caused by the repolarization phase of AA. To remove the VA without affecting this component, we first remove the VA-containing segments and then replace them by spline interpolation applied to the remaining data samples. This can to some extent replace the removed baseline in the VA segment and is one of the most basic and efficient approaches for VA cancellation during SR [39]. The interpolated data is denoted by  $\mathbf{m}'$  and has the same length as the recorded electrogram  $\mathbf{m}$ . During SR and in some cases during AF, the VA does not overlap with the depolarization phase of AA, and leaves this component unaffected. Removal and interpolation cancels the VAs thus sufficiently and no further processing would be necessary, cf. the input signal  $\mathbf{m}$  and interpolated signal  $\mathbf{m}'$  in the first VA-containing segment of Fig. 3.1. However, unlike during SR, it is likely that during AF the depolarization phase of the AA and the VA completely or partially overlap. In this case VA removal and interpolation also removes the overlapping depolarization phase of AA. Therefore, processing the removed component, i.e.,  $\mathbf{x} = \mathbf{m} - \mathbf{m}'$ , is required to extract the potentially removed atrial components and add them back to the interpolated data, cf. the  $\mathbf{m}$ ,  $\mathbf{m}'$  and the removed signal  $\mathbf{x}$  in the second and third VA-containing segments of Fig. 3.1.

Before employing any further processing, we construct an appropriate data matrix  $\mathbf{X}$  of size  $W \times K$ , where each column of  $\mathbf{X} = [\mathbf{x}_1^T, \mathbf{x}_2^T, \dots, \mathbf{x}_K^T]^T$  is one VA-containing segment (of length  $W$ ) of  $\mathbf{x}$  stored in the vector  $\mathbf{x}_k$ ,  $k \in 1, 2, \dots, K$ , and where  $K$  is the total number of detected segments. The data matrix  $\mathbf{X}$  is modelled as the sum of two components: (i) matrix  $\mathbf{V}$  containing the aligned ventricular activities, and (ii) matrix  $\mathbf{A}$  containing the randomly occurring atrial activities that coincide with the VA-containing segment, i.e.

$$\mathbf{X} = \mathbf{A} + \mathbf{V}. \quad (3.2)$$

### 3.2.3. VA AND AA SEPARATION

We now formulate the problem of decomposing the data matrix  $\mathbf{X}$  into its two components,  $\mathbf{V}$  and  $\mathbf{A}$ . The problem can be considered as a highly underdetermined blind source separation where the number of unknowns,  $\mathbf{A}$  and  $\mathbf{V}$ , is twice the number of given measurements,  $\mathbf{X}$ . However, prior knowledge of the two sources can be employed to derive useful approximate solutions: (i) The aligned VAs in  $\mathbf{V}$ , from beat-to-beat, have an almost similar morphology

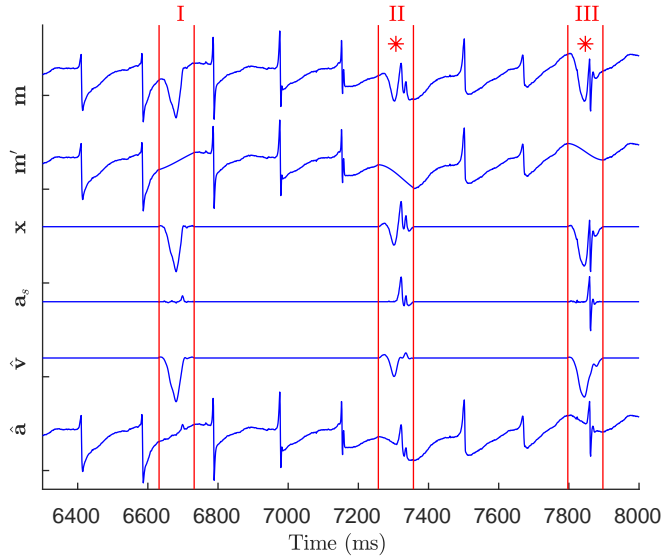


Figure 3.1: The input electrogram  $\mathbf{m}$  and output signals at each stage of the algorithm with  $\hat{\mathbf{v}}$  and  $\hat{\mathbf{a}}$  as the final extracted VA and AA output. The onset and offset of VA-containing segments are denoted by red vertical lines. The segments where AA and VA overlap are also denoted by \*.

which indicates that  $\mathbf{V}$  is a low-rank matrix, while the occurrence of AA and its morphology in these segments is random indicating that  $\mathbf{A}$  is not a low-rank matrix. (ii) When presented in frequency domain, the VAs are much sparser (have narrower bandwidth than AAs). As an example, Fig. 3.2 shows two segments of a clinically recorded EGM containing AA and VA, as well as their amplitude spectrum. Note that the segments are not overlapping in time as the EGM is recorded during SR. (iii) AAs are sharper and more spiky in time domain compared to VAs, matrix  $\mathbf{A}$  can therefore be constrained to be sparse. Exploiting these three properties, we formulate the separation problem as

$$\min_{\{\mathbf{A}, \mathbf{V}\}} \text{rank}(\mathbf{V}) + \beta \|\boldsymbol{\Psi}^T \mathbf{V}\|_1 + \alpha \|\mathbf{A}\|_1 \quad \text{s.t.} \quad \mathbf{X} = \mathbf{A} + \mathbf{V}, \quad (3.3)$$

where  $\text{rank}(\cdot)$  is the rank operator,  $\|\mathbf{A}\|_1 = \sum_{ij} |A_{ij}|$  is the  $l_1$ -norm of  $\mathbf{A}$ ,  $\boldsymbol{\Psi}^T$  performs a two-dimensional discrete cosine transform (DCT) [40], and  $\alpha$  and  $\beta$  are penalization parameters.

Since the rank function is non-differentiable and non-convex, it is in most studies approximated with the nuclear norm,  $\|\mathbf{V}\|_* = \sum_{i=1}^K \sigma_i(\mathbf{V})$ , that is the summation of all sorted (from largest to smallest) singular values  $\sigma_i$  of matrix  $\mathbf{V}$ . However, minimizing the truncated nuclear norm (TNN)  $\|\mathbf{V}\|_r = \sum_{k=r+1}^K \sigma_i(\mathbf{V})$ , that is the summation of the  $K-r$  smallest singular values, performs better in minimizing the rank function than minimizing the nuclear norm [41]. The TNN, on the other hand, is non-convex and it cannot be minimized directly. To overcome this issue, the TNN can be rewritten as its convex surrogate [41]

$$\|\mathbf{V}\|_r = \sum_{i=r+1}^K \sigma_i(\mathbf{V}) = \|\mathbf{V}\|_* - \sum_{i=1}^r \sigma_i(\mathbf{V}) = \|\mathbf{V}\|_* - \max_{\mathbf{U}_r^T \mathbf{U}_r = \mathbf{I}, \mathbf{H}_r^T \mathbf{H}_r = \mathbf{I}} \text{Tr}(\mathbf{U}_r^T \mathbf{V} \mathbf{H}_r), \quad (3.4)$$

where  $\text{Tr}(\cdot)$  indicates the trace of a matrix, and  $\mathbf{U}_r$  and  $\mathbf{H}_r$  are matrices containing the first

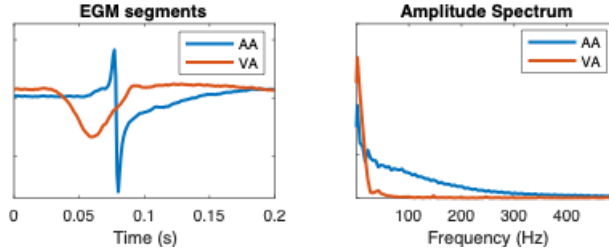


Figure 3.2: Two segments of a clinically recorded EGM containing AA and VA, as well as their amplitude spectrum. Note that the segments are not overlapping in time as the EGM is recorded during SR.

3

$r$  columns of the left and right singular vectors of  $\mathbf{V}$  respectively, where  $\mathbf{V} = \mathbf{U}\text{diag}(\boldsymbol{\sigma})\mathbf{H}^T$  is the singular value decomposition (SVD) of  $\mathbf{V}$ . Using Eq. (3.4), the new optimization problem for separation of VA and AA can be written as

$$\min_{\{\mathbf{A}, \mathbf{V}\}} \|\mathbf{V}\|_* - \max_{\mathbf{U}_r^T \mathbf{U}_r = \mathbf{I}, \mathbf{H}_r^T \mathbf{H}_r = \mathbf{I}} \text{Tr}(\mathbf{U}_r^T \mathbf{V} \mathbf{H}_r) + \beta \|\boldsymbol{\Psi}^T \mathbf{V}\|_1 + \alpha \|\mathbf{A}\|_1 \quad \text{s.t. } \mathbf{X} = \mathbf{A} + \mathbf{V}, \quad (3.5)$$

Generally, the lower  $K$  (i.e., the number of VA-containing segments in  $\mathbf{M}$ ), the less accurate the SVD will be. This might lead to AA components erroneously ending up in the low-rank matrix  $\mathbf{V}$ . Constraining  $\mathbf{V}$  to be sparse in the frequency domain using the  $l_1$  regularization on  $\boldsymbol{\Psi}^T \mathbf{V}$  overcomes that AA components, that are constrained to be sparse in time domain, end up in the  $\mathbf{V}$  matrix. Notice that we did not extensively search for efficient dictionaries for  $\boldsymbol{\Psi}$ . However, we found that the application of the DCT was computationally of rather low complexity, while leading to good performance.

A variety of numerical approaches can be used to solve the optimization problem in Eq. (3.5), among which we opt for the alternating direction method of multipliers (ADMM) [42]. This algorithm solves a convex optimization problem by breaking it into smaller pieces which are simpler to implement. Furthermore, ADMM has a fast convergence rate to a reasonable precision in practice. To solve Eq. (3.5), we follow the same approach and algorithmic steps introduced in [43]. The estimated AAs in  $\mathbf{A}$  are added back to the corresponding samples in the interpolated electrogram  $\mathbf{m}'$  using a rectangular window. This results in the final estimated atrial activity  $\hat{\mathbf{a}}$ . The ventricular activities in  $\mathbf{V}$  are also added to their corresponding samples in a zero signal of same length as  $\mathbf{m}$  using a rectangular window.

### 3.3. RESULTS

The proposed framework, from here on referred to as low-rank and sparse matrix decomposition (LRSD) method, is tested on clinically recorded epicardial unipolar electrograms. The electrograms consist of 10 s of induced AF signals recorded at similar locations on the right atrium of multiple patients, filtered (bandwidth 0.5 to 400 Hz) and sampled (1 kHz). More details on the electrode specifications can be found in [5]. To provide a clear understanding of the steps of the algorithm and enable visual inspection of the results, we initially employ it on the clinically recorded data and demonstrate the output of each step in Section 3.3.1. However, in a more detailed evaluation will be performed on synthetic data.

The results are evaluated using quantitative performance indices and will also be compared to TMS and ICA approaches.

### 3.3.1. EXPERIMENTS ON CLINICAL DATA

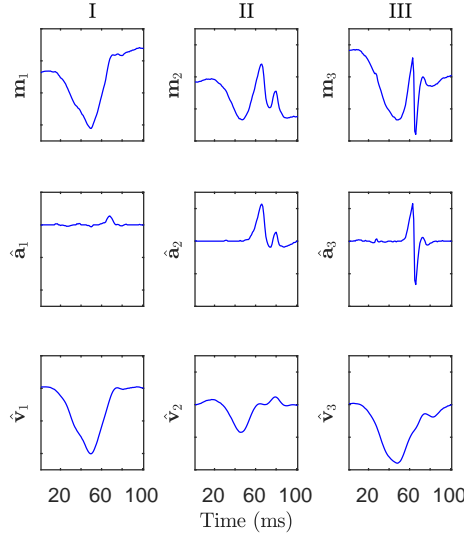
Fig. 3.1 visualizes a fragment of each stage of the proposed framework, employed on 10 s of a clinically recorded electrogram during induced AF. We normalize the electrogram first by removing the average and next by scaling the signal such that the average ventricular activity (average of all VA containing segments) has an absolute maximum amplitude of 1. This helps to make up for the variations of EGM amplitude within the patients, to some extent. The 10 seconds contain  $K = 16$  VA-containing segments, each windowed with a rectangular window with a fixed length of  $W = 100$  samples (100 ms). Since the focus of this study is on introducing the algorithm itself and not on optimal tuning of its parameters, we used values that yielded visually good source separation, that are,  $\alpha = 0.5$ ,  $\beta = 0.8$ , and  $r = 3$ .

The input signal is shown as  $\mathbf{m}$  in Fig. 3.1. The VA-containing segments are initially removed and interpolated and the result is shown as  $\mathbf{m}'$ . LRSD is employed on the data matrix  $\mathbf{X}$  containing the VA-containing segments of  $\mathbf{x} = \mathbf{m} - \mathbf{m}'$ . The separated atrial and ventricular activities resulting from the LRSD are plotted as  $\mathbf{a}_s$  and  $\hat{\mathbf{v}}$  respectively.  $\hat{\mathbf{a}} = \mathbf{a}_s + \mathbf{m}'$  demonstrates the final atrial activity estimated from the input signal  $\mathbf{m}$ . For an easier visual inspection, we show for both  $\hat{\mathbf{a}}$  and  $\mathbf{v}$  in Fig. 3.3 a zoomed version of 3 VA-containing segments from the example in Fig. 3.1.

To compare the performance of the algorithm with two other approaches we select the TMS [37] and ICA [38] approaches. TMS, similar to the LRSD, only requires one electrogram as well as the ECG signal only for detection of VA-containing segments and is computationally of low complexity. However, to separate the two sources, ICA requires the complete ECG signal. Moreover, taking care of the permutation and scaling in the result of ICA is complicated and can affect its performance. Fig. 3.4 demonstrates four clinically recorded electrograms  $\mathbf{m}$  from four different patients as well as the three estimated atrial components for each patient. As we can see, LRSD visually provides the best and smoothest output. The smoothness of the atrial component is of high importance for further processing of the data, since any added distortion might be misinterpreted as fractionated AAs.

### 3.3.2. PERFORMANCE EVALUATION

Evaluating the performance of the proposed method using quantitative performance indices, requires the pure AA and VA (ground truth), which are not available from clinically recorded data. On the other hand, due to the big range of variations in AAs and VAs morphology during AF, generating realistic synthetic data for a fair performance evaluation is difficult. To avoid these complications and test the framework on realistic data, we generated the synthesized data in two steps. First we select a sample VA-containing segment from the electrogram and we make sure it does not coincide with AA. We then extract the VA in this segment using spline interpolation and subtraction. Since VA does not overlap with AA, this provides us with well separated AA and VA components. The separated VA, referred to as pure VA, is then added to another location on the same EGM where it overlaps with pure AA and not with another VA. The pure VA is also shifted in small steps (10 ms)



3

Figure 3.3: Zoomed version of the three specified VA-containing segments in Fig. 3.1 as well as  $\hat{\mathbf{a}}$  as the final extracted atrial and ventricular activity.

to create different degrees of overlap with the AA. The same steps are also performed on the ECG signal. Finally, TMS, ICA, and LRSD are employed on the synthesized data.

To evaluate the performance of the introduced approaches in separating the AA and VA components, we use four different performance indices. The first performance index we use is the normalized cross-correlation coefficient (Pearson's correlation coefficient) between the pure AA  $\mathbf{a}$  and the extracted AA  $\hat{\mathbf{a}}$ , referred to as the similarity metric, that is

$$Si = \frac{\text{cov}(\mathbf{a}, \hat{\mathbf{a}})}{\text{std}(\mathbf{a})\text{std}(\hat{\mathbf{a}})}, \quad (3.6)$$

where  $\text{cov}(\cdot)$  is covariance and  $\text{std}(\cdot)$  is the standard deviation. The closer this variable is to 1, the more similar the signals are. The second performance index is the mean square error (MSE) between  $\mathbf{a}$  and  $\hat{\mathbf{a}}$ , denoted by  $MSE_a$ . The smaller this value is, the better the results. The third performance index is the ventricular depolarization reduction (VDR) defined as [36]

$$VDR = \left| 1 - \frac{\max(|\hat{\mathbf{v}}|)}{\max(|\mathbf{v}|)} \right| \quad (3.7)$$

where  $\max(|\mathbf{v}|)$  is the maximum amplitude of ventricular activity that coincides with the R-peak in ECG and  $\max(|\hat{\mathbf{v}}|)$  is the maximum amplitude of extracted ventricular activity. The smaller the VDR is, the better the ventricular reduction. We also introduce a new performance index that measures smoothness, abbreviated as Sm. It is calculated as the standard deviation of the first time derivative of the difference between  $\mathbf{a}$  and  $\hat{\mathbf{a}}$ , which is

$$Sm = \text{std}\left(\frac{d(\mathbf{a} - \hat{\mathbf{a}})}{dt}\right). \quad (3.8)$$

The smaller this value is, the less fractionated the results are.

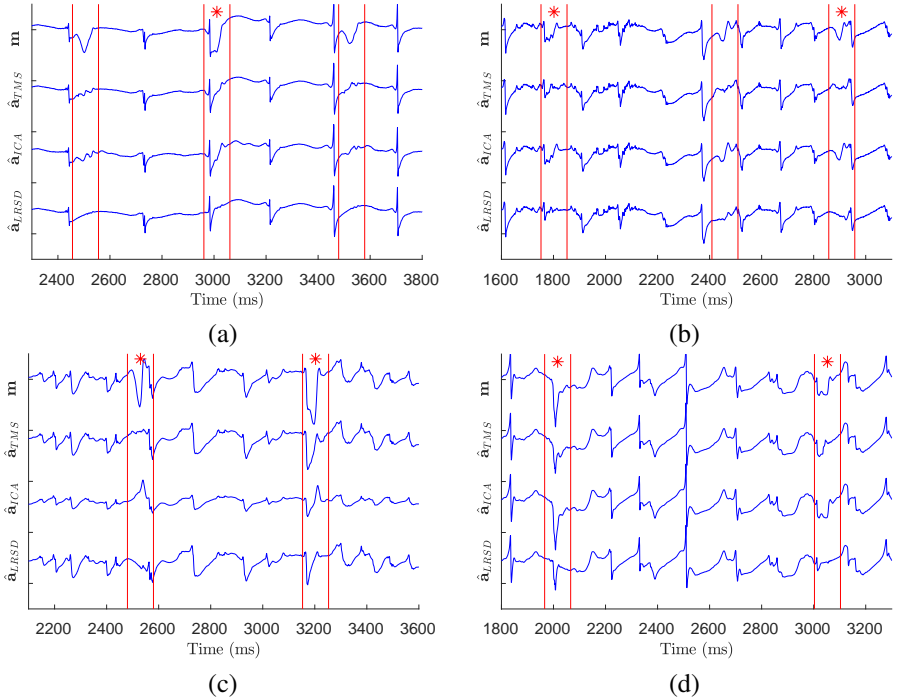


Figure 3.4: The signals shown above are respectively the clinically recorded electrogram  $\mathbf{m}$  from four different patients (a) to (d), and the separated atrial activity after employing TMS, ICA and the LRSD. The vertical lines indicate the onset and offset of VA-containing segments. Overlapping AA and VA are indicated by \*.

Table 3.1 shows the results of the instrumental measures evaluated on synthesized data of five different patients, where the VAs and AAs are separated using the three introduced approaches TMS, ICA and the LRSD. The patients are sorted based on the regularity in their VA-containing segments, where the mean square error between the average of all segments and the pure VA denoted by  $MSE_v$  is used as the indicator of the regularity. For all patients, the added pure VA overlaps with several randomly selected AAs, with different levels of overlap, except for patient 2 where we purposely chose samples with no overlap with AA. The performance of ICA in our simulations is relatively bad. This might be partly due to (i) the low quality of the ECG signal (as the second signal needed for separation of two sources using ICA, it mostly contains VAs) we had access to in this experiment and (ii) the errors in handling the permutation and scaling issues in ICA. Note that in this study, extracted VAs from ICA were automatically selected as the signal having more correlation with the initial VA containing segments.

As can be seen, the results with respect to similarity and MSE are quite comparable for all patients, however as the regularity in VA-containing segments decreases, the LRSD outperforms the other two approaches in almost all measures. Only for the first patient with very regular segments, TMS performs better than the proposed LRSD. As previously mentioned, the smoothness is of high importance since the added distortions might be misin-

Table 3.1: Summary of quantitative performance indices

	$MSE_v$		Si	$MSE_a$	VDR	Sm
P1	0.005	TMS	<b>0.96</b>	<b>0.005</b>	<b>0.19</b>	<b>0.01</b>
		ICA	0.29	0.124	0.59	0.03
		LRSD	0.75	0.031	0.26	0.02
P2	0.008	TMS	0.89	0.008	0.13	0.01
		ICA	0.80	0.058	1.53	0.02
		LRSD	<b>0.97</b>	<b>0.007</b>	<b>0.06</b>	<b>0.01</b>
P3	0.021	TMS	0.82	0.02	0.25	0.01
		ICA	0.53	2.250	2.64	0.09
		LRSD	<b>0.86</b>	<b>0.01</b>	<b>0.04</b>	<b>0.01</b>
P4	0.071	TMS	0.71	0.07	0.32	0.04
		ICA	0.36	0.958	2.64	0.09
		LRSD	<b>0.84</b>	<b>0.038</b>	<b>0.15</b>	<b>0.03</b>
P5	0.148	TMS	0.68	0.148	0.28	0.07
		ICA	0.25	2.820	2.52	0.19
		LRSD	<b>0.79</b>	<b>0.038</b>	<b>0.15</b>	<b>0.03</b>

terpreted as fractionated electrograms. However our simulations on synthesized data show that if the AA is already fractionated, the added distortions after employing TMS and ICA completely change the morphology of pure AA, while the LRSD preserves the pure AA morphology, resulting in better performances.

### 3.4. CONCLUSION

In this chapter we proposed a new framework for removal of VA from atrial electrograms, which is based on interpolation and subtraction followed by low-rank and sparse matrix decomposition. The proposed framework is of low complexity (for the 10 seconds EGM used in this study the algorithm takes around 1 second to run on a 2.9 GHz Intel i5 MacBook Pro and MATLAB R2019a.), does not require high resolution multi-channel recordings, or a calibration step for each individual patient. The approach outperforms the reference methods TMS and ICA with respect to instrumental measures. In particular in cases where the ventricular activities are less regular. It provides smooth AA estimates, which is of high importance for signal processing applications that are based on the fractionation evaluation in atrial activities.



# 4

## A COMPACT MATRIX MODEL FOR ATRIAL ELECTROGRAMS FOR TISSUE CONDUCTIVITY ESTIMATION

Finding the hidden parameters of the cardiac electrophysiological model would help to gain more insight on the mechanisms underlying atrial fibrillation, and subsequently, facilitate the diagnosis and treatment of the disease in later stages. In this chapter, we aim to estimate tissue conductivity from recorded electrograms as an indication of tissue (mal)functioning. To do so, we first develop a simple but effective forward model to replace the computationally intensive reaction-diffusion equations governing the electrical propagation in tissue. Using the simplified model, we present a compact matrix model for electrograms based on conductivity. Subsequently, we exploit the simplicity of the compact model to solve the ill-posed inverse problem of estimating tissue conductivity. The algorithm is demonstrated on simulated data as well as on clinically recorded data. The results show that the model allows us to efficiently estimate the conductivity map. In addition, based on the estimated conductivity, realistic electrograms can be regenerated demonstrating the validity of the model.

### 4.1. INTRODUCTION

Atrial fibrillation (AF) is a common age-related cardiac arrhythmia characterized by rapid and irregular electrical activity of the atria. In Europe, 1 to 3 % of the population (more specifically elderly) suffer from AF. These patients have five times higher risk of strokes,

---

This chapter is based on the article published as "A compact matrix model for atrial electrograms for tissue conductivity estimation" by B. Abdi, R.C. Hendriks, A.-J. van der Veen, N.M. de Groot, Computers in Biology and Medicine, 2019, 107 , pp.284-291.

especially ischemic stroke with higher death rate or worse prognosis at higher cost [2]. The development and progression of AF is rooted in impaired electrical conduction and structural damage of atrial tissue, known as electropathology. Electrograms recorded during surgery or high-resolution mappings of the entire atria can help to localize and quantify the degree of electropathology and to stage AF [5, 10]. However, the analysis of the electrograms is currently constrained by the lack of suitable methods that can reveal the hidden electrophysiological parameters of the tissue. These parameters can be used as local indication of electropathology in the tissue. The lack of such methods also limits the success rate of some AF therapies, e.g., electrogram-based ablation that targets areas with complex fractionated electrograms. This happens due to the inhomogeneity and complexity in defining fractionation and its relation to pathological causes in tissue [31].

4

Currently, cardiologists mostly analyze the electrical propagation and electropathology based on local activation times (ATs) and local conduction velocities (CVs), defined as the distance traveled by the depolarization wavefront in a unit of time. However, the interpretation of these propagations, due to the interaction of many parameters, is quite complex, needs expert intervention and is time varying (from beat-to-beat during AF). The changes in conduction velocities may have multiple causes of both pathologic and non-pathologic origin; even pathological causes might not be local and might origin from a different area in the atrium. For example, in a two-dimensional (2D) isotropic and homogeneous tissue, the changes in the propagation velocity from the steady state velocity (for flat wavefront propagation) have a linear relationship with the local curvature [44]. In general, concave wavefronts propagate faster than convex wavefronts without having any pathological causes. This is actually due to the amount of local excitatory current supplied by the cells at the wavefront compared to the membrane area downstream that will be excited next. CV also depends on the pacing cycle length and typically decreases for shorter cycles without indicating electropathology in the tissue [45].

The electrical propagation in tissue is governed by electrophysiological models and is directly connected to its underlying parameters. Particularly, the propagation is correlated to the tissue intracellular conductivity. It plays an important role in the underlying dynamics and functional connections in the tissue as a mechanism of inter-cellular communication. The estimation of these hidden parameters can be essential in the diagnosis and staging of the disease. Moreover, the developed physiological models can potentially be used for testing and determining appropriate treatments, e.g., guiding the electrogram based ablation therapies. Unlike CV, analyzing tissue conductivity does not require expert intervention and it can be correlated to local electropathology. As an example, it has been shown in previous studies [46, 47] that one way to represent fibrosis (as the hallmark of electropathology and AF progression) in computer models of AF is via slow conductivities. Despite the beneficial effect of conductivity in analyzing electropathology, the complexity of the electrophysiological models makes its estimation challenging and not practical in clinical settings.

Realistic computer electrophysiological models of electrograms during sinus rhythm (SR) and AF have been developed in [13, 14, 16]. The results show that an analysis of the morphology of a single electrogram can provide useful information about the substrate maintaining AF. This detailed model is very useful for analyzing the effect of tissue properties like anisotropy and heterogeneity on the resulting electrograms. However, using this

model in the inverse problem of extracting tissue properties from electrograms is nearly impossible due to the large number of parameters that need to be estimated. In another study [48], the tissue conductivity map is directly estimated from cellular action potentials (APs) recorded by high resolution micro-electrode arrays, which is not practical for living human tissue. In [49, 50], a quite different approach was used based on Eikonal equations to approximately model the cells' activation times, based on the apparent conductivity while ignoring all the microscopic details of the process, including cellular potentials and electrograms.

Our hypothesis is that understanding atrial fibrillation and improving AF therapy starts by developing a proper forward model that is accurate enough (from a physiological point of view) and simultaneously simple enough to allow for subsequent parameter estimation. Thus, the main focus of this chapter is on developing a simplified forward model that can efficiently explain the observed electrogram morphology based on the tissue conductivity. Using a parsimonious parametrization, this model can then be used in the inverse problem of estimating tissue conductivity as an indicator of electropathology.

The remainder of this chapter is organized as follows. In Section 4.2 we present the electrophysiological models that describe the electrical propagation and electrogram generation in cardiac tissue. Next, we introduce a simplified matrix model for the electrogram, formulated in terms of two parameter vectors: the activation times and the tissue conductivity map. In Section 4.3 we formulate the inverse problem of conductivity estimation and present initial algorithms for solving the problem. In Section 4.4 we demonstrate the performance of our proposed approach on simulated data and compare its results with two other reference approaches. In Section 4.5 we apply these algorithms to clinically recorded data, and demonstrate their effectiveness in the analysis of real data. We conclude in Section 4.6, and discuss possible future directions.

## 4.2. ELECTROGRAM MODEL

### 4.2.1. ACTION POTENTIAL PROPAGATION AND ELECTROGRAM MODELS

As shown in Section 2.5.2, action potential propagation in the tissue is governed by the following reaction-diffusion equation that models the membrane current as a function of three currents,

$$C \frac{\partial V(\mathbf{x}, t)}{\partial t} = I_{\text{tm}}(\mathbf{x}, t) + I_{\text{st}}(\mathbf{x}, t) - I_{\text{ion}}(\mathbf{x}, t, V). \quad (4.1)$$

We also showed in Section 2.5.3 that for a 2D tissue where the modeled cells are located within the area  $A_0$ , the electrogram model is [13]

$$\Phi(\mathbf{y}, t) = \frac{1}{4\pi\sigma_e} \int_{A_0} \frac{I_{\text{tm}}(\mathbf{x}, t)}{\|\mathbf{y} - \mathbf{x}\|} dA(\mathbf{x}), \quad (4.2)$$

with its space-discretized version representation as,

$$\Phi_m(t) = \frac{1}{4\pi\sigma_e} \sum_{n=1}^N \frac{I_{\text{tm}}(\mathbf{x}_n, t)}{r_{m,n}} a, \quad (4.3)$$

where  $I_{\text{tm}}(\mathbf{x}_n, t)$  is the space-discretized representation of all cellular transmembrane currents and is given by

$$\begin{aligned} I_{\text{tm}}(\mathbf{x}_n, t) &= S_v^{-1} \nabla \cdot \boldsymbol{\Sigma}_n \nabla V_n(t) \\ &= S_v^{-1} \left( \frac{\partial}{\partial x} \left( \sigma_{xx,n} \frac{\partial V_n}{\partial x} \right) + \frac{\partial}{\partial x} \left( \sigma_{xy,n} \frac{\partial V_n}{\partial y} \right) + \frac{\partial}{\partial y} \left( \sigma_{yx,n} \frac{\partial V_n}{\partial x} \right) + \frac{\partial}{\partial y} \left( \sigma_{yy,n} \frac{\partial V_n}{\partial y} \right) \right) \end{aligned} \quad (4.4)$$

where  $\boldsymbol{\Sigma}_n \equiv \boldsymbol{\Sigma}(\mathbf{x}_n)$  is the tissue conductivity (see Section 4.2.3 for more details), and  $V(\mathbf{x}_n, t) \equiv V_n(t)$ . By stacking all cellular potentials at time instant  $t$  in a vector  $\mathbf{v}(t) = [V_1(t), \dots, V_N(t)]^T$  and likewise for the currents  $\mathbf{i}_{\text{tm}}(t) = [I_{\text{tm},1}(t), \dots, I_{\text{tm},N}(t)]^T$ , Eq. (4.4) can be expressed in a space-discretized vector form as

$$\mathbf{i}_{\text{tm}}(t) = S_v^{-1} \mathbf{D}_{\boldsymbol{\sigma}} \mathbf{v}(t). \quad (4.5)$$

The linear operator  $\mathbf{D}_{\boldsymbol{\sigma}}$  in this equation equals

$$\mathbf{D}_{\boldsymbol{\sigma}} = \mathbf{D}_x \text{diag}(\boldsymbol{\sigma}_{xx}) \mathbf{D}_x + \mathbf{D}_x \text{diag}(\boldsymbol{\sigma}_{xy}) \mathbf{D}_y + \mathbf{D}_y \text{diag}(\boldsymbol{\sigma}_{yx}) \mathbf{D}_x + \mathbf{D}_y \text{diag}(\boldsymbol{\sigma}_{yy}) \mathbf{D}_y, \quad (4.6)$$

where  $\text{diag}(\cdot)$  is a diagonal matrix with its diagonal entries from the argument vector, and  $\boldsymbol{\sigma}_{xx}$ ,  $\boldsymbol{\sigma}_{xy}$ ,  $\boldsymbol{\sigma}_{yx}$  and  $\boldsymbol{\sigma}_{yy}$  are vectors stacking the corresponding conductivities of all cells. As an example,  $\boldsymbol{\sigma}_{xx} = [\sigma_{xx,1}, \sigma_{xx,2}, \dots, \sigma_{xx,N}]^T$ . Matrices  $\mathbf{D}_x$  and  $\mathbf{D}_y$  are respectively the first-order discrete spatial derivative operators in the  $x$  and  $y$  directions, where we can use a forward, backward, or central space difference scheme.

By using Eq. (4.5), we can reformulate Eq. (4.3) as

$$\Phi_m(t) = k \mathbf{r}_m^T \mathbf{D}_{\boldsymbol{\sigma}} \mathbf{v}(t), \quad (4.7)$$

where all constants are collected in  $k = a(4\pi\sigma_e S_v)^{-1}$ . This equation shows that each electrogram is a weighted sum of all cellular action potentials, where the weights depend linearly on the inverse of cell distances to the electrode and nonlinearly on their conductivities.

To develop the space-discretized matrix representation of Eq. (4.3), we stack the  $M$  electrogram signals in a single vector  $\boldsymbol{\phi}(t) = [\Phi_1(t), \dots, \Phi_M(t)]^T$ . We also define an  $M \times N$  matrix  $\mathbf{R}$  that contains all the inverse distances from electrodes to cells,  $\mathbf{R} = [\mathbf{r}_1, \mathbf{r}_2, \dots, \mathbf{r}_M]^T$ . Sampling over time, the linearized matrix representation of the electrogram array at all time instances can then be written as

$$\boldsymbol{\Phi} = k \mathbf{R} \mathbf{D}_{\boldsymbol{\sigma}} \mathbf{V}, \quad (4.8)$$

where  $\boldsymbol{\Phi} = [\boldsymbol{\phi}(0), \boldsymbol{\phi}(1), \dots, \boldsymbol{\phi}(T-1)]$  is an  $M \times T$  matrix containing all the  $M$  resulting electrograms for all time instances, and matrix  $\mathbf{V}$  contains all the cellular action potentials.

### 4.2.2. SIMPLIFIED ELECTROGRAM MODEL

Given an electrogram array  $\boldsymbol{\Phi}$ , our aim is to estimate the conductivity tensor  $\boldsymbol{\Sigma}$  from Eq. (4.8). Therefore, we first need to compute  $\mathbf{V}$  using Eq. (4.1). However, we propose to simplify the electrogram model by skipping the transmembrane potential computation in Eq. (4.1), and benefit from the observation that once activated, all cells produce almost the same stereotype AP, denoted by  $V_0(t)$ . A similar approach was first employed

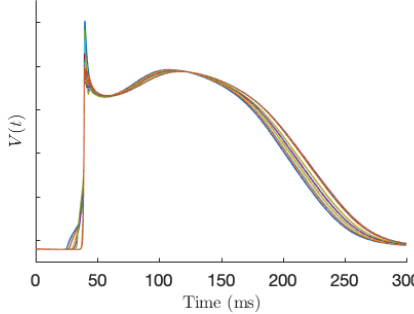


Figure 4.1: Aligned simulated APs of the 29th row of the simulated tissue M3 whose conductivity map and activation map are plotted in Fig. 4.2.

by Spach et al. in [34] to reproduce experimental electrograms using the activation times and a stereotype AP. Moreover, the same concept was used by Franzone et al. [35] to model electrograms and look at tissue properties on more complex electrogram morphologies. Both studies verify this assumption and show that it can provide realistic electrograms. To demonstrate this hypothesis, as an example, Fig. 4.1 shows all simulated action potentials in the 29th row of the anisotropic tissue M3 in Fig. 4.2. This row includes an area with slower conductivities. The APs have been aligned with respect to their ATs, annotated as the time when the cell's potential reaches a threshold value of -40mV in the depolarization phase of its AP. As can be seen, the depolarization phases of the simulated APs, that are of importance in calculating electrograms, match reasonably with each other. We will discuss the simulations in more detail in Section 4.4.

With this assumption, our proposed simplified matrix representation of Eq. (4.8) can be written as

$$\Phi = k \mathbf{R} \mathbf{D}_\sigma \mathbf{V}_\tau, \quad (4.9)$$

where the  $(n, j)$ th entry of  $\mathbf{V}_\tau$  equals  $[\mathbf{V}_\tau]_{n,j} = V_0(jT_s - \tau_n)$ , which is a time shifted and sampled version of  $V_0(t)$ ,  $\tau_n$  is the AT of cell  $n$ , and  $T_s$  is the sampling period. This also assumes each cell is activated only once (i.e., data contains a single AF cycle length). We will collect all ATs in a vector  $\tau = [\tau_1, \dots, \tau_N]^T$ . This sparse parametrization of the model in terms of  $\tau$  and  $\sigma$  opens up new possibilities for parameter estimation (conductivity) and further signal manipulations.

### 4.2.3. COMPACT MATRIX MODEL FOR ELECTROGRAMS BASED ON CONDUCTIVITY

To this end, we reformulate Eqs. (4.6) and (4.9) in the form of a measurement equation that highlights the linear dependency on the conductivity map. As a first step, the conductivity tensor can be written as

$$\Sigma_n = \begin{bmatrix} \sigma_{xx,n} & \sigma_{xy,n} \\ \sigma_{yx,n} & \sigma_{yy,n} \end{bmatrix} = \sigma_n \mathbf{A}_n \begin{bmatrix} 1 & 0 \\ 0 & \alpha_n^2 \end{bmatrix} \mathbf{A}_n^T. \quad (4.10)$$

The right-hand side of this equation represents an eigenvalue decomposition of the con-

ductivity tensor. The principal eigenvalue  $\sigma_n$  describes the conductivity in the main direction of the cell while  $\alpha_n$  defines the anisotropic ratio (for human atrial cells,  $\alpha_n$  is of the order of 0.4 in healthy tissue [49]). The columns of the orthonormal matrix  $\mathbf{A}_n$  are the eigenvectors of the conductivity tensor and define the orientation of the cell in the global coordinate system.  $\mathbf{A}_n = [\cos(\theta_n), -\sin(\theta_n); \cos(\theta_n), \sin(\theta_n)]$  is parametrized by  $\theta_n$ , a rotation angle that represents the fiber direction. The conductivity tensor can thus be written as

$$\boldsymbol{\Sigma}_n = \sigma_n \mathbf{K}_n, \quad \mathbf{K}_n = \mathbf{A}_n \begin{bmatrix} 1 & 0 \\ 0 & \alpha_n^2 \end{bmatrix} \mathbf{A}_n^T = \begin{bmatrix} \kappa_{n,1} & \kappa_{n,2} \\ \kappa_{n,3} & \kappa_{n,4} \end{bmatrix}, \quad (4.11)$$

where  $\mathbf{K}_n$  is parametrized by two parameters,  $\alpha_n$  and  $\theta_n$ .

The remaining parameters are then the cellular conductivities along the main direction, i.e.,  $\sigma_n$ . Using a stacked vector notation for all cells  $n \in \{1, \dots, N\}$  we obtain  $\boldsymbol{\sigma} = [\sigma_1, \sigma_2, \dots, \sigma_N]^T$ . Using Eq. (4.11), Eq. (4.6) can be written as

$$\begin{aligned} \mathbf{D}_{\boldsymbol{\sigma}} = & \mathbf{D}_x \text{diag}(\boldsymbol{\kappa}_1) \text{diag}(\boldsymbol{\sigma}) \mathbf{D}_x + \mathbf{D}_x \text{diag}(\boldsymbol{\kappa}_2) \text{diag}(\boldsymbol{\sigma}) \mathbf{D}_y \\ & + \mathbf{D}_y \text{diag}(\boldsymbol{\kappa}_3) \text{diag}(\boldsymbol{\sigma}) \mathbf{D}_x + \mathbf{D}_y \text{diag}(\boldsymbol{\kappa}_4) \text{diag}(\boldsymbol{\sigma}) \mathbf{D}_y, \end{aligned} \quad (4.12)$$

where as an example  $\boldsymbol{\kappa}_1 = [\kappa_{1,1}, \kappa_{2,1}, \dots, \kappa_{N,1}]^T$ . We further use a property of the Khatri-Rao product (column-wise Kronecker product) denoted by  $\circ$ , to write the vectorized form of Eq. (4.12) to express its linear dependency on  $\boldsymbol{\sigma}$ . The employed property is  $(\mathbf{B}^T \circ \mathbf{A})\mathbf{x} = \text{vec}(\mathbf{A}\text{diag}(\mathbf{x})\mathbf{B})$ , where  $\text{vec}(\cdot)$  stacks the columns of the argument matrix to form a vector. The final vectorized version of Eq. (4.12) is

$$\text{vec}(\mathbf{D}_{\boldsymbol{\sigma}}) = \boldsymbol{\Gamma} \boldsymbol{\sigma}, \quad (4.13)$$

where

$$\boldsymbol{\Gamma} = \mathbf{D}_x^T \circ (\mathbf{D}_x \text{diag}(\boldsymbol{\kappa}_1)) + \mathbf{D}_y^T \circ (\mathbf{D}_x \text{diag}(\boldsymbol{\kappa}_2)) + \mathbf{D}_x^T \circ (\mathbf{D}_y \text{diag}(\boldsymbol{\kappa}_3)) + \mathbf{D}_y^T \circ (\mathbf{D}_y \text{diag}(\boldsymbol{\kappa}_4)). \quad (4.14)$$

Using Eq. (4.13), and a property of the Kronecker product, denoted by  $\otimes$ , which is  $(\mathbf{B}^T \otimes \mathbf{A})\text{vec}(\mathbf{X}) = \text{vec}(\mathbf{A}\mathbf{X}\mathbf{B})$ , we can also present the vectorized version of Eq. (4.9) as

$$\text{vec}(\boldsymbol{\Phi}) = k(\mathbf{V}_{\boldsymbol{\tau}}^T \otimes \mathbf{R}) \text{vec}(\mathbf{D}_{\boldsymbol{\sigma}}) = k(\mathbf{V}_{\boldsymbol{\tau}}^T \otimes \mathbf{R}) \boldsymbol{\Gamma} \boldsymbol{\sigma}. \quad (4.15)$$

Finally, by writing  $\boldsymbol{\phi} = \text{vec}(\boldsymbol{\Phi})$  and defining the mixing matrix  $\mathbf{M}_{\boldsymbol{\tau}} = (\mathbf{V}_{\boldsymbol{\tau}}^T \otimes (k \mathbf{R})) \boldsymbol{\Gamma}$  of size  $MT \times N$ , the resulting linear measurement equation based on conductivity, from here on referred to as the compact matrix model for atrial electrograms (CMM), is

$$\boldsymbol{\phi} = \mathbf{M}_{\boldsymbol{\tau}} \boldsymbol{\sigma}. \quad (4.16)$$

Note that the notation in  $\mathbf{M}_{\boldsymbol{\tau}}$  hides the parameters  $\boldsymbol{\kappa}_1, \boldsymbol{\kappa}_2, \boldsymbol{\kappa}_3$  and  $\boldsymbol{\kappa}_4$  which depend on two parameters,  $\alpha_n$  and  $\theta_n$  that are assumed to be known in this study.

### 4.3. CONDUCTIVITY ESTIMATION

We have seen how the measured data ( $\boldsymbol{\phi}$  or  $\boldsymbol{\Phi}$ ) can be described in terms of a simple parametrization:  $\boldsymbol{\tau}$ ,  $\boldsymbol{\sigma}$ , and some nuisance parameters, i.e., a  $2 \times 2$  matrix  $\mathbf{K}_n$  that models the cell direction. Given the data, the inverse problem is to estimate these parameters. In particular, we are interested in the conductivity map.

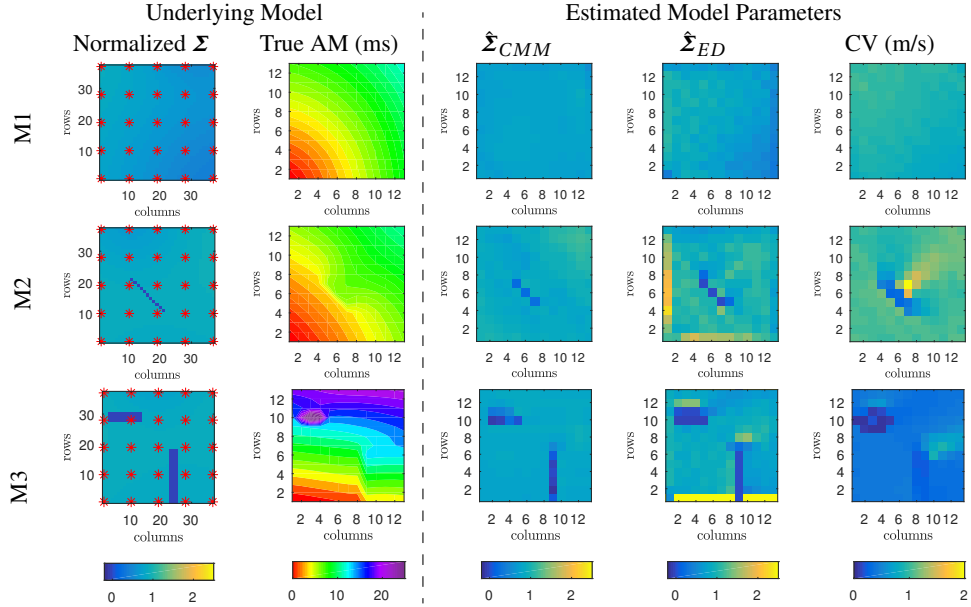


Figure 4.2: Each row of the figure demonstrates a simulated tissue and its estimated parameters. First and second columns demonstrate the underlying model including the true conductivity map and the true AM on the 2D tissue surface, respectively. In all cases the tissue is stimulated from the left bottom corner. The electrode locations are indicated by \*. The third to fifth columns demonstrate the estimated parameters including conductivity map estimated from the proposed CMM, conductivity map estimated from the Eikonal diffusion equation, and the conduction velocity map, respectively.

An initial step to reduce the number of unknowns and simplify the inverse problem is to estimate the ATs in  $\tau$  using a standard approach. In this study we estimated  $\tau$  by finding the minimum of the first time derivative of each electrogram which coincides with the activation time of the cell that is under the electrode [29]. This provides us with an incomplete activation map (AM) where the values are only known for cells that are under the electrodes. Next, we linearly interpolate the incomplete AM to provide a higher resolution AM for modeled cells. This provides a good estimation of ATs when the wavefront is rather smooth and there is only one single wavefront, that is mostly the case during SR. However, our simulation showed that in case of multiple wavefronts or existing blocks in the tissue, that is the case during AF, the activation time estimation using the minimum of the first time derivative of electrograms is less precise and better estimation methods are required. This is discussed in more detail in Chapter 5.

Assuming  $\tau$  is known, the next step is to estimate  $\sigma$  using Eq. (4.16). The amount of data is  $M \times T$  while the number of unknown parameters is a function of the chosen spatial resolution, i.e., the modeled number of cells  $N$ . As they are both on a regular grid, we can define the ratio of the number of cells to the number of electrodes as the “oversampling ratio”  $L^2$ . The number of unknowns in this step ( $\sigma$ ) is then equal to  $L^2 M$ . We would expect the number of data samples to be easily larger than the number of unknowns ( $T \gg L^2$ ), but unfortunately, most time-domain samples are not very informative. Thus, the mixing matrix

$\mathbf{M}_\tau$  is ill-conditioned or ill-posed, in particular for larger  $L$ . This issue always arises when we discretize and solve an inverse problem that has (i) the form of a first-kind Fredholm integral equation (Eq. (4.2)), and (ii) has a Laplacian operator (Eq. (4.1)) in its forward model.

Estimation of the conductivity map  $\boldsymbol{\sigma}$  is based on the linear measurement model Eq. (4.16). Since the mixing matrix is ill-conditioned, simply inverting  $\mathbf{M}_\tau$  produces an unstable solution. Therefore, regularization is needed, which is equivalent to bringing in some prior information to penalize implausible solutions. Our experiments show that, in general, the conductivity in each small enough anatomical site varies smoothly around an average value  $\mu_\sigma$  creating a smooth (low rank) conductivity map  $\boldsymbol{\Sigma}$  of size  $r_c \times c_c$ , where  $\boldsymbol{\sigma} = \text{vec}(\boldsymbol{\Sigma})$ . These smooth variations can partly be due to the changes in the properties of many cells in the real 3D tissue that are only modeled by a few cells on the 2D recording area. Notice that the changes in the conductivities of different anatomical sites can also be modeled by setting different values for  $\mu_\sigma$  with respect to our prior knowledge of the recording site. On the other hand, in cases of functional or pathological problems, a local conductivity  $\sigma_n$  could be much smaller than the average  $\mu_\sigma$ , resulting in a conductivity block that causes irregular AP wavefront propagation or even results in formation of multiple wavefronts.

These observations encourage regularization conditions that promote a sparse and low-rank solution for  $\boldsymbol{\Sigma}$ . Among many possibilities, we will consider the following regularized cost function for estimation of conductivity:

$$J(\boldsymbol{\sigma}) = \|\boldsymbol{\phi} - \mathbf{M}_\tau \boldsymbol{\sigma}\|_2^2 + \lambda_1 \|\boldsymbol{\sigma} - \mu_\sigma \mathbf{1}\|_1 + \lambda_2 \|\boldsymbol{\Sigma} - \mu_\sigma \mathbf{1}\mathbf{1}^T\|_*, \quad (4.17)$$

where  $\lambda_1$  and  $\lambda_2$  are the regularization parameters, and  $\mathbf{1}$  is the all-ones vector. The  $\ell_1$ -norm regularization term,  $\|\cdot\|_1$ , promotes a sparse solution, whereas the nuclear norm  $\|\cdot\|_*$  (the sum of singular values of its argument) promotes a smooth low-rank conductivity map. Notice that for applications in which we are more interested in localizing conductivity blocks in tissue, we can ignore the smooth low-rank regularization and only penalize the optimization problem using the  $\ell_1$ -norm which means setting  $\lambda_2 = 0$ .

In this chapter we solve Eq. (4.17) using the Split Bregman algorithm [51] which leads to the following augmented Lagrangian optimization problem,

$$\begin{aligned} \hat{\boldsymbol{\sigma}} = \arg \min_{\boldsymbol{\sigma}, \mathbf{p}, \mathbf{Q}} & \|\boldsymbol{\phi} - \mathbf{M}_\tau \boldsymbol{\sigma}\|_2^2 \\ & + \lambda_1 \|\mathbf{p}\|_1 + \mu_1 \|\mathbf{p} - (\boldsymbol{\sigma} - \mu_\sigma \mathbf{1}) - \mathbf{b}_1\|_2^2 + \lambda_2 \|\mathbf{Q}\|_* + \mu_2 \|\mathbf{Q} - (\boldsymbol{\Sigma} - \mu_\sigma \mathbf{1}\mathbf{1}^T) - \mathbf{B}_2\|_2^2, \end{aligned} \quad (4.18)$$

where the  $\mathbf{p}$  and  $\mathbf{Q}$  are the introduced auxiliary variables,  $\mu_1$  and  $\mu_2$  are penalization parameters, and  $\mathbf{b}_1$  and  $\mathbf{B}_2$  are the Lagrange multipliers. The Split Bregman algorithm then solves this problem iteratively by breaking it into smaller problems, which are simpler to implement. In each step of each iteration, one unknown parameter is updated by minimizing Eq. (4.18) while assuming the other unknowns are constant. For more detail on solving each step we refer to [52]. Overall the algorithm has a fast convergence rate to a reasonable precision in practice.

## 4.4. SIMULATION RESULTS

To demonstrate the performance of the proposed conductivity map estimation algorithm, we have simulated 2D phantom tissue areas of  $90 \times 90$  cells with  $\Delta l_0 = 0.02$  cm cell-to-

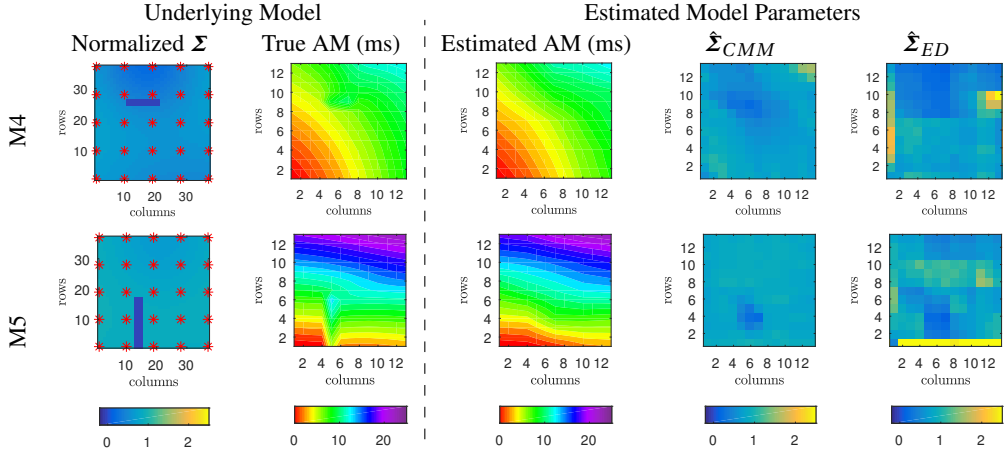


Figure 4.3: Each row of the figure demonstrates a simulated tissue and its estimated parameters. First and second columns demonstrate the underlying model including the true conductivity map and the true AM on the 2D tissue surface respectively. In each case the tissue is stimulated from the left bottom corner and the electrode locations are indicated by \*. The third to fifth columns demonstrate the estimated parameters including the estimated AM, the estimated conductivity map from the proposed CMM, and the estimated conductivity map from the Eikonal diffusion equation.

cell distances on the grid, based on examples of real tissue. Each simulated tissue has a different conductivity map with a smooth background and zero, one or two conductivity blocks in it that are respectively shown in the first column of Fig. 4.2 and are denoted by M1, M2, and M3. Notice that the plots only demonstrate the  $37 \times 37$  central cells where a  $5 \times 5$  electrode array with inter-electrode distance of  $3\Delta l_0$  was positioned. The electrode locations are shown by the \*. The tissues are stimulated with a stimulation current injected to the cell at the left bottom of the tissue. The tissues in M1 and M2 are isotropic ( $\alpha_n = 1$ ) while the tissue in M3 is anisotropic with  $\alpha_n = 0.4$ . In all simulations  $\mathbf{A}$  equals the identity matrix indicating that the main direction of the cells is along the  $x$ -axis. Eq. (4.1) was used to calculate the propagation of the APs on the tissue with a fixed time step  $T_s = 0.01\text{ ms}$ . The resulting activation maps in the selected areas are also shown in the second column of Fig. 4.2. Eq. (4.8) was next used to calculate the electrograms recorded by the electrode array. Since this high temporal resolution complicates the subsequent parameter estimation, the resulting electrograms and the stereotype  $V_0(t)$  were down-sampled by a factor of 5, which increases the sampling period of the data to  $T_s = 0.05\text{ ms}$ . Note that we made sure the upstroke phase of  $V_0(t)$  is preserved after down-sampling.

We then use Eq. (4.18) to estimate the conductivity maps of each tissue, assuming that the isotropic ratio  $\alpha_n$  and fiber rotation angle  $\theta_n$  are known and constant (the same values that were used in generating the data). To reduce the number of unknowns, the modeled cell size in the inverse problem was considered three times bigger than the initial cell size used in the forward model simulation. The inter-electrode distance was considered three times the modeled cell size ( $L = 3$ ), i.e., nine times the initial cell size. To focus on the performance of the conductivity map estimation algorithm itself, and to avoid the errors in AT estimations, we use the real ATs in this simulation. For each modeled cell, we

used the activation time of the central cell of the  $3 \times 3$  block of initial cells that it covers. Obviously using the ATs estimated from electrograms and interpolating them for higher resolution modeled cells introduces inaccuracies in estimating the conductivity map. We will later demonstrate how these inaccurate ATs affect the conductivity estimation. The equations derived in Section 4.2.3 were then used to calculate the mixing matrix  $\mathbf{M}_r$ , and finally Eq. (4.18) was used to estimate the conductivity maps. The resulting conductivity maps  $\hat{\Sigma}_{CMM}$  are shown in the third column of Fig. 4.2. Since the focus of this study is on introducing the model itself and not on optimal tuning of its parameters, we used values that yielded visually good results in all simulations, which are,  $\lambda_1 = 1e9$ ,  $\lambda_2 = 1e8$ ,  $\mu_1 = 1e4$ ,  $\mu_2 = 1e4$ ,  $\mu_\sigma = 0.9$ , and the number of iteration  $N_{itr} = 100$ .

For reference, we use the apparent conductivity map estimation using the Eikonal-diffusion (ED) equation [50]. To the best of our knowledge, this is the only similar approach that estimates electrical conductivity map and is also applicable to our data. We also provided the local conduction velocity map [53] as a commonly used approach in the literature for analysis of slow conduction and conduction block in tissue. CV for each cell is determined as the length of the wavefront propagation velocity vector with its two elements along the rows and columns direction. The velocity in rows (columns) direction is computed as the cell-to-cell distance over the activation time delay between the cell and its neighbouring cell in the next row (column). This is because in all our AMs the propagation is along the increasing rows and/or columns direction.

Notice that unlike CMM and ED, CV does not provide a measurement of conductivity but only measures the local velocity of the wavefront propagation. The estimated CV map and the estimated conductivity map from the ED equation, are also plotted in the right two columns of Fig. 4.2. As shown in the figure, the CV map only provides an overview of areas with fast and slow conduction which cannot be directly connected to tissue conductivity and thus electropathology in tissue. ED, on the other hand, performs well for isotropic and rather homogeneous tissues, but provides inaccurate results around boundaries of the tissue (case M1 and M2), the main diagonal of the coordinate system, and around the boundaries of the blocks. It also completely fails to provide any reliable results in case of anisotropic tissue, which is the case shown in M3. The results in general show that the proposed method outperforms the two reference methods.

Fig. 4.3 demonstrates two other examples, denoted by M4 and M5. Different from the simulation in Fig. 4.2, the conductivities are now estimated using the ATs that are estimated from low resolution electrograms instead of using the true ATs. The ATs are estimated by finding the minimum of the first time derivative of electrograms, and linearly interpolated to obtain a higher resolution activation map for all modeled cells. The tissue in M4 is isotropic while the tissue in M5 is anisotropic. All other parameters used in these simulations are equal to those used in generation of Fig. 4.2 and only the conductivity maps are different, which are plotted in the first column of Fig. 4.3. The ground truth ATs and the estimated ATs from electrograms are also shown in Fig. 4.3. The proposed CMM and ED were used for estimation of conductivity and the results are shown in the last two columns of Fig. 4.3 respectively. Notice that we did not include CV in this figure. As can be seen, by comparing the estimated AM with the true AM, the estimated ATs are less accurate in areas with blocks. These inaccurate estimations cause the blocks to appear much smoother, or they are even missed. This can also be affected by the size of the block and its geometry with

respect to the wavefront propagation direction. As shown in the simulations, the proposed CMM performs better than the ED because it also depends on the final electrograms and not only on the estimated ATs.

Fig. 4.4 demonstrates the robustness of the model with respect to inaccurate local activation times. The first row shows the estimated conductivity map and conduction velocity map of the simulated tissue M2 that was already presented in Fig. 4.2. The second to fourth row present three realizations of parameter estimation when uniformly distributed random errors in range of  $[-\varepsilon_m, \varepsilon_m]$  ms are added to the true activation times. Note that the average delay between two neighboring modeled cells in the true activation map is about 0.5 ms. The conduction velocity maps are provided for comparison. As can be seen, the conductivity map is less affected by the errors in activation times than CV map due to: (i) its dependency on the electrograms morphology and not only on the estimated activation times, and (ii) the regularization terms in conductivity estimation using Eq. (4.17).

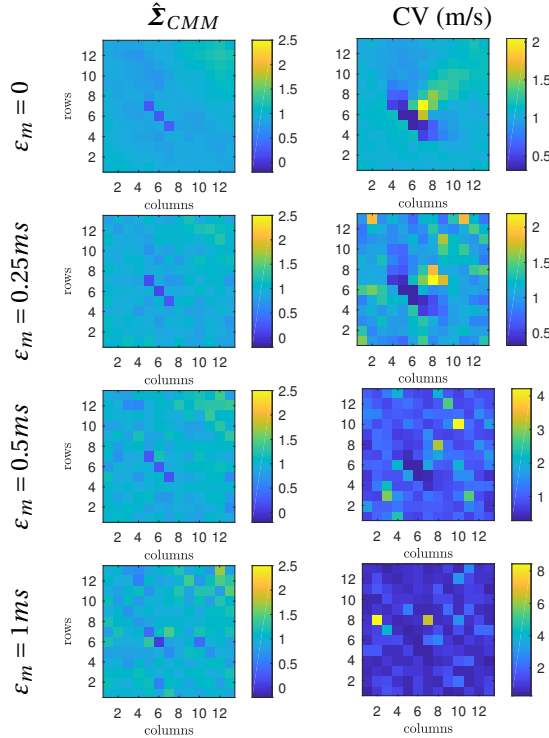


Figure 4.4: The first row demonstrates the estimated conductivity map (using the proposed approach) as well as the estimated conduction velocity map for the simulated electrograms already presented in M2 in Fig. 4.2. The second to fourth row show the same estimated parameters, where uniformly distributed local error, in range of  $[-\varepsilon_m, \varepsilon_m]$ , are added to the true activation times.

## 4.5. EXPERIMENTS ON CLINICAL DATA

In this section we apply the proposed method to clinically recorded data. The epicardial electrograms used in this study were recorded using a 192-unipolar electrode array ( $8 \times 24$ ) with 2 mm inter-electrode distance and 0.45 mm electrode diameter. The electrode array is subsequently positioned on 9 mapping atrial sites using the anatomical borders, visually by the surgeon. The array records 5 seconds of sinus rhythm and 10 s of induced atrial fibrillation (IAF) signals at each site. This technique was performed in more than 400 patients of 18 years and older, with coronary and/or structural heart disease, with or without AF, electively scheduled for cardiac surgery and a ventricular ejection fraction above 40%. We have selected four representative patients from the database denoted by P1 to P4, and only used the signals recorded from a fixed location in the middle of the right atrium. The electrograms for P1 to P3 are recorded during SR, and the electrograms for P4 are recorded during IAF. The acquired signals are amplified, filtered (bandwidth 0.5 to 400 Hz), sampled (1 kHz), analogue to digital converted (16 bits) and recorded on a hard disk. More details on the mapping approach and the electrode array specifications can be found in [5].

Before employing Eq. (4.18) to estimate the tissue conductivity, we need to perform some preparation steps. First the tissue surface is meshed with a 2D mono-layer grid where each element on the grid is assumed to be a cell. Although a smaller cell size provides a more accurate estimation of conductivity, to avoid numerical complications and reduce the number of unknowns in our model, we select the largest possible cell size that still reasonably models the electrograms. Therefore, in our simulations the modeled cell size equals  $\Delta l = 0.2/3 = 0.067\text{cm}$  which is one third of the inter-electrode distance leading to  $L = 3$ . After gridding the tissue surface the inverse of the cell to electrode distances are calculated and stored in the matrix  $\mathbf{R}$ .

The ATs are estimated using the maximum negative slope of the electrograms followed by a 2D interpolation. This provides good estimates of the ATs under the assumption of SR, and a single smooth wavefront which holds for the P1 to P3. The resulting activation maps are demonstrated in Fig. 4.5, where the electrode locations are marked by the \*. We also use the same approach to estimate the ATs for P4 whose activation map is demonstrated in Fig. 4.6. As can be seen, two wavefronts enter the recording area and collide, and as a result, some electrograms are fractionated. This implies that our approach might provide faulty and smooth ATs that will eventually affect the estimation of conductivity map as already demonstrated in simulated tissues in Fig. 4.3.

After completing the activation map, we can build  $\mathbf{V}_\tau$  in Eq. (4.9) by shifting the stereotype  $V_0(t)$  with respect to the estimated ATs. The matrix  $\Phi$  containing the recorded electrograms was initially normalized to have a zero average and a minimum to maximum amplitude of 1. Although we have not measured the tissue fiber direction at the recording site,  $\mathbf{A}_n = \mathbf{I}$  for all cells seems reasonable enough with respect to the isochrones geometry. Since the conduction velocity across the  $x$ -axis is almost twice its value across the  $y$ -axis, we set  $\alpha_n^2 = 0.25$ . After calculating all necessary parameters, the equations used in Section 4.2.3 were employed to compute the mixing matrix  $\mathbf{M}_\tau$  with  $k = 1/300$ . Finally, Eq. (4.18) was used to estimate the conductivity map which are demonstrated in the second column of Fig. 4.5 and Fig. 4.6. The optimization parameters used in these simulations are  $\lambda_1 = 2$ ,  $\lambda_2 = 2$ ,  $\mu_\sigma = 0.8$ ,  $\mu_1 = 1$ ,  $\mu_2 = 1$ ,  $N_{\text{itr}} = 100$ . Note that such ranges of variation in the conductivity within a small area is acceptable, as demonstrated in a previous study on

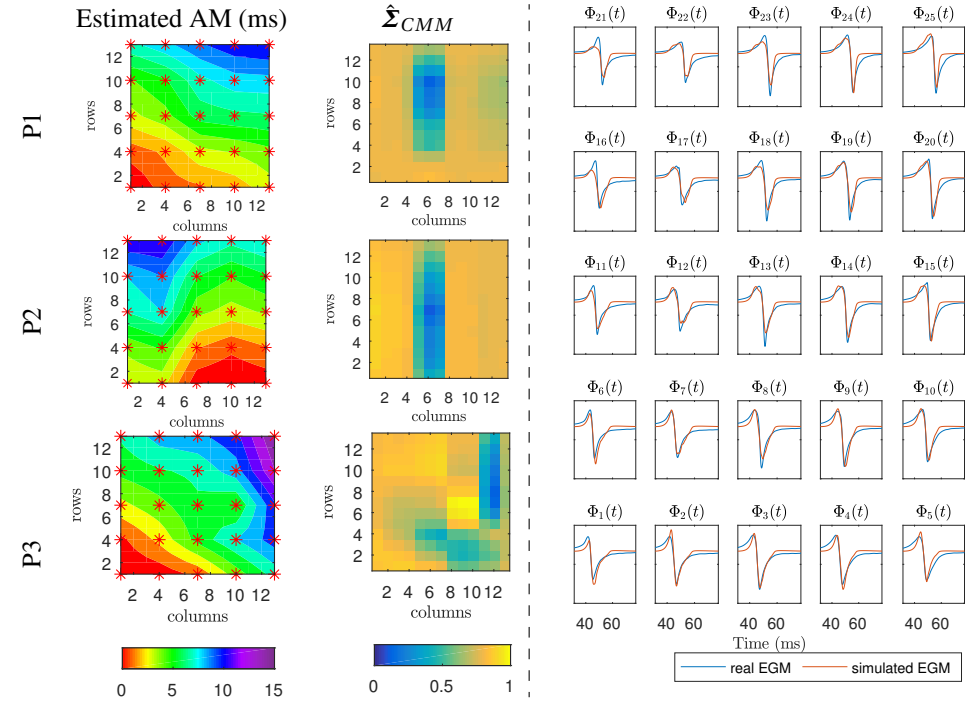


Figure 4.5: The estimated activation map (first column) as well as the estimated conductivity map (second column) from the electrograms recorded at the right atrium of three different patients during one heart beat in SR. The electrode locations are indicated by \*. Clinically recorded electrograms of patients P1, as well as the simulated electrograms using the proposed approach, are also demonstrated in the third column.

similar clinical mapping data [54]. However, these ranges can be further improved by the correct tuning of the regularization parameters. This is deferred to future work.

There is no ground truth to compare the conductivity map to. Therefore, to demonstrate the performance of the model, Fig. 4.5 also shows the  $5 \times 5$  clinically recorded electrograms, as well as the modeled electrograms for the same recording in P1. Fig. 4.6 also demonstrates the recorded and simulated electrograms of P4 during IAF. The estimated  $\sigma$  in combination with the proposed CMM in Eq. (4.16) were used to generate the modeled electrograms. As we can see, despite the low gridding resolution and all simplifications we made in this study, the real and modeled signals match reasonably, especially around the AT of each electrogram. For IAF data in P4, the approach can, to some extent, follow the morphology of the fractionated electrograms, except for the sharp deflections as in  $\Phi_6$ . This is partly due to the errors in AT estimation of the fractionated electrograms, and the smooth changes in the AM due to linear interpolations. Moreover, since the electrical propagation outside the boundaries of the simulated tissue is neglected, the simulated electrograms at the boundaries are less accurate.

4

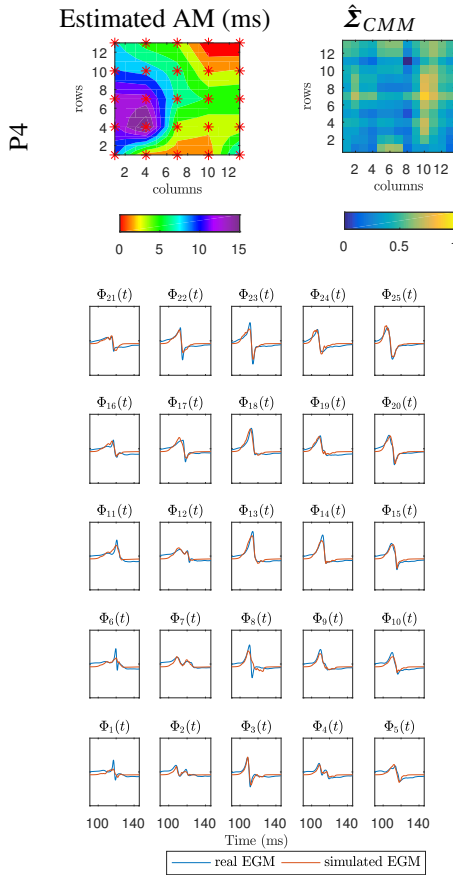


Figure 4.6: The estimated activation map (top left) as well as the estimated conductivity map (top right) from the recorded electrograms during induced AF. The recorded electrograms of each electrode as well as the simulated electrograms are also plotted.

## 4.6. DISCUSSION AND CONCLUSIONS

In this study we developed a compact matrix model for atrial electrograms CMM to show its linear dependence on the conductivity vector, enabling the estimation of this parameter from the recorded electrograms. The results show that despite the low resolution and all simplifying assumptions, the model can efficiently estimate the conductivity map and regenerate realistic electrograms, specially during sinus rhythm. We also provided the results of two other approaches, namely, conductivity estimation based on Eikonal-diffusion equation and conduction velocity estimation. The provided examples show that our method outperforms the other two approaches especially in case of anisotropy and inhomogeneity in the tissue.

However, we need to acknowledge that the presented algorithm may not perform well in cases where our underlying assumptions are not valid. These can happen in two cases.

First, when the wavefront is not smooth, as is the case during AF. In this case, multiple wavefronts enter the area of interest simultaneously or one wavefront breaks into multiple wavelets due to the inhomogeneity in the conductivity. This complicates the estimation of the activation times and results in an inaccurate activation map and consequently an inaccurate conductivity map. Therefore, more robust AT estimation algorithms need to be developed. Second, for 3D tissues where each layer of tissue might have a different conductivity map and wavefront propagation. In this case our model, like any other approach that uses electrograms, images all the activities on the 2D tissue surface and ignores the underlying layers and is therefore not valid. Although this can be partly solved by developing 3D models of the tissue following the same principles as 2D, the main problem would be the estimation of the ATs in the underlying layers which is currently not possible in clinical recordings.

Future work therefore includes the development of a better algorithm for the estimation of ATs, analyzing the efficiency and accuracy of various alternative regularization functions and algorithms for solving the inverse problem, as well as a discussion on the selection of the regularization parameters.



# 5

## IMPROVED LOCAL ACTIVATION TIME ANNOTATION OF FRACTIONATED ELECTROGRAMS

Local activation time (LAT) annotation in unipolar electrograms is complicated by interference from nonlocal atrial activities of neighboring tissue. This happens due to the spatial blurring that is inherent to electrogram recordings. In this study, we aim to exploit multi-electrode electrogram recordings to amplify the local activity in each electrogram and subsequently improve the annotation of LATs. An electrogram array can be modeled as a spatial convolution of cellular transmembrane currents with an appropriate distance kernel, which depends on the cells' distances to the electrodes. By deconvolving the effect of the distance kernel from the electrogram array, we undo the blurring and estimate the underlying transmembrane currents as our desired local activities. However, deconvolution problems are typically highly ill-posed and result in unstable solutions. To overcome this issue, we propose to use a regularization term that exploits the sparsity of the first-order time derivative of the transmembrane currents. We perform experiments on simulated two-dimensional tissues, as well as clinically recorded electrograms during paroxysmal atrial fibrillation. The results show that the proposed approach for deconvolution can improve the annotation of the true LAT in the electrograms. We also discuss, in summary, the required electrode array specifications for an appropriate recording and subsequent deconvolution. By ignoring small but local deflections, algorithms based on steepest descent of the electrogram deflection are prone to generate smoother activation maps. However, by exploiting

---

This chapter is based on the article published as "Improved local activation time annotation of fractionated atrial electrograms for atrial mapping" by B. Abdi, R.C. Hendriks, A.-J. van der Veen, N.M. de Groot, in Computers in Biology and Medicine, 2020, 117, p.103590.

multi-electrode recordings, we can efficiently amplify small but local deflections and reveal new details in the activation maps that were previously missed.

## 5.1. INTRODUCTION

Atrial electrograms (EGMs) recorded during high resolution atrial mapping, as well as their corresponding activation maps, facilitate the identification and localization of potential triggers and substrates perpetuating atrial fibrillation (AF). They can also be used to guide cardiologists through treatment approaches such as EGM based ablation therapies [11].

An EGM recording is an aggregation of the cellular activities that are in the neighborhood of an electrode. How strong each individual cell contributes to the total aggregated potential depends on the distance of the cell to the electrode, as well as on the electrode dimension [55]. The depolarization wavefront propagation in a rather homogeneous tissue with a uniform excitation wavefront results in a smooth stereotype atrial activity: a positive spike followed by a negative deflection in unipolar EGMS. In these cases, the local activation time (LAT) of the cells that are right under the electrode coincides with the maximum negative deflection or the steepest descent (SD) of the electrogram.

However, if the tissue is inhomogeneous or multiple excitation wavefronts are propagating in the electrode neighborhood, the recorded EGM may contain nonlocal (far-field) deflections from the so called “distant active membrane” [56]. In such cases, the steepest descent annotated as the LAT might belong to a far-field excitation and not to the local activity. This makes the estimation of LATs prone to errors and will negatively affect the estimation of other parameters that depend on LATs, such as conduction velocity or tissue conductivity [57]. This, in turn, complicates the analysis of EGM recordings and the underlying atrial substrate for AF by adding confusion about the origin of observed components [58]. As shown in a study on bipolar electrograms in [59], 67% of complex fractionated electrograms represent nonlocal activities and are thus not consistent with spatial disorganization in the tissue.

To attenuate the effect of nonlocal activities, bipolar electrograms are alternatively used in many studies. However, these recordings suffer from serious drawbacks including sensitivity to propagation direction and inability to provide no useful information about the potential distribution in the electrogram. Many other studies directly focus on improving LAT estimation in fractionated atrial electrograms. A review of such methods can be found in [29]. Some of these approaches try to make use of spatial information offered by multi-electrode recordings. These include application of cross-correlation, spatial filtering, spatial gradient or spatial deconvolution, among which only the spatial deconvolution is formulated according to an electrophysiological model of the tissue. It benefits from the fact that a multi-electrode electrogram recording can be modeled as a convolution of the cellular transmembrane current with a spatial filter that depends on the electrode diameter and its distance to the cells [60].

In this chapter, we also exploit the convulsive electrogram model for a better annotation of the local deflection (and respectively the local activation time) in fractionated electrograms. We first present a model for the EGM array that reflects the spatial convolution. By employing this model, we formulate a deconvolution problem to estimate the local activities. However, the deconvolution problem is under-determined and results in unstable solutions. To overcome this issue, some studies employ prior knowledge such as planar

wavefront propagation [60]. Other studies use spatial interpolation and filtering to artificially introduce more data points [55]. None of the assumptions in these approaches are satisfactory from a physiological point of view. In this chapter, we propose to use a regularization based on sparsity of the first-order time derivative of the electrograms to solve the inverse problem of local activity estimation. We solve the proposed deconvolution problem using the Split Bregman method [51]. Overall, the approach is computationally efficient, does not suffer from boundary artifacts, and can also perform with incomplete observations. Our results on simulated and clinically recorded data show that the proposed approach can efficiently amplify the local activities in an EGM and outperforms the reference approaches in LAT estimation.

## 5.2. METHOD

### 5.2.1. ACTION POTENTIAL PROPAGATION

As shown in Section 2.5.2, an electrogram is the record of changes in the potentials of the many cells surrounding an electrode. These changes in cellular potentials are the result of action potential propagation in the tissue. This propagation in a two-dimensional (2D) tissue can be modeled using the following reaction-diffusion equation [12]

$$C \frac{\partial V(x_c, y_c, t_c)}{\partial t} = I(x_c, y_c, t_c) + I_{\text{st}}(x_c, y_c, t_c) - I_{\text{ion}}(x_c, y_c, t_c, V), \quad (5.1)$$

where  $V(x_c, y_c, t_c)$  is the cellular potential at location  $(x_c, y_c)$  and time  $t_c$ ,  $C \approx 1 \mu\text{Fcm}^{-2}$  is the total membrane capacitance,  $I_{\text{st}}$  is the stimulus current, and  $I_{\text{ion}}$  is the total ionic current computed according to the Courtemanche model in [33]. The transmembrane current is given by,

$$I(x_c, y_c, t_c) = S_v^{-1} \nabla \cdot \Sigma(x_c, y_c) \nabla V(x_c, y_c, t_c), \quad (5.2)$$

where  $S_v \approx 0.24 \mu\text{m}^{-1}$  is the cellular surface-to-volume ratio, and  $\Sigma(x_c, y_c)$  the intracellular conductivity tensor.

### 5.2.2. ELECTROGRAM MODEL

An electrogram can be modeled as the weighted summation of cellular transmembrane currents. The weights are equal to the inverse of the cell-to-electrode distance. The distance between a cell at position  $(x_c, y_c)$  and an electrode at position  $(x_m, y_m)$  and a (constant) height  $z_0$  above the 2D tissue equals  $\sqrt{(x_c - x_m)^2 + (y_c - y_m)^2 + z_0^2}$ . The electrogram can thus be modeled as [12]

$$\phi(x_m, y_m, t_c) = \frac{1}{4\pi\sigma_e} \int_{\mathcal{A}} \frac{I(x_c, y_c, t_c)}{\sqrt{(x_c - x_m)^2 + (y_c - y_m)^2 + z_0^2}} dA(x_c, y_c), \quad (5.3)$$

for  $m = 1, 2, \dots, M$ , where  $M$  is the total number of electrodes,  $\mathcal{A}$  is the area in which the modeled cells are located,  $A(x_c, y_c)$  is the area variable, and  $\sigma_e$  is the constant extra-cellular conductivity.

Eq. (5.3) represents a 2D spatial convolution of  $I(x_c, y_c, t_c)$  with a distance kernel  $R_0$  given by

$$R_0(x_c, y_c) = \frac{1}{\sqrt{x_c^2 + y_c^2 + z_0^2}}. \quad (5.4)$$

A plot of  $R_0$  is shown in Fig. 5.1 (a). The spatial sampling implemented by the electrode array is modeled by a sampling operator  $S_0$ ,

$$S_0(x_c, y_c) = \sum_{m=1}^M \delta(x_c - x_m) \delta(y_c - y_m)$$

where  $\delta(x_c)$  is a Dirac delta impulse. Note that we introduce  $S_0$  to only select (sample) those cells that have an electrode on top. In simple words, to move from the higher-resolution representation (in terms of the cell locations) to a low-resolution representation (in terms of the electrode locations). The measurement model in Eq. (5.3) can thus be written as

$$\phi(x_c, y_c, t_c) = \frac{1}{4\pi\sigma_e} S_0(x_c, y_c) (R_0(x_c, y_c) \ast\ast I(x_c, y_c, t_c)), \quad (5.5)$$

where  $\ast\ast$  denotes the 2D spatial convolution. Note that we have assumed the electrode diameter can be neglected in the model for  $R_0$ . We will motivate this assumption in Section 5.3.6.

To be able to invert the model, we discretize Eq. (5.5) in space as well as in time. In space, we use source clamping and replace each block of cells in the three dimensional tissue with a modeled “cell” on a uniform 2D grid of cells with cell-to-cell distance  $\Delta x$  and  $N = r_c \times c_c$  the total number of cells. symbols  $r_c$  and  $c_c$  are the number of rows and columns of the grid, respectively. We also sample in time with sample period  $T_s$  and total number of time-domain samples  $T$ . The discretized convolutive model of the electrogram then becomes

$$\phi[x, y, t] = c S_0[x, y] (R_0[x, y] \ast\ast I[x, y, t]), \quad (5.6)$$

where  $x, y, t$  are integers that index the sample grid, and  $c = \Delta x^2 / 4\pi\sigma_e$  contains all constants and will be omitted for simplification. The sampled distance kernel  $R_0[x, y]$  is represented by a limited support of size  $(2b+1) \times (2b+1)$  elements. To implement the convolution, the modeled 2D grid of cells need to be extended by  $b$  cells in each direction. The sampling operator  $S_0[x, y]$  selects only the  $M$  spatial locations on the grid on which we have measurements, and replaces the other locations with zero. This discretized model is easily translated into a matrix model [57].

### 5.2.3. TRANSMEMBRANE CURRENT ESTIMATION

Our aim, in this section, is to estimate the transmembrane currents  $I[x, y, t]$  in Eq. (6.4), which is both a deconvolution and an interpolation problem. Basically, the deconvolution can be performed by using a loss function that minimizes the least square error between the target value  $\phi$  and the estimated value  $S_0(R_0 \ast\ast I)$  (first term in Eq. (5.7), below). However, since the number of available electrograms is less than the number of modeled cells and the distance kernel has a low-pass filtering effect, the inverse problem is highly ill-posed and

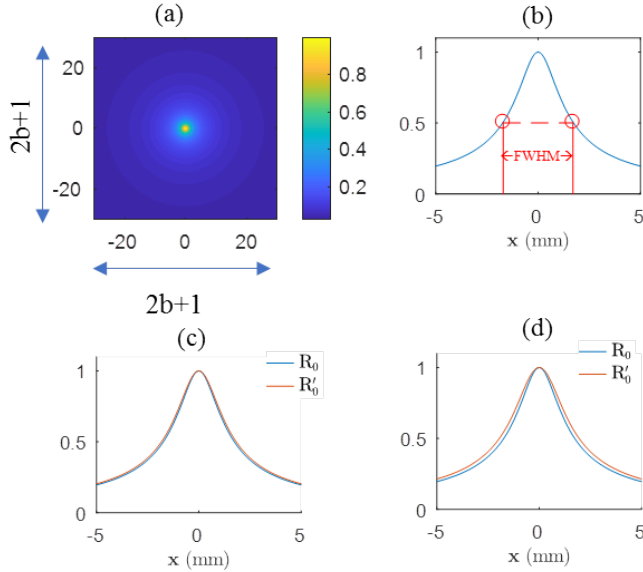


Figure 5.1: (a) The distance kernel calculated from Eq. (5.4) with  $z_0 = 1$  mm and (b) a cross section of the distance kernel at the central row with its FWHM denoted by vertical red lines. (c and d) The cross section of the distance kernel at the central row for  $(R_0)$  and  $(R'_0)$ , without and with considering the effect of the electrode diameter, respectively. The electrode diameter equals  $d_0 = 0.45$ mm and  $d_0 = 1$ mm in (c) and (d), respectively.

results in unstable solutions. To stabilize the solution, we need to introduce regularization constraints that rule out physically unlikely solutions by employing prior knowledge of the expected solution.

A classical regularization technique in this context is Tikhonov regularization [61], however, it provides only a spatial constraint, and the underlying assumptions on the prior are not strong enough to provide for much interpolation. A priori space-time information such as a specific wave pattern propagation is too specific and does not hold if the EGMs are fractionated. On the other hand, a priori information should be simple enough to allow an efficient problem solving. As shown in many studies, the sharp deflections in an electrogram are of high importance in the analysis of wave propagation and AF. These deflections are visible in the first-order time derivative of the transmembrane current, denoted by  $I'[x, y, t]$ . A prior model is that the temporal derivative should have only a few nonzero elements, which are its fast temporal deflections. Note that the assumption may not hold for electrograms recorded at areas with continuous electrical activity and no distinct deflection (e.g., CFAEs). However, in most types of fractionated electrograms, specially those due to far-field atrial activities, lines of blocks and wave collisions, the number of deflections is still small and the first-order time derivative of the transmembrane current can be considered sparse. In an optimization framework, this is implemented by imposing an  $\ell_1$ -norm constraint as the regularization function (the second term in Eq. (5.7), below). The  $\ell_1$ -norm which is the sum of absolute values, is known to induce sparsity in the solution.

The resulting regularized optimization problem that we propose is thus given by

$$\min_I \quad \|\phi - S_0(R_0 \circledast I)\|_2^2 + \lambda \|I'\|_1 \quad (5.7)$$

where

$$\|I\|_2^2 := \sum_x \sum_y \sum_t |I[x, y, t]|^2, \quad \|I'\|_1 := \sum_x \sum_y \sum_t |I'[x, y, t]|$$

and  $\lambda$  is a regularization parameter that is a weight on the importance of the regularization, which will be discussed further in Section 5.3.7.

Due to the coupling between the  $\ell_1$ -norm and the  $\ell_2$ -norm terms, Eq. (5.7) is a hard problem to solve. An efficient numerical approach to solve  $\ell_1$ -regularized problems is the Split Bregman algorithm [51] which splits the  $\ell_1$ -norm and  $\ell_2$ -norm components by introducing new variables. To efficiently employ the Split Bregman algorithm on this problem, we propose to use two new splitting variables,  $Z_1 = R_0 \circledast I$  and  $Z_2 = I'$ . The new optimization problem will then be

$$\begin{aligned} \min_{I, Z_1, Z_2, B_1, B_2} \quad & \|\phi - S_0 Z_1\|_2^2 + \mu_1 \|Z_1 - (R_0 \circledast I) - B_1\|_2^2 \\ & + \lambda \|Z_2\|_1 + \mu_2 \|Z_2 - I' - B_2\|_2^2 \end{aligned} \quad (5.8)$$

where  $B_1$  and  $B_2$  are the Bregman iterative parameters and  $\mu_1$  and  $\mu_2$  are the penalty parameters. Due to the decoupling, we can now break the problem in Eq. (5.8) into five easy steps. Each step updates the value of one of the unknown parameters  $I, Z_1, Z_2, B_1$ , and  $B_2$ . A proper representation of Eq. (5.8) for structured matrix computations and a detailed description of the five steps taken to solve it, can be found in our previous work in [62], where in a preliminary study, we focused on the proper formulation of the present problem and the derivation of efficient solutions for its steps. In total, the algorithm has a fast convergence rate to a reasonable precision in practice by avoiding costly matrix inversion and performing the computations in the Fourier domain.

Note that the modeled cell size  $\Delta x$  that we use in the inverse problem to estimate the transmembrane currents is much larger than a real cell size and, as mentioned before, each modeled cell in our simulation represents a group of cells in the 3D real tissue. Therefore, the estimated transmembrane currents would actually be more localized electrograms than the exact cellular transmembrane currents. However, in this chapter, we will keep referring to them as transmembrane currents.

## 5.3. SIMULATION RESULTS

### 5.3.1. STRATEGIES FOR GENERATION OF FRACTIONATED ELECTROGRAMS

To perform an instrumental evaluation of our proposed approach, we need to generate simulated fractionated electrograms. We use various patterns of heterogeneity for the tissue conductivity map, based on the literature, to produce fractionation. This assures that the patterns are sufficient to obtain fractionation and the resulting electrograms are representative of real clinical data. The size of each map is  $101 \times 83$  cells, with  $\Delta x = 0.6$  mm. The simulated patterns, in order of increasing level of heterogeneity, are:

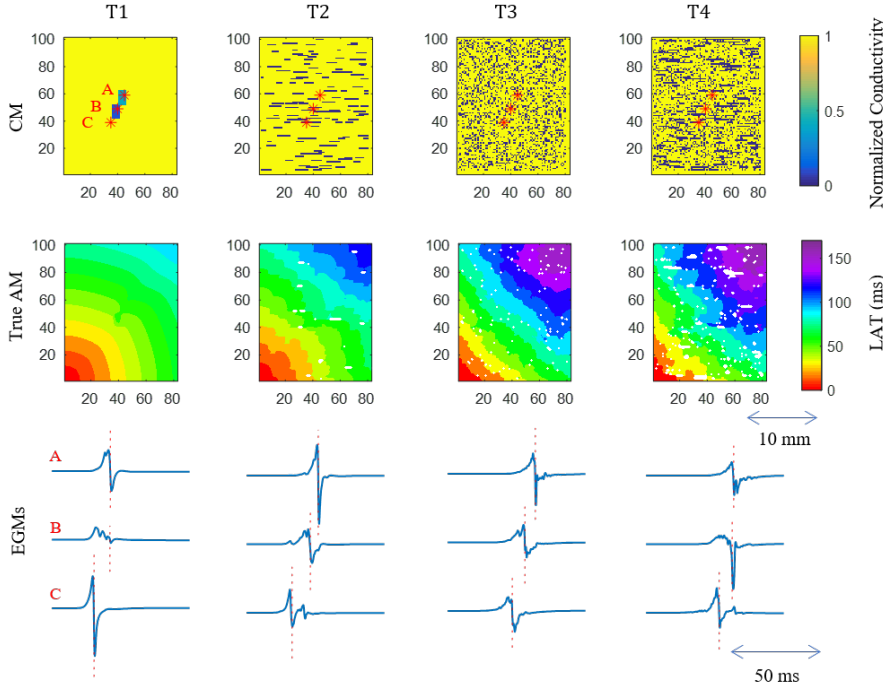


Figure 5.2: The first row of the image shows four normalized conductivity maps (CM) denoted by T1 to T4. The second row shows the corresponding true activation maps (AM) and the third row shows three example electrograms recorded by electrodes at locations A, B, and C denoted by the red \*. The true LAT of each electrogram is denoted by vertical red dashed lines.

1. *A small conduction block:* A homogeneous tissue except for two small areas with smaller conduction in the center (see T1 in Fig. 5.2). Notice that T1 is not representative of real tissue, but serves as a simple example for visualization purposes.
2. *Zones of no conduction:* In this model the heterogeneities in conductivity are incorporated as a set of randomly positioned lines of blocks, disconnecting the coupling between the cells on the grid [63] (see T2 in Fig. 5.2).
3. *Percolation:* the conduction disturbance in this approach is modeled by randomly disconnecting the coupling between some modeled cells and their neighbors [64] (see T3 in Fig. 5.2).
4. *Zones of no conduction and percolation:* both approaches are used simultaneously to generate new pattern of heterogeneity (see T4 in Fig. 5.2).

To model action potential propagation in the simulated tissues, Eq. (5.1) is discretized and solved using a finite difference method with no flux boundary condition. A more detailed description of the simulation steps and parameters can be found in Chapter 4. The

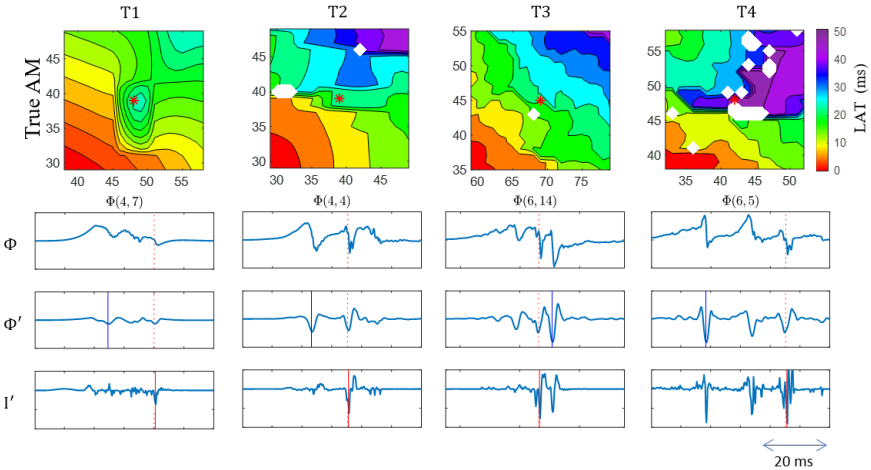


Figure 5.3: The zoomed activation maps around four representative fractionated electrograms selected from T1 to T4 in Fig. 5.2 are shown in the first row. The electrogram location in the center is denoted by red \*. The second row shows the fractionated electrograms. The true LAT of each electrogram is denoted by red vertical dashed line. The third and fourth row show the time derivative of the electrograms, and the time derivative of the estimated transmembrane current with their steepest descent denoted by blue and red vertical lines, respectively.

resulting activation maps are shown in the second row of Fig. 5.2. Each pixel in the activation map represents the true activation time of its corresponding cell which is annotated as the time when the cell potential  $V$  reaches a threshold value of  $-40$  mV in the depolarization phase of its action potential. The white pixels belong to the cells that were positioned on a block and did not get activated. Finally, Eq. (5.3) in the discretized form is used to compute the electrograms recorded by an assumed  $15 \times 9$  electrode array ( $M=135$ ), with an inter-electrode distance of  $\Delta l = 3\Delta x$ , covering the  $43 \times 25$  central cells and a constant value of  $z_0 = 1$  mm (which will be discussed in Section 5.3.4). We used the largest kernel size possible,  $(2b+1) \times (2b+1) = 83 \times 83$  to compute the simulated electrograms. The last row of Fig. 5.2 shows the simulated electrograms recorded at three locations on the tissue denoted by the \*. The true LAT of each electrogram which equals the activation time of the cell that is exactly under the electrode, is also denoted by red vertical dashed lines. Due to the heterogeneity in the tissues, the recorded electrograms have multiple deflections. Moreover, as we move from T1 to T4, the level of fractionation increases and the deflections get less distinct.

### 5.3.2. TRANSMEMBRANE CURRENTS

To visualize the performance of our proposed approach, we start with examples of single electrograms. Fig. 5.3 shows four examples of fractionated electrograms selected from T1 to T4, respectively. As can be seen in the zoomed activation maps of the  $21 \times 21$  cells surrounding the fractionated electrogram, the slow conductions and blocks in the wave propagation induce fractionation in the recorded electrogram. The first-order time derivatives of the electrograms are plotted in the second row. As can be seen, the local deflection

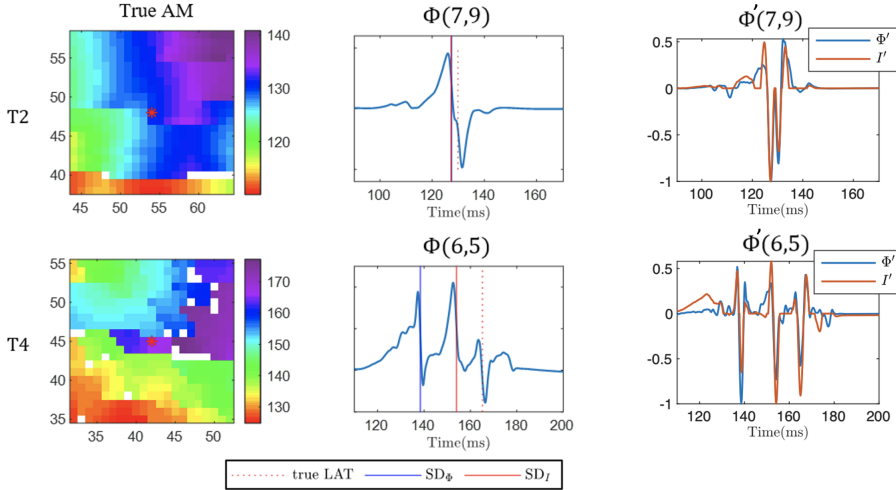


Figure 5.4: Two example electrograms in which both  $\text{SD}_\Phi$  and  $\text{SD}_I$  fail to estimate the true LAT. The first column shows the zoomed activation maps around the selected electrograms from T2 and T4. The second column shows the electrograms with the true and estimated LAT using both approaches. The third column shows normalized  $\Phi'$  and  $I'$ . You can see how the deflection with the steepest descent changes in the second row.

5

that coincides with the true LAT, is not the steepest descent. These examples show that, although in most studies the steepest descent is used as the LAT, it may not provide reliable results in fractionated electrograms.

We used the  $15 \times 9$  electrogram array and Eq. (5.8) to estimate the transmembrane current  $I[x, y, t]$ . For simplification the limited kernel size of  $(2b+1) \times (2b+1) = 13 \times 13$  was used in the inverse problem. Since the focus of this study is on introducing the approach itself and not on optimal tuning of its parameters, we used values that yielded good results in LAT estimation in all simulations, which are,  $\lambda = 7 \times 10^{-4}$ ,  $\mu_1 = 1$ ,  $\mu_2 = 1$ , and the number of iteration  $N_{\text{itr}} = 100$ .

The first-order time derivative of the estimated transmembrane currents are plotted in the third row of Fig. 5.3. As can be seen, the local deflections are amplified and the far-field activities are attenuated. Now as expected, the steepest descent of the transmembrane currents coincides with the true LAT. Fig. 5.4 also shows two examples where both methods fail to estimate the correct LAT. This highly depends on the wave propagation pattern but mostly happens around areas with a complex propagation pattern, with a strong far-field activity that is rather close to the electrode location.

As can be seen, the estimated transmembrane currents do not look as sharp as expected and still some level of fractionation is observed. This is because the estimation of the transmembrane current in the inverse problem is highly ill-posed and there is no guarantee that the resulting electrograms should look like as expected specially in case of fractionation. This can be imposed on the problem by using different regularizations such as imposing sparsity constraint on the transmembrane current itself to provide sharper results or minimizing the error between the estimated currents and a stereotype transmembrane

current. However, our goal in this chapter is to improve LAT estimation, and our experiments with different regularization terms shows that the current problem formulation in Eq. (5.7) provides the best results. That is because imposing the sparsity constraint on the first time-derivative of the transmembrane current helps to preserve the sharp deflections of the transmembrane current (that are later annotated as LATs) while performing deconvolution.

### 5.3.3. LAT ESTIMATION

Since the transmembrane currents are less affected by the far-field activities, they should provide a better estimation of LATs than the electrograms. To evaluate the performance of our proposed approach ( $SD_I$ ) in LAT estimation, we have compared its results with two reference approaches: (i) steepest descent of the electrograms, and ( $SD_\phi$ ) (ii) maximum of the spatial gradient of the electrogram array ( $SG_\phi$ ) [65]. From each of the three conductivity patterns demonstrated as T2, T3 and T4 in Fig. 5.2, 5 randomly generated tissues were simulated. This resulted in 675 simulated electrograms for each pattern. The proposed and the two reference methods were used to estimate the LATs in each electrogram.

In the estimation of the error, electrograms that were positioned on the cells that did not get activated were excluded. This resulted in 658, 650, and 649 simulated electrograms in tissue type T2, T3 and T4, respectively. The resulting root-mean-square errors (RMSE) between the true LAT and the LAT estimated by each approach per tissue type are shown in Table 5.1. On average, in all tissue types, the proposed approach outperforms the reference approaches in LAT estimation.

Table 5.1: RMSE (ms) in LATs estimation of the simulated electrograms using the proposed approach  $SD_I$ , the steepest descent  $SD_\phi$ , and the maximum spatial gradient  $SG_\phi$ .

	T2	T3	T4
$SD_I$	2.5	2.4	1.8
$SD_\phi$	3.1	4.2	2.2
$SG_\phi$	4.7	7.0	3.0

For a better comparison, Fig. 5.5 shows the histogram of the absolute errors (larger than 2 ms) in LAT estimation by  $SD_\phi$  and  $SD_I$ . As can be seen, the number of errors with large values are much larger with  $SD_\phi$  than with  $SD_I$ . Since these large errors belong to areas with blocks in the tissue, this shows that a large number of the blocks and heterogeneities are ignored by  $SD_\phi$ .

As an example, Fig. 5.6 demonstrates the true activation map of the  $15 \times 9$  electrogram array recorded on T1, as well as the three estimated activation maps using  $SD_I$ ,  $SD_\phi$ , and  $SG_\phi$ . As can be seen, there is an area with slower conduction in the center of the tissue which causes fractionation in the resulting electrograms. Since this area is small and has a low conductivity, its local deflections are smaller than the nonlocal deflections caused by far-field activities of the neighboring cell. As a result,  $SD_\phi$  and  $SG_\phi$  both miss the local deflections, and annotate the far-field activities as the LAT. On the other hand, the proposed approach first amplifies the local activities and then annotates them as the LAT, which helps

to preserve the block in the center.

Fig. 5.7 also provides another example of a simulated tissue with two extensive lines of block that can potentially lead to a reentry circuit (denoted by the white arrows) in larger scales. The white rectangle in the middle of the tissue denotes the location of the  $15 \times 9$  electrode array. The activation maps estimated using the steepest descent  $SD_\phi$  and our proposed approach  $SD_I$  of the simulated electrograms are also shown. As can be seen, no evidence of the block lines is visible in the  $SD_\phi$ . This is because the local deflection cased by the wave propagating in between the two lines is very small compared to the strong activity of the neighboring cells. On the other hand, our proposed approach  $SD_I$  accurately annotates the small local deflections except for the two electrodes at the boundaries due to the incomplete observations in their neighborhoods.

### 5.3.4. ELECTRODE HEIGHT $Z_0$

Throughout this chapter, we used a constant value  $z_0=1$  mm for the electrode height, as suggested in [66, 67]. In this section, we aim to examine if this value is applicable in our simulation setup and how it affects the simulated electrograms. To do so, we have designed an experiment as follows: (i) first, an  $8 \times 8$  subsection of the clinical electrogram array with equal number of rows and columns is selected. To avoid further complications, a subsection of the array with non-fractionated electrograms is selected. (ii) The activation map of the selected subsection is estimated and interpolated (using cubic interpolation). The resolution is increased by 3 times in both the  $x$  and the  $y$  direction. The higher resolution activation map is used as the activation map of the modeled cells whose sizes are one-third of the inter-electrode distance. (iii) To regenerate electrograms based on the higher resolution activation map, the simplified electrogram model in Chapter 4 is used. It employs the simplifying assumption that once activated, all cells produce the same stereotype action potential  $V_0(t)$ . The stereotype  $V_0(t)$  is estimated from the Courtemanche model for a single cell. The action potential produced by each modeled cell will therefore be  $V_n(t) = V_0(t - \tau_n)$ , where  $\tau_n$  is the activation time of the cell. (iv) The transmembrane currents are then calculated using

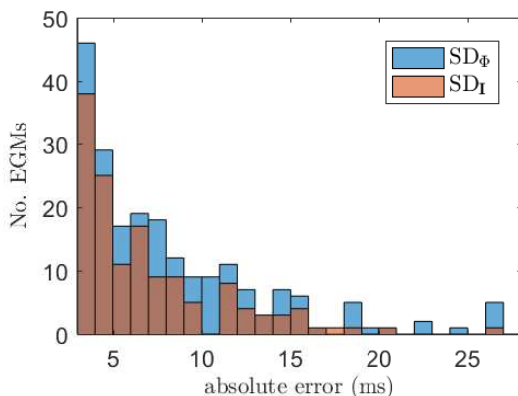


Figure 5.5: The histogram of absolute errors (larger than 2 ms) in LAT estimation using  $SD_\phi$  and  $SD_I$  on simulated electrograms.

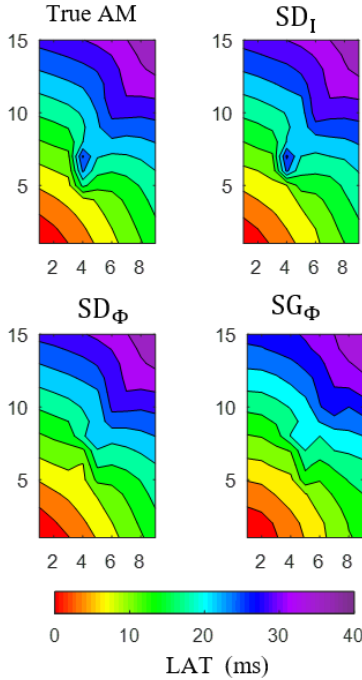


Figure 5.6: The true (simulated) activation map of the  $15 \times 9$  electrogram array in T1, as well as the estimated activation maps using the proposed approach  $SD_I$ , the steepest descent  $SD_\Phi$ , and the maximum spatial gradient  $SG_\Phi$ , respectively.

$I(x, y, t) = S_v^{-1} \sigma \nabla \cdot \nabla V(x, y, t)$ , assuming the conductivity is the same in the recording area as the propagation is also homogenous. We further normalize the amplitudes of regenerated and clinical electrograms and ignore all the constants. (v) Finally, Eq. (5.3) is used to calculate the regenerated electrograms from the transmembrane currents. Since the LATs and other parameters are estimated from the clinical electrograms, the only left parameter that can affect the morphology of the regenerated electrograms is  $z_0$ .

As an example, Fig. 5.8 (a) shows the high resolution activation map estimated from the selected  $8 \times 8$  subsection of a clinical electrogram array. Fig. 5.8 (b, c and d) show a clinical electrogram as well as its corresponding regenerated electrograms (using the above approach) with three different values of electrode height:  $z_0 = 1$  mm,  $z_0 = 0.2$  mm, and  $z_0 = 5$  mm, respectively. The electrogram location is denoted by the red \* on the activation map. As can be seen, the effect of  $z_0$  is more evident on the steepness of the main deflection and the regenerated electrogram with  $z_0 = 1$  mm has the best match to the clinical electrogram. Although an extension of the above approach can be used for the systematic estimation of  $z_0$ , the accuracy of the result will largely depend on the accurate estimation of other underlying parameters including activation map, conductivity map and the stereotype  $V_0$ . This makes the correct estimation of  $z_0$  in a clinical setup prone to error and almost impractical.

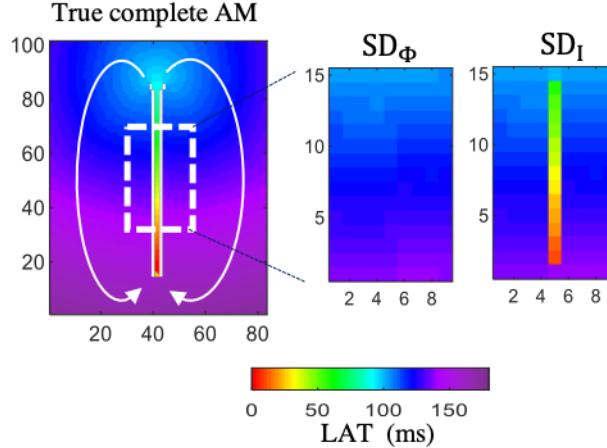


Figure 5.7: Simulated tissue with two parallel vertical lines of block close to the center of the tissue that can potentially lead to a reentry circuit (denoted by white arrows). The white rectangle in the middle of the tissue denotes the location of the  $15 \times 9$  electrode array. The activation maps estimated using the steepest descent  $SD_{\Phi}$  and our proposed approach  $SD_I$  are also shown.

5

Fig. 5.9 shows two examples of using wrong values for  $z_0$  in our proposed inverse problem for estimating LATs for T1 in Fig. 5.6. The values used in the inverse problem are  $z_0 = 0.5$  mm,  $z_0 = 1$  mm, and  $z_0 = 2$  mm, while the true value used in the forward model for generating the electrograms is  $z_0 = 1$  mm. As can be seen, using smaller values for  $z_0$ , to some extent, will still provide better results than  $SD_{\Phi}$ . This is because the distance kernel has a larger value on its central element and using it in the inverse problem will sharpen the electrograms.

### 5.3.5. SPATIAL SAMPLING RESOLUTION

The required inter-electrode distance for spatial sampling of the tissue using the electrode array depends on the spatial bandwidth (Nyquist rate) of the electrograms. Although the true spatial bandwidth of the underlying electrogram is at the micrometer level and unknown, it is unavoidably filtered by the response of the measurement electrodes. In other words, the blurring caused by the distance kernel  $R_0$  limits the spatial resolution of the recorded electrical activity. The distance kernel (also known as point spread function (PSF) in the image processing literature [68, 69]) performs as a low-pass filter and inevitably removes the high-frequency components of the recorded signal.

The so-called “Full Width at Half Maximum (FWHM)” of the distance kernel is commonly used as a short-hand measure of the required spatial resolution [69]. It is equal to the width between the two points on the distance kernel where the amplitude has dropped to half of its maximum value. Fig. 5.1 (a) shows the symmetric 2D distance kernel of size  $60 \times 60$  mm<sup>2</sup>, calculated using Eq. (5.4) with  $z_0 = 1$  mm and with ignoring the electrode diameter. The distance kernel is normalized to have a maximum of 1. Fig. 5.1 (b) shows a cross section of the distance kernel at the central row where the FWHM is also denoted.

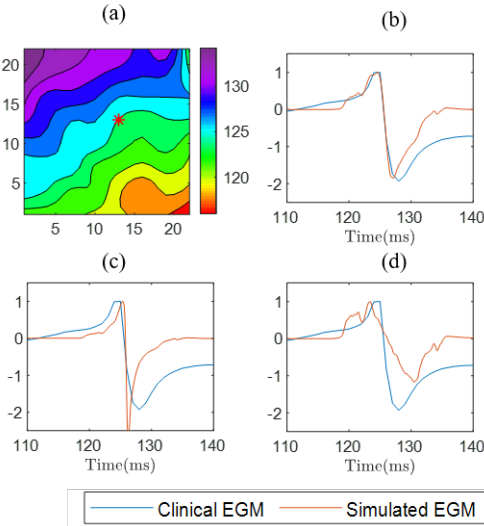


Figure 5.8: (a) The high resolution activation map estimated from an  $8 \times 8$  subsection of a clinical electrogram array. (b,c and d) The clinical and regenerated electrogram of the electrode at the location denoted by \* with  $z_0=1 \text{ mm}$ ,  $z_0=0.2 \text{ mm}$  and  $z_0=5 \text{ mm}$ , respectively.

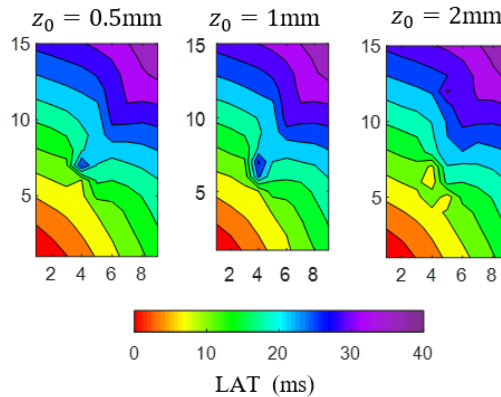


Figure 5.9: Three different values of  $z_0 = 0.5 \text{ mm}$ ,  $z_0 = 1 \text{ mm}$ , and  $z_0 = 2 \text{ mm}$  are used in the inverse problem to estimate LATs for T1 in Fig. 5.6. The true value used in the forward model for generating the electrograms is  $z_0 = 1 \text{ mm}$ .

For this kernel the FWHM, and therefore the maximal spatial sampling distance, equals 3.4 mm. Although sampling at Nyquist rate guarantees perfect reconstruction of the sampled signal, a more conservative approach would be to record the electrograms at smaller distances than the FWHM. Therefore, the spatial resolution we use in our clinical setup equals 2 mm. Note that a denser electrode array will only improve the signal-to-noise ratio but will not reduce the blurring caused by the distance kernel. Also note that the estimated maximal spatial sampling distance is strongly dependent on the selected electrode height  $z_0$ .

### 5.3.6. ELECTRODE SIZE

The distance kernel, and therefore the measured electrograms, also depend on the diameter  $d_0$  of the electrodes. In this section, we investigate the effect of the electrode's diameter  $d_0$  on the measurement model. We describe the effect of the non-zero diameter by an averaging of all cellular electrograms that the electrode surface covers. This can be modeled by updating the distance kernel in Eq. (5.4) as

$$R'_0(x, y) = D(x, y) \ast R_0(x, y), \quad (5.9)$$

where function  $D(x, y)$  is 1 if  $\sqrt{x^2 + y^2} < d_0/2$ , and 0 otherwise. The convolution results in an averaging effect over the electrode surface.

Fig. 5.1 (c and d) shows the distance kernel after considering the electrode diameter, calculated using Eq. (5.9). In Fig. 5.1 (c) the electrode diameter is  $d_0 = 0.45$  mm. This is equal to the electrode size we use for recording our clinical data. Fig. 5.1 (d) also shows the PSF for  $d_0 = 1$  mm. As can be seen, the electrode size does not change the morphology of the distance kernel considerably and its effect will be ignored in this study. This is because of the large value of  $z_0$  which is inherent to the tissue and cannot be improved. This result also implies that decreasing the electrode diameter to smaller values than we currently use will not considerably improve the resolution of the electrogram recording.

### 5.3.7. REGULARIZATION PARAMETER $\lambda$

As discussed in Section 5.2.3, the inverse problem of transmembrane current estimation is highly ill-posed and may result in many unfavorable solutions. To overcome this issue, we added a regularization term to the optimization problem in Eq. (5.7). Although many regularization terms can be used to stabilize the results, we opt for the sparsity of the first-order time derivative of the transmembrane current. This helps to preserve the sharp deflections of the transmembrane current (that are later annotated as LATs) while performing deconvolution. However, one can, depending on the application, employ different regularizations such as imposing a sparsity constraint on the transmembrane current to provide sharper results, or minimizing the error between the estimated currents and a stereotype transmembrane current.

The regularization parameter  $\lambda$  controls the importance of the regularization term. Fig. 5.10 shows the logarithm of the RMSE in LAT estimation using  $SD_\phi$  and  $SD_I$  with different values of  $\lambda$  for the five randomly generated tissues based on the T4 pattern in Fig. 5.2. Although using larger value for  $\lambda$  makes the resulting transmembrane current sharper, as can be seen, it increases the error in LAT estimation drastically. This is because the deconvolution error is ignored. On the other hand, decreasing the value of  $\lambda$  after a certain point causes almost no regularization and the error will stay constant.

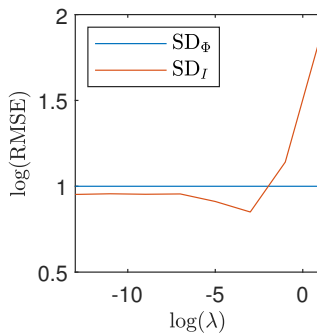


Figure 5.10: The logarithm of RMSE in LAT estimation using  $SD_\Phi$  and  $SD_I$  with different values of  $\lambda$  for the five randomly generated tissue based on the T4 pattern as in Section 5.3.1. The logarithm of the RMSE is normalized so that the steepest descent has an amplitude of 1.

## 5.4. CLINICAL RESULTS

5

In this section, we applied the proposed method to clinically recorded data. The epicardial electrograms used on this study were recorded using an  $8 \times 24$  unipolar electrode array ( $M = 192$ ) with a 2 mm inter-electrode distance and  $d_0 = 0.45$  mm electrode diameter. The electrode array were subsequently positioned visually by the surgeon on 9 mapping atrial sites using anatomical borders. The array records 5 seconds of sinus rhythm and 10 seconds of induced atrial fibrillation (IAF) signals at each site. This technique was performed in more than 400 patients of 18 years and older, with coronary and/or structural heart disease, with paroxysmal AF, electively scheduled for cardiac surgery and a ventricular ejection fraction above 40%. The acquired signals were amplified, filtered (bandwidth 0.5 to 400 Hz), sampled (1 kHz), analogue-to-digital converted (16 bits) and recorded on a hard disk. More details on the mapping approach and the electrode array specifications can be found in [5].

As with the simulated data, we used the steepest descent of the clinical electrograms ( $SD_\Phi$ ) as well as the steepest descent of estimated transmembrane currents ( $SD_I$ ) to estimate the activation map of the electrogram array. However, we did not have access to the true LATs to evaluate and compare the performance of these two approaches. For this reason, we manually inspected the electrogram array to explain the differences in the resulting activation maps and to identify the local deflections for the clinical examples shown in this section. Although this is a quite complicated task, some spatio-temporal criteria of the electrogram array can help us. The common criteria of nonlocal activities are: (i) having no evidence of propagation [70], (ii) having time-equivalent deflections with lower amplitudes at neighboring electrodes whose amplitudes decrease with distance [71], and (iii) matching highly with the average of the neighboring electrograms [70]. While none of these criteria alone can perfectly single out the local deflection, observing some of these criteria together increases the probability of a correct annotation.

In the following subsections, we provide four categories of common cases where our proposed approach provides different results compared to the steepest descent. In each case, we use one representative example (recorded from different patients) to visualize and discuss the results. Notice that these results are based on our visual observation on a limited

number of patients and a more robust validation on a larger number of patients is deferred to future work. The clinically recorded electrograms for one array ( $8 \times 24$  electrodes) and Eq. (5.8) are used to estimate the transmembrane currents  $I[x, y, t]$  and subsequently the local deflection. It takes about 1.4 seconds to solve the deconvolution problem (with 100 iterations) for the clinical data of size  $M = 24 * 8$  and a single atrial beat (100 ms), without increasing the resolution, and about 6.7 seconds if we increase the resolution by 9 times to have smaller modeled cells (3 times increase in each axis) on a 2.9 GHz Intel i5 MacBook Pro and MATLAB R2019a.

### 5.4.1. TURNING A SMOOTH PROPAGATION INTO A NON-SMOOTH PROPAGATION

The most noticeable difference between the activation maps (AMs) generated from the electrograms  $SD_\phi$  and our proposed approach using the estimated transmembrane currents  $SD_I$  is that, in general, the AMs estimated from electrograms tend to be smoother. An example of such a case is shown as P1 in Fig. 5.11. As can be seen,  $SD_I$  introduces some heterogeneities in the area denoted by a red circle in the map, while the  $SD_\phi$  shows a homogeneous propagation. To investigate the results, we have plotted a  $3 \times 3$  subsection of the electrograms recorded in the area of interest. The electrode locations are denoted by white dots on the AMs. The blue vertical lines denote the LAT estimated using  $SD_\phi$  and the red vertical lines denote the LAT estimated estimated using  $SD_I$ . As can be seen, the recorded electrograms are fractionated, which is an indication of a zone of slow conduction in the tissue [72]. This observation matches with the AM we get using  $SD_I$ , but not with the AM we get using  $SD_\phi$ . This is similar to the example already shown in Fig. 5.6.

5

### 5.4.2. CHANGING THE LOCATION OF THE LINE OF COLLISION OR (FUNCTIONAL) CONDUCTION BLOCK

Another noticeable difference between the AM generated by  $SD_\phi$  and  $SD_I$ , is in the location of the line of collision or the line of (functional) conduction block. As can be seen in P2 in Fig. 5.11, a distinct late wavefront (color coded by purple) invades the mapping area from above. The AM estimated using the  $SD_I$  shows that this wavefront covers more parts of the mapping area compared to the AM estimated from  $SD_\phi$ . It also shows that the two distinct discontinuities in the  $SD_\phi$  map are connected. To investigate the results, we have plotted a  $3 \times 3$  subsection of the electrograms recorded in the area of interest. The electrode locations are denoted by white dots on the AMs. The blue vertical lines denote the LAT estimated using  $SD_\phi$  and the red vertical lines denote the LAT estimated estimated using  $SD_I$ . As expected, the electrograms show double potentials, which is an indicator of a collision or a functional block [72]. We can also explain the low amplitude of the second deflection by the small area its corresponding wavefront covers. On the other hand, the other wavefront (color coded in red, yellow and green) covers a bigger area and produces stronger activities. As a result, the electrodes in this area record a nonlocal activity that is much stronger than its true local activity. Moreover, on the right-hand side of the block, all electrodes have similar LAT and there is no evidence for wavefront propagation. This is an indicator of superposition of far-field activity. However, the local activity seems to be very small such that it cannot even be detected using estimated transmembrane currents.

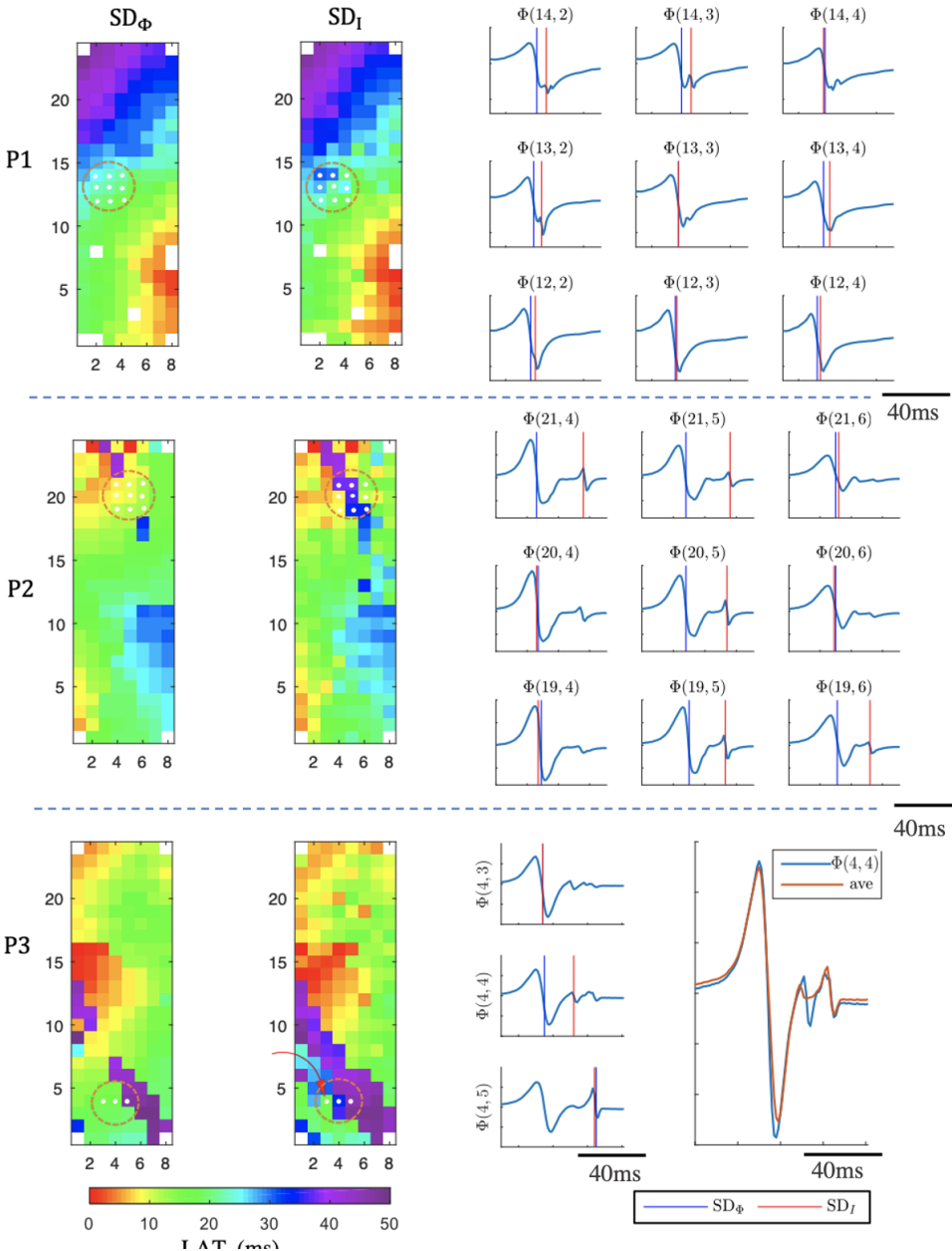


Figure 5.11: Each row of the figure shows a different clinically recorded electrogram array denoted by P1 to P3. The first column shows the LATs estimated from the electrograms  $SD_{\Phi}$  and the second column shows the LATs estimated from the estimated transmembrane currents  $SD_I$ . In each case some representative electrograms belonging to the locations denoted by red dashed circles and white dots are shown at the right hand side of the figure. The blue vertical lines denote the LAT estimated using  $SD_{\Phi}$  and the red vertical lines denote the LAT estimated using  $SD_I$ . The red arrow in P3 shows a new distinct wavefront in the activation map that is only visible in the activation map estimated using  $SD_I$ . The plot at the right-hand side of P3 shows the electrogram  $\Phi(4, 4)$  and the average electrogram of its 8 neighboring electrodes.

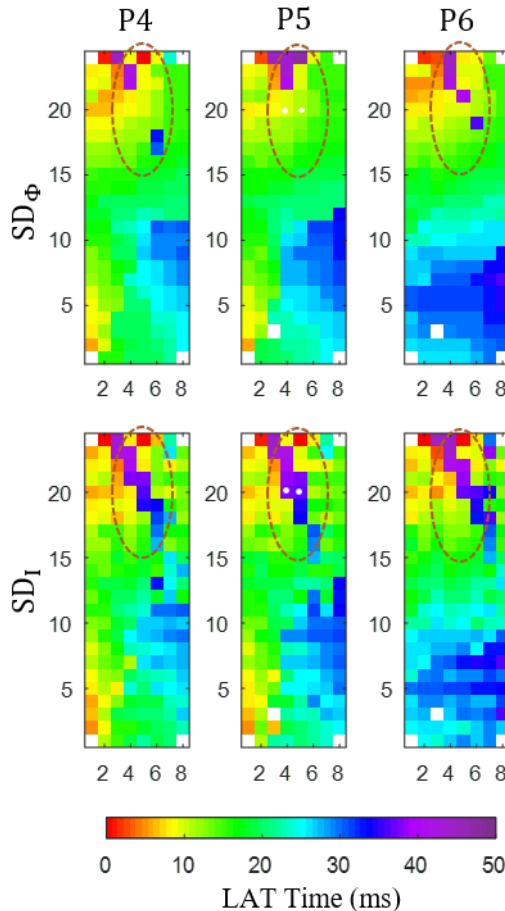


Figure 5.12: The estimated activation maps of three succeeding atrial beats at the same location. The first row shows the activation map estimated using  $SD_{\phi}$  and the second row shows the activation map estimated from  $SD_I$ .

### 5.4.3. INTRODUCTION OF MORE DISTINCT WAVEFRONTS IN THE MAPPING AREA

In some cases, the proposed approach introduces new wavefronts in the mapping area. P3 in Fig. 5.11 shows an example where the estimated activation map using  $SD_{\phi}$  contains two main distinct wavefronts, while the activation map estimated using  $SD_I$  contains a new wavefront color coded by blue and denoted by a red arrow. We have also plotted three electrograms whose locations are denoted by white dots on the activation map. As can be seen, each electrogram belongs to one of the observed wavefronts.  $SD_{\phi}$  and  $SD_I$  provide a similar result in LAT estimation for  $\Phi(4,3)$  and  $\Phi(4,5)$ , while they annotate two different deflections for  $\Phi(4,4)$ . As can be seen,  $\Phi(4,4)$  is composed of 3 main deflections, two of which coincide with its two neighbors, which implies these are the nonlocal activities. However,

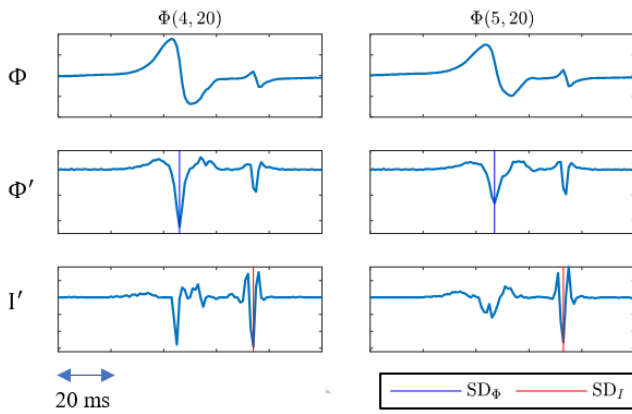


Figure 5.13: Two example electrograms from the block line in P5, the electrode locations are denoted by white dots in the activation map. The second and the third row show the first-order time derivatives of the electrogram and the estimated transmembrane current. The steepest point of each derivative (LAT) is denoted by vertical lines.

5

the second deflection does not match with the two wavefronts in its neighborhood. This indicates that the second deflection belongs to the local activity. This conclusion is more clear when we compare  $\Phi(4, 4)$  with the average activity of its 8 neighboring electrodes shown in the right-hand side of P3 in Fig. 5.11. As can be seen, the difference is more distinct around the second deflection.

#### 5.4.4. PROVIDING MORE CONSISTENT MAPS OVER SUCCEEDING BEATS

One remarkable difference between an AM generated by  $SD_\Phi$  and  $SD_I$  is that the proposed approach provides more consistent activation maps over succeeding atrial beats. Fig. 5.12 shows the activation maps generated by both approaches for three succeeding atrial beats for the same location. As can be seen, both approaches show some large conduction delays in the area denoted by the red oval. However, the pattern is more consistent in the maps estimated using the proposed approach (second row). Note that P4 (in Fig. 5.12) and P2 (in Fig. 5.11) are similar. In Section 5.4.3 we provided some evidence to explain the difference between the activation patterns generated by  $SD_\Phi$  and  $SD_I$ .

Fig. 5.13 also demonstrates two example electrograms denoted by white dots in the line of block of P5. The first-order time derivative of the electrograms and of the estimated transmembrane currents are also plotted. As can be seen in both cases, the amplitude of the smaller deflection increases after the deconvolution. This indicates that this small activation is a local activity and not the far-field effect of the neighboring cells.

## 5.5. DISCUSSION AND CONCLUSION

### 5.5.1. SUMMARY

In this chapter, we proposed a new approach for a better estimation of local activation times for atrial mapping by reducing the spatial blurring effect that is inherent to electrogram recordings, using sparsity based regularization and first-order

time derivatives in formulating the deconvolution problem, improved the performance of transmembrane current estimation. We solved the regularized deconvolution problem efficiently using the Split Bregman algorithm. We also discussed, in summary, the required electrode array specifications including the electrode height, the electrode size and the required spatial resolution for an appropriate deconvolution. Unlike other approaches, our algorithm uses electrophysiological models to incorporates spatial information to improve LATs. We also showed, using realistic simulated tissue, that our algorithm outperforms two reference approaches: steepest descent ( $SD_\phi$ ) as the most common approach for LAT annotation, and the approach based on the spatial gradient ( $SG_\phi$ ) which also requires multi-electrode recording. Our results on simulated and clinically recorded data, show that  $SD_\phi$  is prone to make the activation maps smoother by always selecting the steepest descent and ignoring local small deflections. This arises in situations where the local activities belong to a wavefront that only invades a small part of the mapping area. The activities generated by this wavefront are thus smaller in amplitude compared to the nonlocal activities that belong to a wavefront that covers a larger area. The deconvolution, on the other hand, reduces the effect of nonlocal activities and amplifies the local activities which results in a better estimation of true local deflection. This can result in estimation of AMs that are less smooth and more irregular with probably more distinct wavefronts. It also changes the location of estimated (functional) conduction blocks or collision lines in the tissue.

### 5.5.2. LIMITATIONS OF THE PROPOSED METHOD

In this study, we replaced each block of 3D tissue with a modeled cell in a 2D mono-layer tissue with constant cell-to-cell distance, ignoring the tissue curvature and thickness which might affect the results. Moreover, we assume a constant electrode height of  $z_0 = 1$  mm, to compute the distance kernel while it might be subject to spatial variation and quality of contact. Due to complications of simulating 3D tissue, the performance of the proposed approach was tested on two-dimensional simulated tissue. Since we do not have access to the true local activities of clinically recorded electrograms, we used manual annotation to analyze the performance of the approach.

### 5.5.3. FUTURE WORK

While the focus of this chapter is to develop a new algorithm for a better estimation of LATs in electrogram arrays, future work will include an evaluation on the effect of these improvements on the further analyses performed on LATs regarding AF. More specifically, we aim to investigate the effect of the new approach on the association of conduction disorders with substrates underlying AF and on the performance of existing methods in classification of AF stages in a larger group of patients. Moreover, to provide a more robust claim on the consistency of the estimated activation map over time, we aim to provide a measure of consistency/stability for a larger group of patients.



# 6

## ANALYSING THE EFFECT OF ELECTRODE SIZE ON ELECTROGRAM AND ACTIVATION MAP PROPERTIES

Atrial electrograms recorded from the epicardium provide an important tool for studying the initiation, perpetuation, and treatment of AF. However, the properties of these electrograms depend largely on the properties of the electrode arrays that are used for recording these signals. In this study, we use the electrode transfer function to model and analyze the effect of electrode size on the properties of measured electrograms. To do so, we use both simulated as well as clinical data. To simulate electrogram arrays we use a two-dimensional (2D) electrogram model as well as an action propagation model. For clinical data, however, we first estimate the transmembrane current for a higher resolution 2D modeled cell grid and later use these values to interpolate and model electrograms with different electrode sizes. We simulate electrogram arrays for 2D tissues with 3 different levels of heterogeneity in the conduction and stimulation pattern to model the inhomogeneous wave propagation observed during atrial fibrillation. Four measures are used to characterize the properties of the simulated electrogram arrays of different electrode sizes. The results show that increasing the electrode size increases the error in LAT estimation and decreases the length of conduction block lines. Moreover, visual inspection also shows that the activation maps generated by larger electrodes are more homogeneous with a lower number of observed wavelets. The increase in electrode size also increases the low voltage areas in the tissue while decreasing the slopes and the number of detected deflections. The effect is more pronounced for a tissue with a higher level of heterogeneity in the conduction pattern. Similar conclusions hold

---

This chapter is based on the article "Analyzing the Effect of Electrode Size on Electrogram and Activation Map Properties" by B. Abdi, M.S. van Schie, N.M. de Groot, R.C. Hendriks, in Computers in Biology and Medicine, 2021, p. 104,467.

for the measurements performed on clinical data. The electrode size affects the properties of recorded electrogram arrays which can consequently complicate our understanding of atrial fibrillation. This needs to be considered while performing any analysis on the electrograms or comparing the results of different electrogram arrays.

## 6.1. INTRODUCTION

Recording and processing of electrograms (EGMs) is the cornerstone of mapping procedures guiding ablative therapies of cardiac arrhythmias. Thorough understanding of the impact of recording technology on EGM morphology is of paramount importance, particularly in case of complex tachyarrhythmias such as atrial fibrillation (AF) [11, 73]. However, the properties of these electrograms depend to a large extent on the physical dimensions of the electrode arrays that are used for recording these signals.

As shown in several studies, the electrode size (or diameter) is an important parameter that can affect the characteristics of the recorded electrograms. Most studies focus on bipolar electrograms and measurements that are performed only on clinical recordings [74–78]. There are only a few studies investigating the effect of the electrode size on the properties of the unipolar electrograms using both electrophysiological models and clinical recordings. These properties include signal-to-noise ratio (SNR), fractionation level, voltage level, and the error in local activation time (LAT) estimation [63, 66, 79]. In general, these studies show that increasing the electrode size increases the SNR and consequently the atrial activity is less affected by noise and artifacts [80, 81]. However, this is mainly the case for homogeneous tissue. It has also been shown that the number of deflections and the level of fractionation also increase by increasing the electrode size [63, 78, 79]. Moreover, low voltage areas in the tissue also increase when using bigger electrode sizes [63, 77]. It has also been shown that using larger electrodes, increases the error in LAT estimation [66], which will result in activation maps with less detail and less conduction blocks [74, 76]. These effects are more pronounced in zones of conduction block or slow conduction in the tissue (i.e., scarred tissue) [74, 75].

Some of these studies use clinical recorded electrograms using different electrogram arrays with different electrode sizes that are successively positioned on similar locations on the atria. However, it should be noted that not all observed changes in the electrogram properties are due to changes in electrode size, but also due to the spatio-temporal varying nature of electrical wave propagation (specially during AF) and the changes in the inter-electrode distances. Moreover, bipolar electrograms are also affected by varying propagation directions. In this chapter, we exclusively investigate the effect of the electrode size on the properties of high resolution unipolar electrogram arrays by keeping the other parameters like inter-electrode distances and electrical wave propagation patterns fixed. We use both clinical observation and electrophysiological models that govern the wave propagation and electrogram generation to analyze and investigate these effects. This is done by investigating the electrode transfer function and its properties, making the comparisons and conclusions more robust. Moreover, we investigate these results for tissues with different levels of inhomogeneity in the conductivity map. We also focus on the overall properties of the electrogram array and not only on the per-electrode features. These include the overall error in local activation time estimation, length of slow conduction or block lines, low voltage areas in the tissue, as well as the number of deflections.

We first present the electrogram model, our approach for generating simulated electrograms, and our proposed framework for generating high resolution electrogram arrays with different electrode sizes from clinical electrograms in Section 6.2. We also provide a description of our clinical recording setup and employed measures for characterizing the electrogram array properties in the same section. In Section 6.3 and Section 6.4, we perform our approach on simulated and clinical electrograms, respectively, and present the final results. We also discuss the optimal electrode diameter and appropriate inter-electrode distances for electrode arrays with different electrode sizes, the maximum electrode size for capturing scarred tissue of different sizes, and a proper scaling of the electrogram amplitude for a better comparison of electrograms recorded with different arrays. We discuss our findings and conclude this chapter in Section 6.5.

## 6.2. METHOD

### 6.2.1. ATRIAL TISSUE COMPUTER MODEL

As shown in Section 2.5.2, in our model we consider the atrial tissue as a two dimensional mono-layer grid of cells where the electrode array is positioned at a constant height  $z_0$  above the atrial tissue. We model the electrogram as a weighted summation of transmembrane currents produced by the cells in the tissue in the vicinity of the electrode, where the weights depend on the inverse of the cell-to-electrode distances. An electrogram at location  $(x, y)$  and at time sample  $t$  can then be modeled as [12]

$$\phi(x_m, y_m, t) = \frac{1}{4\pi\sigma_e} \int_{\mathcal{A}} \frac{I_{\text{tr}}(x, y, t)}{\sqrt{(x - x_m)^2 + (y - y_m)^2 + z_0^2}} dA(x, y), \quad (6.1)$$

where  $m = 1, 2, \dots, M$  is the electrode index with  $M$  the total number of electrodes,  $I_{\text{tr}}(x, y, t)$  is the transmembrane current,  $\mathcal{A}$  is the area in which the modeled cells are located,  $A(x, y)$  is the area variable, and  $\sigma_e$  is the constant extra-cellular conductivity. Note that for now we assume that we are recording the electrograms with point electrodes whose diameters can be neglected. We will investigate the effect of electrode diameter later in Section 6.2.2.

The transmembrane current produced by each cell can be computed using the following equation [13]

$$I_{\text{tr}}(x, y, t) = S_v^{-1} \nabla \cdot \Sigma(x, y) \nabla V(x, y, t), \quad (6.2)$$

where  $V(x, y, t)$  is the cellular potential,  $\Sigma(x, y)$  is the intracellular conductivity tensor, and  $S_v = 0.24 \mu\text{m}^{-1}$  is the cellular surface-to-volume ratio. The potential and transmembrane current can simultaneously be calculated using the reaction-diffusion equation that governs the action potential propagation in the tissue [13],

$$C \frac{\partial V(x, y, t)}{\partial t} = I_{\text{tr}}(x, y, t) + I_{\text{st}}(x, y, t) - I_{\text{ion}}(x, y, t, V), \quad (6.3)$$

where  $C = 1 \mu\text{Fcm}^{-2}$  is the total membrane capacitance,  $I_{\text{st}}$  is the stimulus current, and  $I_{\text{ion}}$  is the total ionic current computed according to the Courtemanche model in [33].

### 6.2.2. ELECTRODE'S TRANSFER FUNCTION MODEL

For a uniform grid of cells with  $\Delta x$  denoting the cell-to-cell distance, we can rewrite Eq. (6.1) as a 2D spatial convolution of transmembrane currents with an appropriate electrode transfer function  $R_0(x, y)$  as

$$\phi(x, y, t) = c S_0(x, y)(R_0(x, y) \ast\ast I_{\text{tr}}(x, y, t)), \quad (6.4)$$

where  $\ast\ast$  denotes the 2D spatial convolution, and  $c = \Delta x^2 / 4\pi\sigma_e$  contains all constants and will be omitted for simplification. We introduced in Eq. (6.4) the sampling operator  $S_0(x, y) = \sum_m \delta(x - x_m, y - y_m)$  with Dirac delta functions to select the  $M$  spatial locations on the grid on which we have measurements and replace the other locations with zero. This can also be used to de-select faulty electrodes. The electrode transfer function is

$$R_0(r) = \frac{1}{\sqrt{r^2 + z_0^2}}. \quad (6.5)$$

where  $r = \sqrt{x^2 + y^2}$  is the horizontal distance between the electrode (at origin) and a cell at location  $(x, y)$ . However, an electrode whose diameter is bigger than the modeled cell size (i.e.,  $d_0 > \Delta x$ ) can no longer be considered as a point electrode. The transfer function should therefore take the diameter of the electrode into account as proposed in [63], i.e.,

$$R_{d_0}(r) = 2 \arcsin \frac{d_0}{\sqrt{(r - d_0/2)^2 + z_0^2} + \sqrt{(r + d_0/2)^2 + z_0^2}}. \quad (6.6)$$

The first row of Fig. 6.1 shows the 2D representation of the electrode normalized transfer function of a point electrode from Eq. (6.5) as a function of  $x$  and  $y$ , as well as the normalized transfer function based on  $r$ , both computed by setting  $z_0 = 0.5$  mm. As can be seen, the value of the transfer function, or the weight of the transmembrane current in Eq. (6.4), for the cell that is exactly under the electrode center equals to 1. A large weight indicates more influence on the final recorded electrogram. As we move further from the center, the weights decrease but the values are still noticeable. One important parameter commonly used to characterize the transfer function is the full width at half maximum (FWHM), denoted on the plot. It shows the diameter at which the weight of the cells is greater than half of the maximum value, indicating their significant influence on the final recorded electrogram. A small FWHM (a narrower transfer function) denotes that the electrode records data from a smaller area thus providing more local electrograms. However a large FWHM denotes that the recorded electrogram will be the summation of activities in a larger area. This can severely affect the morphology of the local activities if the propagation is not homogeneous in the electrode neighborhood. In general, summing up activities in a larger area will smooth out the important local details.

The bottom left plot in Fig. 6.1 shows the transfer functions for different electrode diameters  $d_0 \in \{0.5, 2, 4, 8\}$  mm with  $z_0 = 0.5$  mm. The bottom right plot in Fig. 6.1, also shows the transfer functions when  $z_0 = 1$  mm, assuming a thicker tissue. As can be seen in both plots, as the electrode diameter increases, the transfer function gets wider (larger FWHM) indicating that the recorded electrogram will be more influenced by the neighboring activities. The difference in FWHM is more evident in thinner tissues and for smaller diameters. This will be investigated in more detail in Section 6.3.3.

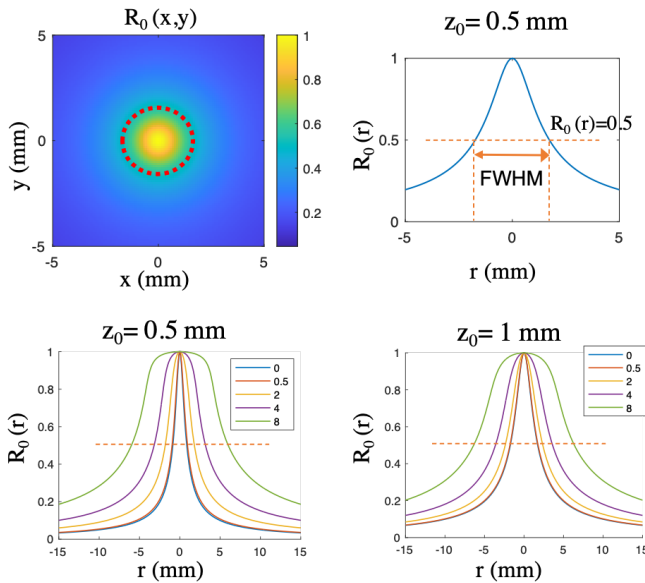


Figure 6.1: Top left: the 2D representation of the electrode normalized transfer function  $R_0(x,y)$  of a point electrode. The red dashed circle represents the FWHM. Top right: the electrode transfer function based on  $R_0(r)$ . Bottom:  $R_{d_0}(r)$  for different electrode diameters  $d_0 \in 0, 0.5, 1, 2, 4, 8$  mm with  $z_0 = 0.5$  mm (left) and  $z_0 = 1$  mm (right).

6

### 6.2.3. MODELING ABNORMAL TISSUE

To generate simulated fractionated electrograms that are representative for clinical data, various approaches have been suggested in the literature. Jacquemet et al. in [63] incorporate the heterogeneities in the conductivity as a set of randomly positioned lines of conduction block that disconnect the coupling between the cells on the grid. However, Vigmond et al. in [64] model the conduction disturbance by randomly disconnecting the coupling between some modeled cells and their neighbors through randomly positioned dots of conduction block. In this chapter, we use both patterns simultaneously for simulated conductivity maps of modeled tissue. This provides simulated electrograms and activation maps that are more similar to clinical recordings (by visual inspection).

To simulate electrograms with different levels of fractionation, we use conductivity maps with varied levels of conduction block density. These are shown in the first row of Fig. 6.2 denoted as T1, T2 and T3 having a low, medium and high density of conduction block, respectively. For comparison, we have also shown the results for a homogeneous tissue with planar wave propagation, denoted by T0, which serves as a standard reference for other tissue types. The size of each tissue is  $213 \times 173$  cells, with a cell-to-cell distance of  $\Delta x = 0.5$  mm. We also activate the tissues using one or two activation waves (by injecting stimulation currents) entering the tissue from different locations to simulate the activation maps during AF (for one atrial beat, lasting around one second).

To model action potential propagation in the simulated tissues, Eq. (6.3) is discretized and solved using a finite difference method with no flux boundary condition. The activities

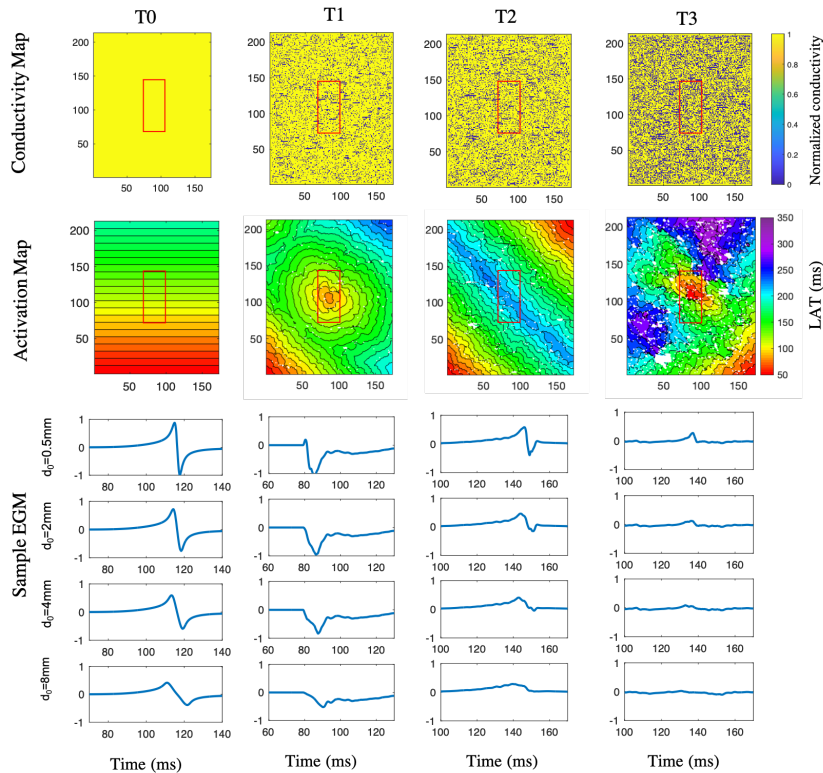


Figure 6.2: Conductivity map, activation map and an example electrogram simulated for different electrode sizes of four simulated tissues. T0 is modeled as a homogeneous tissue while T1, T2 and T3 have a low, medium and high density of conduction block in their conductivity map, respectively. The red rectangle represents the electrode array position. We assume there is one electrode on top of each modeled cell.

are simulated for 1000 ms to include one complete atrial beat, but only a selected time window of 150 ms in length is used for evaluation of electrograms as it includes all the atrial activities. A more detailed description of the simulation steps and parameters can be found in Chapter 4. The resulting activation maps are shown in the second row of Fig. 6.2. Each pixel in the activation map represents the true activation time of its corresponding cell which is annotated as the time when the cell potential  $V$  reaches a threshold value of  $-40$  mV in the depolarization phase of its action potential. The white pixels belong to the cells that were positioned on a conduction block and did not get activated. Finally, Eq. (6.1) is used to compute the simulated electrograms recorded by an assumed electrode array of size  $77 \times 33$  cells positioned on the center of the tissue at a constant height of  $z_0 = 0.5$  mm, which is denoted by a red rectangle on the maps. The last panels in Fig. 6.2 show example electrograms that are randomly selected from different locations on each tissue. Each electrogram is computed for four different electrode diameters  $d_0 \in \{0.5, 2, 4, 8\}$  mm.

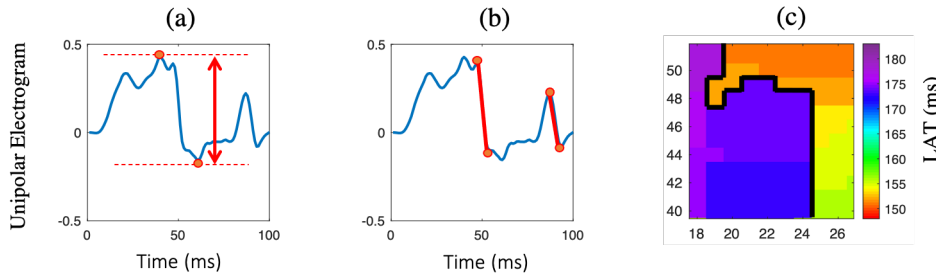


Figure 6.3: (a) Unipolar electrogram with the peak-to-peak voltage denoted by the red two-sided arrow. If the peak-to-peak voltage is smaller than 0.2 V, the EGM will be counted as a low voltage electrogram. (b) Unipolar electrogram from (a) with two of its deflections (downward slopes) denoted by red lines. As can be seen there are more deflections in the signal but we only count those with an average slope that is smaller than -0.02 V/ms. (c) Example activation map (a segment of T7 in Fig. 6.10) with the lines of block denoted by black lines. These are the areas between two neighboring cells with delays in LAT that are larger than 0.7 ms.

#### 6.2.4. CLINICAL STUDIES

The study population consisted of 10 adult patients undergoing surgery in the Erasmus Medical Center Rotterdam. This study was approved by the institutional medical ethical committee (MEC2010-054/MEC2014-393) [82, 83]. Written informed consent was obtained from all patients. Patient characteristics (e.g., age, medical history, cardiovascular risk factors) were obtained from the patient's medical record. Epicardial high-resolution mapping was performed prior to commencement to extra-corporal circulation, as previously described in detail [84]. A temporal bipolar epicardial pacemaker wire attached to the RA free wall served as a reference electrode. A steel wire fixed to subcutaneous tissue of the thoracic cavity was used as an indifferent electrode. Epicardial mapping was performed with a 192-electrode array (electrode diameter 0.45 mm, inter-electrode distances 2.0 mm). The electrode array is subsequently positioned visually by the surgeon on 9 mapping atrial sites using the anatomical borders. We only use the data recorded from Bachmann's bundle. Ten seconds of induced AF were recorded from every mapping site, including a surface ECG lead, a calibration signal of 2 mV and 1000 ms, a bipolar reference EGM and all unipolar epicardial EGMs. Data were stored on a hard disk after amplification (gain 1000), filtering (bandwidth 0.5 to 400 Hz), sampling (1 kHz) and analogue to digital conversion (16 bits).

6

#### INTERPOLATING (CLINICAL) ELECTROGRAMS AND ESTIMATING ELECTROGRAMS FOR DIFFERENT ELECTRODE SIZES

Due to the unstable and unpredictable nature of electrical wave propagation during AF, it is not possible to repeat similar recordings with different electrode arrays (having different electrode diameters and therefore different inter-electrode distances) during AF. To overcome this issue and to interpolate and estimate the electrograms recorded with different arrays, we first estimate high resolution transmembrane currents and subsequently model the effect of larger electrode dimensions. We discretize the 3D tissue activity in space. We use source clamping and replace each block of cells in the real three dimensional tissue with a modeled “cell” on a uniform 2D grid of cells similar to the simulated data. Next,

we estimate the high resolution transmembrane currents using Eq. (6.4) and the recorded electrograms. This can be done by solving the following regularized optimization problem as suggested in Chapter 5

$$\min_I \quad \|\phi - S_0(R_0 \ast\ast I)\|_2^2 + \lambda \|I'\|_1 \quad (6.7)$$

where

$$\|I\|_2^2 := \sum_x \sum_y \sum_t |I[x, y, t]|^2, \quad \|I'\|_1 := \sum_x \sum_y \sum_t |I'[x, y, t]|$$

and where  $\lambda$  is the regularization parameter. Employing the  $\ell_1$ -norm regularization function (i.e.,  $\|\cdot\|_1$ ) helps to preserve the main features of the transmembrane currents among which sparse fast temporal changes (deflections). These are of high importance for correct LAT estimation. More details on an efficient approach to solve Eq. (6.7) can be found in [62]. After estimating the high resolution transmembrane current, we can estimate different electrograms for varying electrode sizes and inter-electrode distances using Eq. (6.4) with an appropriate transfer function from Eq. (6.6).

### 6.2.5. ELECTROGRAM ANALYSIS

Here, we introduce four measures that are used to characterize the properties of the electrogram arrays. Notice that both simulated and clinical electrograms' amplitudes are scaled with a constant value so that the amplitude of the electrograms of a homogeneous wave propagating through the tissue (as in tissue type T0) recorded by the smallest electrode ( $d_0 = 0.5$  mm) equals 1 V. The scaling value is different for clinical and simulated recordings but similar for different electrode sizes. We characterize the properties of the simulated and clinical high resolution electrogram arrays recorded during one atrial beat using the following four measures:

1. **LATE:** percentage of large absolute errors in LAT estimation denoted by LATE. These are the error values that are larger than 10 ms. This measure is only evaluated for simulated tissue where we have access to true activation times. The true activation time is annotated as the time when the potential of the cell that is exactly under the electrode reaches the value of -40 mV, insuring that the action potential is triggered. The estimated activation time of the simulated electrogram is annotated as the point with the steepest descent. The threshold value of 10 ms was selected heuristically. However different threshold values yield a similar pattern of changes.
2. **LSC/B:** length of lines of slow conduction or block in the tissue denoted by LSC/B. To compute this value we first find the delay between each cell and its four direct neighbors on the grid of cells. If the delay is bigger than 0.7 ms it will be considered as a slow conduction or block with the length of  $\Delta x$ . This threshold value is selected with respect to the standard delay between neighboring cells estimated from the standard tissue T0. Note that this is not a small threshold considering the cell-to-cell distances of  $\Delta x = 0.5$  mm in the simulation. Moreover, since we model inhomogeneity in the tissue using dots and small lines of block, their effects on the LAT also ranges from very small to large values. Fig. 6.3 (b) shows an example activation map with its lines of slow conduction or block denoted by thick black lines.

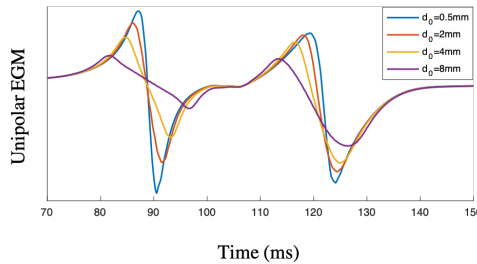


Figure 6.4: An example of a simulated atrial activity recorded using different electrode sizes.

3. **LVA**: percentage of electrograms with lower peak-to-peak voltage than 0.2 V denoted by LVA. The peak-to-peak voltage is defined as the difference between the maximum and the minimum electrogram amplitude and is shown in an example electrogram in Fig. 6.3 (a). The threshold value was selected heuristically, making sure it is small enough to indicate the changes in between different tissue types and electrode diameters.
4. **ND, SD, and MD**: percentage of electrograms having no deflection (ND), a single deflection (SD), or multiple deflections (MD). We only count the deflections having an average slope smaller than  $-0.02\text{ V/ms}$ . The threshold value was selected heuristically to avoid small negligible deflections caused by noise and artifacts. Fig. 6.3 (c) shows an example electrogram with 2 deflections.

It is important to note that all the measures are evaluated for high resolution electrogram arrays assuming that there is one electrode on top of each cell. This is not possible in practice because the inter-electrode distance should be larger than the electrode diameter. However, the results will confirm that the changes in the measures are due to the changes in the electrode size and not due to the different inter-electrode distances. The above mentioned measures are computed using custom written MATLAB codes.

## 6.3. SIMULATION RESULTS

### 6.3.1. EFFECT OF ELECTRODE SIZE ON ELECTROGRAM PROPERTIES

In this section, we investigate the effect of the electrode size on the properties of the simulated electrograms using the measures we introduced in Section 6.2.5. Five randomly generated conductivity maps were modeled for each tissue type T1 to T3, which were previously shown in Fig. 6.2. The tissues were stimulated with one or two activation waves entering the tissue from different locations and the resulting electrograms were computed for four different electrode diameters  $d_0 \in 0.5, 2, 4, 8\text{ mm}$ . The last row of Fig. 6.2 shows an example electrogram from each tissue computed for the four different electrode diameters. For a better comparison, Fig. 6.4 also shows simulated electrograms for different electrode sizes in one plot. These electrograms belong to T5 in Fig. 6.5 with two distinct deflections as a result of a long line of block (for more details see Section 6.3.4).

The measures introduced in Section 6.2.5 were evaluated for all  $2541 \times 5 = 12705$  simulated electrograms of each tissue type ( $77 \times 33 = 2541$  electrograms per map) and are presented in Tables 6.1 to 6.4. As can be seen in the resulting tables, increasing the electrode size increases the error in LAT estimation while the length of detected slow conduction or block lines in the tissue decreases. Except for the homogeneous tissue T0, where using bigger electrode diameters results in an increase in LSC/B which is almost similar for all electrode diameters. As a result, the final activation maps seem smoother. This will be discussed in more detail in Section 6.3.2.

The percentage of low voltage areas in the tissue also increases by increasing the electrode size, indicating that using bigger electrodes decreases the amplitudes of recorded electrograms. However, by comparing the results of lower voltage areas in Tables 1 to 3, it seems that a larger diameter is more useful at indicating the differences in low voltage areas of different tissue types and respectively the mean conductivity of the underlying substrate, even if the discrete block lines in the simulation are missed.

The percentage of single and multiple deflections in the electrograms decreases by increasing the diameter. This is because the slope of some of the deflections gets very small and it will not be annotated as a deflection anymore.

Table 6.1: Measures evaluated for  $m = 77 \times 33$  EGMs of tissue type T0.

d0 (mm)	LATE %	LSC/B (cm)	LVA %	No. Deflections %		
				ND	SD	MD
<b>0.5</b>	0	0	0	0	100	0
<b>2</b>	0	46.2	0	0	100	0
<b>4</b>	0	41.25	0	100	0	0
<b>8</b>	0	44.55	0	100	0	0

Table 6.2: Measures evaluated for  $m = 77 \times 33 \times 5$  EGMs of tissue type T1.

d0 (mm)	LATE %	LSC/B (cm)	LVA %	No. Deflections %		
				ND	SD	MD
<b>0.5</b>	0.97	86.15	0	0.97	70.70	28.32
<b>2</b>	2.36	80.18	0.07	98.09	1.90	0
<b>4</b>	5.23	79.37	0.90	99.26	0.73	0
<b>8</b>	18.79	66.10	25.42	100	0	0

Table 6.3: Measures evaluated for  $m = 77 \times 33 \times 5$  EGMs of tissue type T2.

d0 (mm)	LATE %	LSC/B (cm)	LVA %	No. Deflections %		
				ND	SD	MD
<b>0.5</b>	2.35	98.24	0	2.30	65.54	32.14
<b>2</b>	6.07	85.11	0.72	98.64	1.35	0
<b>4</b>	12.61	82.63	7.41	99.39	0.60	0
<b>8</b>	38.57	68.35	71.54	100	0	0

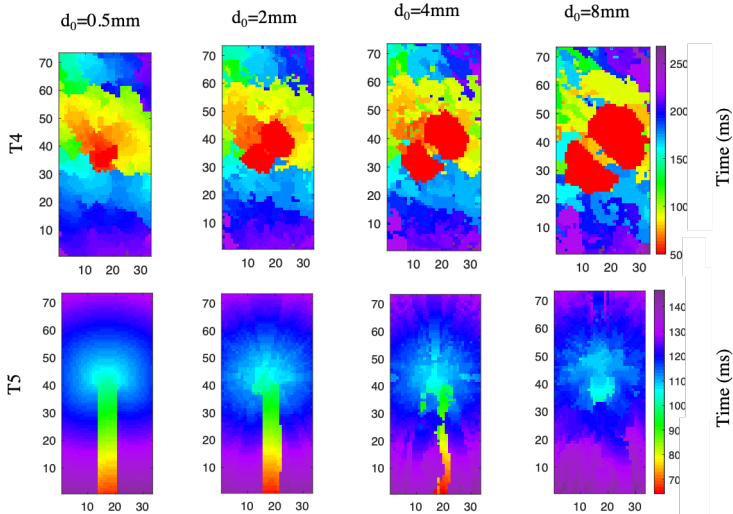


Figure 6.5: Activation map estimated from high resolution electrogram arrays with different electrode sizes. T4 has the same tissue conductivity pattern as T2 and in T5 two lines of block are positioned along the center of the tissue.

6

Table 6.4: Measures evaluated for  $m = 77 \times 33 \times 5$  EGMs of tissue type T3.

<b>d0 (mm)</b>	<b>LATE %</b>	<b>LSC/B (cm)</b>	<b>LVA %</b>	<b>No. Deflections %</b>		
				<b>ND</b>	<b>SD</b>	<b>MD</b>
<b>0.5</b>	11.19	115.03	0.32	10.01	62.19	27.79
<b>2</b>	32.61	94.06	17.35	97.99	2.00	0
<b>4</b>	49.34	84.16	65.09	98.58	1.41	0
<b>8</b>	72.19	65.44	99.28	99.89	0.10	0

However, as can be seen in the tables, the variations in electrogram properties caused by using different electrode diameters are more evident in tissues with higher level of heterogeneity or more scarred tissues. This also indicates that electrograms generated in homogeneous tissues will not be much affected by the electrode diameter.

### 6.3.2. EFFECT OF ELECTRODE SIZE ON THE ACTIVATION MAP

We use some examples to visualize the effect of electrode size on the resulting activation maps. As discussed earlier in Section 6.3.1, using bigger electrode sizes increases the error in LAT estimation and decreases the length of detected conduction block lines. This happens because the electrograms recorded by bigger electrodes are affected more by neighboring activities. Therefore, the deflection generated by larger and stronger inhomogeneous waves in the neighborhood may over-impose the small, but main, local deflections. As a result, the final activation maps seem smoother and more homogeneous.

Fig. 6.4 shows an example of a simulated atrial activity recorded using different elec-

trode sizes. As can be seen, two deflections are visible in each activity. The first deflection (at 90 ms) belongs to the local main activity and the second deflection (at 123 ms) belongs to a strong neighboring activity. As the electrode size increases, the second deflection gets steeper compared to the first deflection. Annotating the steepest descent as the LAT will then result in annotating the second deflection for electrode of diameters  $d_0 = 4$  mm and 8 mm. That is an absolute error of about 33 ms in LAT estimation.

Fig. 6.5 shows estimated activation maps of two simulated tissues recorded using electrode arrays having different electrode sizes. These examples imitate the two patterns of common changes that we observed in clinical cases. T4 has the same tissue conductivity pattern as T2 (medium density of conduction blocks) with a different stimulation pattern (explained in Section 6.2.3) resulting in generation of complex fractionated atrial electrograms. As can be seen, small waves in the tissue are over-imposed by larger and stronger activities in their surrounding and the smooth variations from one color to another are replaced by sharp variations. In T5 (second row of Fig. 6.5) two lines of block are positioned along the center of the tissue. The activation map starts from the area in-between these lines and then propagates through the whole tissue. As can be seen, this abnormal area is completely lost when we use bigger electrode sizes. As mentioned before, this happens because the activities generated in this abnormal area have lower amplitude compared to the stronger activities outside the block lines and an electrode with a bigger size records more activities from its neighborhood. We discuss this case in more detail in Section 6.3.4.

## 6

### 6.3.3. OPTIMAL ELECTRODE DIAMETER AND INTER-ELECTRODE DISTANCE

The electrode transfer function in Eq. (6.6) and shown in Fig. 6.1 can be used for calculating the optimal electrode diameter and inter-electrode distance. This can be done by investigating the FWHM of different electrode diameters. Fig. 6.6 shows the calculated FWHM as a function of the electrode diameter (with  $z_0 = 0.5$  mm). This plot has two important features. First, even for a point electrode,  $\text{FWHM} = 1.73$  mm is nonzero. This is because of the electrode height  $z_0 > 0$ . Secondly, FWHM is almost constant for small diameters and the curve bends around  $d_0 = 0.5$  mm. These observations can lead to two important conclusions:

- (i) Optimal electrode diameter: an optimal electrode diameter is around  $d_0 = 0.5$  mm. This is the largest value with a similar FWHM to a point electrode. Note that smaller electrodes are affected more by noise so there is a trade-off between high SNR and small FWHM. Therefore, it is also not preferred to use the smallest electrode possible.
- (ii) Optimal inter-electrode distance (in order to capture all the spatial information of the electrical activities in the tissue): To find this parameter, we first need to estimate the maximum spatial frequency that is presented in electrical activities. This can be a quite complicated task due to the three dimensional inhomogeneous structure of the atrial tissue and the complex unstable wave propagation patterns. On the other hand, no matter how high these spatial frequencies are, they will eventually be recorded by surface electrodes which inherently perform as a spatial low-pass filter. As shown in Chapter 5, the FWHM discussed in Section 6.2.2 can be also used as a short-hand measure of the appropriate inter-electrode distance. As an example for an electrode with  $d_0 = 0.5$  mm, we suggest an optimal inter-electrode distance of around 1.9 mm, which is equal to its FWHM at  $z_0 = 0.5$  mm.

Fig. 6.7 shows the FWHM as a function of both  $d_0$  and  $z_0$ . As can be seen in this figure, as the electrode diameter or the electrode height (or equivalently tissue thickness) increases, the required inter-electrode distance also increases. This means that FWHM and the low-pass filtering effect of the electrode increases. This will result in losing spatial information by electrodes. Even putting them closer to each other in an array will not compensate that loss. Therefore, we can effectively use larger inter-electrode distances. Conversely, electrodes with smaller diameters have smaller FWHM and can potentially capture spatial information with higher frequencies and by putting these electrodes closer to each other on an array, we can record this information.

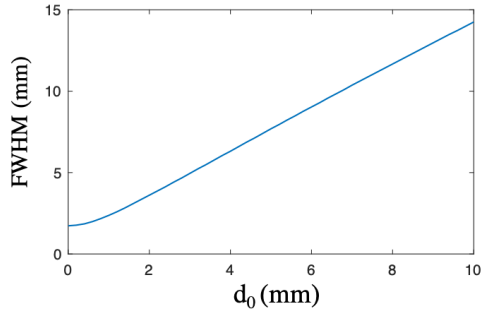


Figure 6.6: FWHM calculated for different electrode diameters with  $z_0 = 0.5$  mm.

6

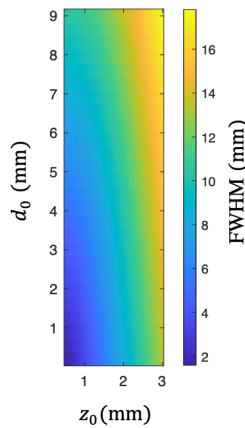


Figure 6.7: The estimated FWHM for different values of  $d_0$  and  $z_0$ .

### 6.3.4. MAXIMUM ELECTRODE SIZE FOR RECORDING SCARRED TISSUE

In this section, we perform an experiment to investigate the maximum electrode size for the detection of abnormal areas and conduction block lines using simulated tissue. We use

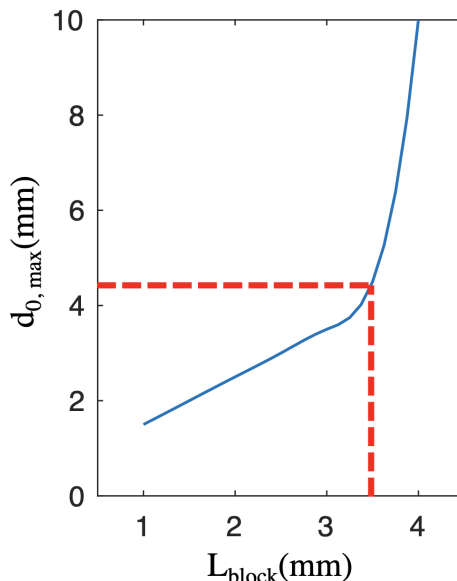
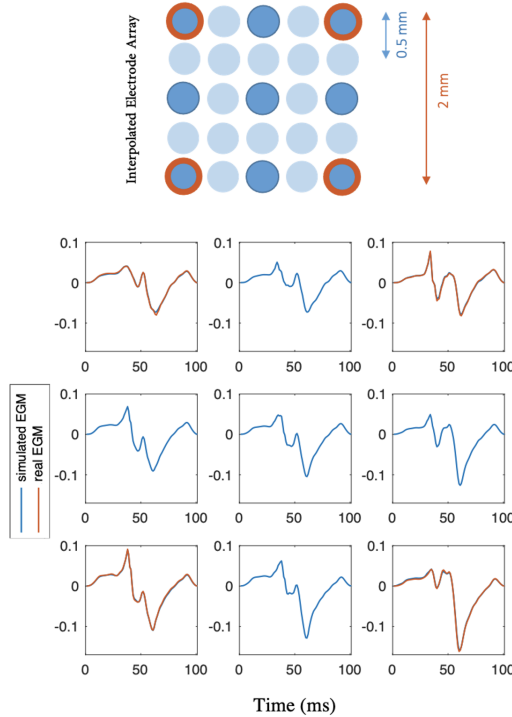


Figure 6.8: Maximum electrode diameter  $d_{0,max}$  for recording a visible scarred tissue, as a function of  $L_{block}$  which denotes the distance between two lines of block.

the same pattern as in T5 in Fig. 6.5 for the scarred tissue where two lines of conduction block are positioned along the center of the tissue with a distance of  $L_{block}$ . The activation wave starts from the area in between these lines and then propagates through the whole tissue. As can be seen in T5, this abnormal area is completely lost when we use bigger electrode sizes. As mentioned before, this happens because the activities generated in this abnormal area have lower amplitude compared to the stronger activities outside the block lines and an electrode with a bigger size records more activities from its neighborhood. We increased the distance between the two parallel lines of blocks and visually inspect the activation map estimated from different electrode arrays to determine the maximum electrode diameter  $d_{0,max}$  that can still provide some evidence of the abnormality in the tissue. The results can be seen in Fig. 6.8. As an example, the two block lines in T5 are distanced at  $L_{block} = 3.5$  mm, and, as can be seen in Fig. 6.8, the maximum electrode diameter that can still provide an evidence of this abnormality is around 4.2 mm. Notice that this is a simple example compared to complex clinical cases where the results are affected by many underlying parameters of the tissue.

## 6.4. CLINICAL RESULTS

As discussed in Section 6.2.4, due to the unstable and unpredictable nature of electrical wave propagation during AF, it is not possible to repeat similar clinical recordings with different electrode arrays. Therefore, to model these recordings, we use our approach presented in Section 6.2.4 to first estimate high resolution transmembrane currents and then use



6

Figure 6.9: Real (in orange) and interpolated/simulated electrograms (in blue) for clinical recordings with  $d_0 = 0.5\text{mm}$ . Note that for an easier inspection, only electrograms from dark blue electrodes have been shown.

them to interpolate and calculate electrograms with bigger electrode sizes. The methodology used for estimation of transmembrane current is discussed and evaluated in [62]. Here, to evaluate its performance in reproducing the electrograms, we find the mean correlation coefficient between the real clinical electrograms and their simulated electrograms after finding the transmembrane currents and recalculating the electrograms. The mean correlation coefficient is equal to  $0.97 \pm 0.004$  (mean  $\pm$  standard deviation) which indicates a good simulation. Note that we can only calculate this measure for the low resolution  $24 \times 8$  clinical electrograms and for  $d_0 = 0.5$  mm, as we do not have the ground-truth EGMs for bigger electrode sizes or higher resolutions. Fig. 6.9 shows four neighboring clinical (real) EGMs (in orange) and the interpolated electrograms in between them.

#### 6.4.1. STATISTICAL ANALYSIS

A similar analysis as in Section 6.3.1 was performed on 10 clinical electrogram arrays of size  $24 \times 8$  recorded from Bachmann's bundle for 10 different patients. The signals were recorded for 10 seconds during induced AF resulting in fractionated electrograms with various levels of fractionation. Note that the electrograms were initially interpolated and modeled for different electrode sizes. This resulted in  $24 \times 8 \times 4$  electrograms in total. The measures introduced in Section 6.2.5 were evaluated for one atrial beat of length 150 ms

(visually selected to make sure each electrogram contained atrial activity) and are presented in Table 6.5. We did not present the result for the error in LAT estimation because we do not have access to the true values in clinical data. As can be seen in the table, the changes in the properties of electrograms recorded using different electrodes follows the same pattern as for the simulated data.

Table 6.5: Measures evaluated for  $24 \times 8 \times 4^2 \times 10$  interpolated clinical electrograms recorded from Bachmann's bundle

d <sub>0</sub> (mm)	LSC/B (cm)	LVA %	No. Deflections %		
			ND	SD	MD
0.5	80.34	47.38	71.31	25.56	3.12
2	68.47	53.13	77.72	20.99	1.27
4	59.95	60.28	84.25	15.62	0.12
8	56.09	78.40	93.46	6.52	0.00

#### 6.4.2. CHANGES IN ACTIVATION MAPS

Similar patterns as in Section 6.3.2 are also seen in the clinical data. Fig. 6.10 shows two examples of how the high resolution activation maps change by using different electrode sizes. As expected, the small deflections and small wavelets in T6 are over-imposed by larger and stronger activities in their surrounding area as the electrode size increases. This leads to a decrease at the total number of wavelets in the area. T7 also shows an example where the abnormal area with long delays in the activation map is partly or completely missed due to the increase in the electrode size.

#### 6.4.3. SCALING ELECTROGRAMS' AMPLITUDE

A proper scaling of the electrograms' amplitudes recorded with different electrode sizes can to some extent compensate for differences in the measures that characterize the electrograms. We propose to use the ratio between the norm of the transfer functions of the electrodes for scaling their amplitudes for a better comparison of their recorded electrograms. This can be formulated as

$$\hat{\phi}_{d_0}(x_m, y_m, t) = \frac{\|R_0(r)\|_2}{\|R_{d_0}(r)\|_2} \phi_{d_0}(x_m, y_m, t) \quad (6.8)$$

where  $R_0(r)$  and  $R_{d_0}(r)$  are calculated from Eqs. (6.5) and (6.6),  $\hat{\phi}$  is the scaled electrogram, and  $\|\cdot\|_2$  is the Euclidean norm or  $l_2$ -norm. This will make the measures like LVA and the number of deflections, more invariant to the electrode diameter. However, it will not affect the estimation of LATs, or any parameter that is extracted from it like LSC/B.

Table 6.6 shows the new measures (cf. the non-scaled version in Table 6.5) after using the norm of the distance kernel for scaling the data. Notice that approaches like the maximum amplitude or steepness of the recorded electrograms for scaling or normalizing them are realization based and thus less stable. Such parameters will depend on the propagation patterns and are prone to spatial and temporal variations, making the results incomparable and not generalizable.

Table 6.6: Measures evaluated for  $24 \times 8 \times 4^2 \times 10$  interpolated clinical electrograms recorded from Bachmann's bundle after scaling the electrograms.

d0 (mm)	LSC/B (cm)	LVA %	No. Deflections %		
			ND	SD	MD
0.5	80.34	47.38	71.31	25.56	3.12
2	68.47	46.62	74.11	24.13	1.75
4	59.95	47.67	77.20	22.19	0.59
8	56.09	52.40	82.41	17.47	0.10

## 6.5. DISCUSSION AND CONCLUSION

In this chapter, we studied the effect of electrode size on the properties of the recorded electrograms. We started by simulated electrograms of 2D atrial tissues and present the effect of different electrode sizes on electrogram properties including the error in LAT estimation, the length of slow conduction or blocks (LSC/B) observed on the resulting activation map, percentage of observed low voltage areas (LVA), and the number of deflections in the recorded electrograms. The results were then tested on clinical electrograms of 10 patients recorded from Bachmann's bundle. Since we had no access to the recorded electrograms recorded with different electrode diameters, we first estimated the high resolution transmembrane current maps using the approach in Chapter 5 and then used the currents and the electrode transfer function to generate such recordings. The results were comparable to those of simulated data.

The results show that using bigger electrodes produces larger error in LAT estimation, which is in accordance with previous results shown in a previous study [66]. These errors in LAT estimation will result in the estimation of a smoother activation map than the true map. These results were also observed in experiments on clinical bipolar electrograms in [74, 76].

The electrograms recorded with a bigger electrode size are in general smoother with smaller slopes and smaller peak-to-peak voltages. Some of the deflections in these signals are so smooth that they are not annotated as a deflection in the recording. This will result in an increase in low voltage areas in the tissue, which agrees with the result of previous studies in [63, 77]. However, if there is no recording with a smaller electrode available for setting the proper thresholds, one might use smaller threshold values for detecting such deflections. This can result in detecting more deflections. This can explain why some studies such as [63, 78, 79] suggest that increasing the electrode size increases the fractionation level in the tissue.

However, by comparing the results of lower voltage areas in Tables 1 to 4, it seems that a larger diameter is more useful at indicating the difference in low voltage areas in between different tissue types with different inhomogeneity levels. Considering that in the inhomogeneous cardiac tissue lower conductivity also means lower voltage in that area, we can conclude that bigger electrodes are more useful at indicating the mean conductivity of the underlying substrate, even if the discrete slow conduction or block lines in the activation map are missed.

Although these conclusions have been partly discussed or hinted in previous studies, in the current study, we developed a more systematic approach. By employing the elec-

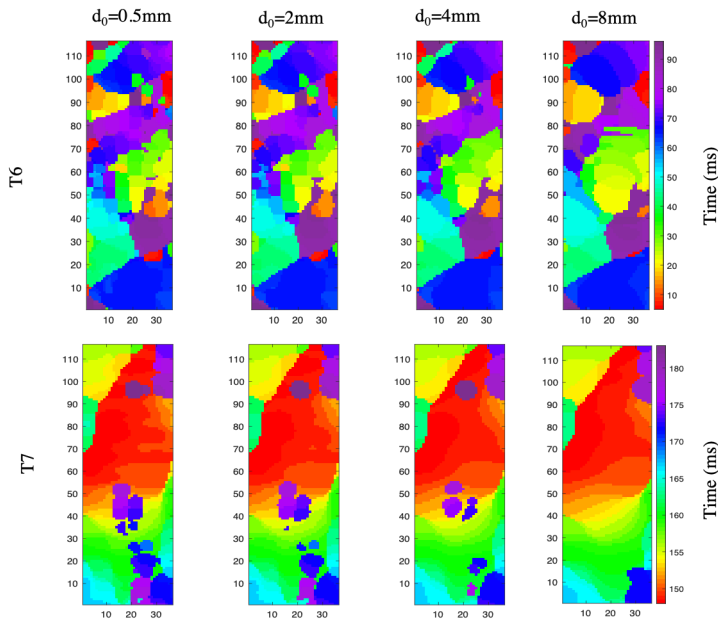


Figure 6.10: Example activation maps estimated from high resolution electrogram arrays with different electrode sizes, estimated from clinically recorded electrogram arrays.

trophysiological models and the electrode transfer function, we could analyze and discuss these effects in more depth. Moreover, the introduced approach for interpolating and modeling clinical electrograms with different electrode sizes allowed us to investigate these effects for recordings of similar wave propagation patterns. It also enabled us to only focus on the electrode diameter and not the inter-electrode distances.

Moreover, we discussed the effect of the optimal electrode diameter and the required inter-electrode distances (or the array resolution) for capturing all the possible spatial information. We performed an experiment to investigate the required minimum electrode size for capturing an inhomogeneous activity in between two parallel block lines in the tissue. We also introduced a proper way for scaling electrograms with different electrode diameter for a better comparison.

These results show the importance of the recording electrode array on the properties of the electrograms, and this needs to be considered in any further evaluation and analysis of the data; especially if considered for treatment such as electrogram-based ablations.

### 6.5.1. STUDY LIMITATIONS

In this study, we modeled the 3D tissue of the atria as a 2D grid of cell assuming a constant electrode height of  $z_0$  for the whole tissue that is under the electrode array. Although 3D forward tissue models of the atria with varying values  $z_0$  have already been developed in literature, employing them in an inverse problem for estimation of transmembrane current is not practical due to the complexity of these models. Moreover, that would require a proper

estimation of  $z_0$  for each recording site beforehand.

We did not have access to electrograms recorded from similar locations and different electrode sizes for a more complete evaluation of our results, as this is not possible in practice due to the temporal and spatial variations of the underlying wave propagation patterns during AF and especially for areas with complex fractionated electrograms.

The clinical electrograms used in this study were recorded from Bachmann's bundle with a predominant route of conduction from right to left and with a potential role in AF [85] which may differ from the rest of atria. However, there are already regional differences in potentials in atria even during SR [86]. Although our method does not depend on these specific properties, the exact results in Tables 6.1 to 6.6 may not be generalizable to other regions in atria.

We used similar threshold values for evaluation of the measures introduced in Section 6.2.5 for simulated and real electrograms. Although both types of electrograms were scaled such that a homogeneous planar wave has a maximum absolute amplitude of 1 V, exact selection of these parameters is more prone to error in real electrograms as we do not have access to such exact recordings. Moreover, we ignored the effect of noise in our simulations. Although smaller electrodes provide sharper and more localized recordings, they are more affected by noise and artifacts. Therefore, using a smaller electrode may not always improve the recordings.



# 7

## CONCLUSION

In this chapter, we conclude this dissertation and provide a summary of our conclusions in response to the research questions that were posed in Chapter 1. We also address some limitations and assumptions that need to be taken into account in further studies. Some open problems and our suggested solutions are also discussed in future work.

### 7.1. CONCLUSION

Throughout this thesis, in response to the research questions that we posed in Chapter 1, we developed a simplified electrophysiological model for atrial electrograms and used it in different applications for providing a better estimation or understanding of the underlying tissue parameters that are important for studying and analyzing AF. In this section, we conclude and discuss our answers to each research question.

#### 7.1.1. SIMPLIFIED ELECTROGRAM MODEL FOR TISSUE PARAMETER ESTIMATION

The electrical propagation in tissue is governed by electrophysiological models and is directly connected to its underlying parameters. Detailed realistic electrophysiological models of electrograms are very useful for analyzing the effect of tissue properties on generated electrograms or studying wave propagation patterns in forward simulations. However, using these models in inverse problems of extracting tissue properties from electrograms, is nearly impossible. This is due to the large number of parameters that need to be estimated. However, our hypothesis was that understanding AF and improving its therapy starts with developing a proper forward model that is accurate enough (from a physiological point of view) and simultaneously simple enough to allow for subsequent parameter estimation. Therefore, we proposed the following research question:

**Q1.** Can we simplify the underlying electrophysiological models of electrograms for tissue parameter estimation using well known signal processing approaches?

Our answer to this question is:

**A1.** As shown and discussed in Chapter 4, it is possible to develop a simplified forward model for electrograms in a compact matrix representation, using a parsimonious parametrization. We showed that this simplified model can efficiently explain the observed electrograms' morphology based on the tissue conductivity and local activation times. To investigate the effectiveness of the model we also investigate its performance throughout other chapters.

However, we need to acknowledge that for 3D tissues, where each layer of tissue might have different properties and different wave propagation patterns, our model needs to be further developed.

### 7.1.2. ESTIMATION OF UNDERLYING TISSUE PARAMETERS

#### TISSUE CONDUCTIVITY ESTIMATION

The electrical propagation in tissue is particularly related to the tissue intracellular conductivity. It plays an important role in the underlying dynamics and functional connections in the tissue as a mechanism of inter-cellular communication. The estimation of these hidden parameters can be essential in the diagnosis and staging of the disease. Despite the beneficial effect of conductivity in analyzing electropathology, the complexity of the electrophysiological models makes its estimation challenging and not practical in clinical settings. Therefore, we proposed the following research question:

**Q2.1.** Can we use the proposed simplified model for estimation of tissue conductivity?

Our answer to this question is:

**A2.1.** As shown and discussed in Chapter 4, we can use the proposed simplified model for estimation of tissue conductivity. To do so, we reformulated our simplified model to show its linear dependence on the conductivity vector, enabling the estimation of this parameter from the recorded electrograms. The results show that, despite the low resolution and all simplifying assumptions, the model can efficiently estimate the conductivity map and regenerate realistic electrograms, especially during sinus rhythm. The provided examples show that our method outperforms the other reference approaches especially in case of anisotropy and inhomogeneity in the tissue.

However, we need to acknowledge that the presented algorithm may not perform well in cases where our underlying assumptions are not valid. These can happen in two cases. First, when the wavefront is not smooth, as is the case during AF. In this case, multiple wavefronts enter the area of interest simultaneously or one wavefront breaks into multiple wavelets due to the inhomogeneity in the conductivity. This complicates the estimation of the activation times and results in an inaccurate activation map and consequently an inaccurate conductivity map. Therefore, more robust AT estimation algorithms need to be developed. Second, the presented algorithm may not perform well for 3D tissues where each layer of tissue might have a different conductivity map and wavefront propagation. In this case our model, like any other approach that uses electrograms, images all the activities on the 2D tissue surface and ignores the underlying layers. Although this can be partly solved by developing 3D models of the tissue following the same principles as in 2D, the main problem would be the estimation of the ATs in the underlying layers which is currently not possible in clinical recordings.

### IMPROVED LAT ESTIMATION

If the tissue is inhomogeneous or multiple excitation wavefronts are propagating in the electrode neighborhood, the recorded EGM may contain nonlocal (far-field) deflections and the steepest descent annotated as the LAT might belong to a far-field excitation and not to the local activity. This makes the estimation of LATs prone to errors and will negatively affect the estimation of other parameters that depend on them. Therefore, we proposed the following research question:

**Q2.2.** Can we use our developed model for a better estimation of LAT in fractionated electrograms?

Our answer to this question is:

**A2.2.** As shown and discussed in Chapter 5, we can use electrophysiological electrogram models to propose algorithms that incorporate spatial information for an improved LAT estimation. Our approach reduces the spatial blurring effect that is inherent to electrogram recordings, using spatial deconvolution. Our results on simulated and clinically recorded data show that using steepest descent for estimating LATs is prone to make the activation maps smoother by ignoring local small deflections. This arises in situations where the local activities belong to a wavefront that only invades a small part of the mapping area. The activities generated by this wavefront are thus smaller in amplitude compared to the nonlocal activities that belong to a wavefront that covers a larger area. The deconvolution, on the other hand, reduces the effect of nonlocal activities and amplifies the local activities, which results in a better estimation of true local deflection. This can result in estimation of activation maps that are less smooth and more irregular with probably more distinct wavefronts. It also changes the location of estimated (functional) conduction blocks or collision lines in the tissue.

It is important to note that, in this study, we replaced each block of 3D tissue with a modeled cell in a 2D mono-layer tissue with constant cell-to-cell distance, ignoring the tissue curvature and thickness, which might affect the results. Moreover, we assumed a constant electrode height, while it might be subject to spatial variation and quality of contact. Due to complications of simulating 3D tissue, the performance of the proposed approach was tested on two-dimensional simulated tissue. Since we do not have access to the true local activities of clinically recorded electrograms, we used manual annotation to analyze the performance of the approach.

### 7.1.3. THE EFFECT OF ELECTRODE SIZE ON ELECTROGRAM PROPERTIES

The properties of electrograms depend to a large extent on the physical dimensions of the electrode arrays that are used for recording these signals. The electrode size is an important parameter that can affect the characteristics of the recorded electrograms including SNR, fractionation level, and voltage level. Therefore, it is important to provide a thorough investigation on these effects. However, it is not possible in practice to provide simultaneous recordings of the same propagation pattern in tissue with different electrode sizes as these pattern may change (especially during AF). Therefore, we proposed the following research question:

**Q3.** Can we use the electrogram model to simulate clinical electrograms recorded by

different electrode sizes and use them to analyze the effect of electrode size on electrogram properties?

Our answer to this question is:

**A3.** As shown and discussed in Chapter 6, we can use the electrogram model to first estimate high resolution transmembrane current maps for clinical electrograms and then used the currents and the electrode model to estimate recordings with different electrode sizes. We also simulated electrograms of 2D atrial tissues. We presented the effect of different electrode sizes on clinical and simulated electrogram properties including the length of the block line, observed on the resulting activation map, percentage of observed low voltage areas, percentage of electrograms with low maximum steepness, and the number of deflections in the recorded electrograms. The results show that using a bigger electrode provides a smoother activation map, because the small deflection in the tissue will be over-imposed by large neighboring activities. The resulting electrograms are in general smoother, with smaller steepness and voltages. Some of the deflections will be so smooth that they will not be annotated as a secondary deflection. Moreover, we discussed the effect of the required inter-electrode distances (or the array resolution) for capturing all the spatial information. We introduced a proper way for scaling the resulting electrograms so that the results are comparable. We also performed an experiment to investigate the required minimum electrode size for capturing an inhomogeneous activity in between two parallel block lines in the tissue.

In is important to note that, as mentioned before, we modeled the the 3D tissue of the atria as a 2D grid of cells assuming a constant electrode height of  $z_0$  for the whole tissue that is under the electrode array. Although 3D forward tissue models of the atria with varying electrode height have been already developed in literature, employing them in an inverse problem for estimation of transmembrane current is not practical due to the complexity of these models. We also did not have access to electrograms recorded from similar locations but different sizes for evaluation of our results. This might be difficult in practice for the complex fractionated electrograms recorded during AF used in this study, due to the temporal and spatial variations of the underlying wave propagation patterns. Note that in this study, we ignored the effect of noise. It is has been shown in the literature that, although smaller electrodes provide sharper and more localized activity, they are more heavily affected by noise and artifacts leading to a smaller SNR.

## 7.2. STUDY LIMITATIONS AND FUTURE WORK

In this section, we introduce some of the open questions and our suggested solutions, based on the conclusions we draw in this dissertation.

### IMPROVED VENTRICULAR ACTIVITY REMOVAL

Our proposed approach in Chapter 3 exploits the temporal properties of ventricular activities by using electrograms recorded during multiple atrial beats. After putting all these activities in a matrix, we constructed an appropriate data matrix and introduced a matrix

decomposition problem, for an improved removal of ventricular activities. The approach only uses one electrogram recording, while in most studies we have access to high resolution spatio-temporal electrogram recordings. The spatial information can potentially improve the ventricular activity removal either by forming a data tensor or by expanding the previous data matrix to include electrograms recorded in multiple locations.

### 2.5D MODELING OF THE TISSUE USING SIMULTANEOUSLY RECORDED EPICARDIAL AND ENDOCARDIAL ELECTROGRAMS

Although 3D electrophysiological models of the atrial tissue have been developed in the literature, as stated before, due to their complexity, they are hard to use in signal processing approaches. However, a feasible practical solution to this problem can be derived by using two layer, also called 2.5D, tissue models together with the simultaneously recorded epicardial and endocardial electrograms. After forming such a model, with some modifications, the approaches introduced throughout this dissertation can be employed.

### IMPROVING CONDUCTIVITY MAP ESTIMATION

We believe that tissue conductivity is an important parameter that can be directly correlated to electropathology in the tissue, and consequently to mechanisms underlying AF. However, our proposed approach in Chapter 4 needs to be improved for a better estimation of conductivity maps, especially during atrial fibrillation. This can be done by: (i) using improved approaches for a better estimation of activation maps, (ii) using electrograms recorded during multiple beats instead of a single beat, (iii) using 3D tissue models. Moreover, for a thorough investigation of wave propagation patterns and electropathology in the tissue, this approach can be integrated with other approaches that aim to estimate tissue impedance by injecting current to the tissue.

7

### ESTIMATION OF TISSUE PARAMETERS

There are many parameters involved in estimation of tissue conductivity and/or local activation times. Among these are the electrode height and tissue fibre direction that can have a large impact on the output results. New algorithms are needed to estimate these parameters. In some cases, these parameters can be physically measured, to some extent, on a patient's heart. Using the measured parameters instead of their assumed conventional values, can result in a better estimation of other tissue parameters that depend on them and reduce our uncertainty about the accuracy of our results. Although it might not be practical to measure these parameters for every patient, it will be useful to measure them for an experimental setup.

### EXPERIMENTING ON LIVE HEARTS IN THE LAB

A hindering complication in unravelling a precise and constraining mechanism for AF originates from the uncertainty in measuring and estimating AF relevant parameters in the tissue, especially those that characterize electrical wave propagation. This is mainly because of the fact that the heart is a complex system and the true values of these parameters cannot be accessed, especially not when performing the recordings on a patient's heart during surgery. Animal or human hearts that are kept alive in a laboratory outside of the body have provided many new opportunities for studying AF and its hidden sources. These hearts can be easily manipulated and the parameters of interest can be measured using much more

higher resolution techniques. These data can then serve as a ground truth for evaluation of different signal processing approaches that aim to improve measurement or estimation of these parameters in a patient's heart. This can especially help with developing more accurate activation map estimation techniques because we can intentionally create scarred tissue with different patterns, thickness, and length that can be activated from different locations.

#### MULTILAYER STAINING OF TISSUE

A multilayer staining of the tissue can provide a three-dimensional structural map that can be used in studying correlation between the electrical wave propagation patterns and different structures in the tissue that can be responsible for AF, like fibrosis. To do so, we can first map the wave propagation in the tissue using high resolution micro-electrode arrays and later perform staining on the same tissue. Using the wave propagation pattern, we can identify locations with conduction abnormalities and use the stained tissues to look for structures that can be correlated with those abnormalities.

### 7.3. CLOSING REMARKS

Although this thesis is getting to an end, as discussed in future works more research and development is needed to make our findings applicable in clinical practice. We tried to have a detailed analysis on the wave propagation and tissue parameters starting with the electrophysiological models that govern these propagations. Although it makes our path in relating these parameters to AF much longer, we believe that this is the correct systematic path that needs to be taken. Detours like characterizing electrogram morphology and using machine learning approaches provide features that can help to differentiate between different types of AF or can provide some guidelines in studying AF. However, more comprehensive studies are needed to unravel the true cause(s) of atrial fibrillation.

Various experiments and measurements have been performed on simulated and/or real hearts which are all complicated, expensive and challenging due to their clinical nature. Thus providing a setup that includes all important measurements might not be affordable by one single organization. We believe that this cannot be done without an extensive multi-disciplinary research team where scientists with many different backgrounds join data and analysis that look at the heart and AF from different points of views. Moreover, introducing open source integrated datasets will help to progress the research into AF and hopefully to understand its underlying causes and its proper treatments.

# LIST OF ABBREVIATIONS

AA	atrial activity
AF	atrial fibrillation
AM	activation map
AP	action potential
AV	atrioventricular
BB	Bachmann's bundle
CFAE	complex fractionated atrial electrograms
CM	conductivity map
CMM	compact matrix model for atrial electrograms
CV	conduction velocities
DCT	two-dimensional discrete cosine transform
ECG	electrocardiogram
ED	Eikonal-diffusion
EGM	electrograms
FDM	finite difference method
FEM	finite element method
FVM	finite volume method
FWHM	full width at half maximum
IAF	induced atrial fibrillation
LAT	local activation time
LSC/B	length of slow conduction or blocks
LVA	low voltage areas
SA	sinoatrial
SD	steepest descent
SNR	signal-to-noise ratio
SR	sinus rhythm
PV	pulmonary vein
VA	ventricular activities
2D	two-dimensional



# BIBLIOGRAPHY

## REFERENCES

- [1] I. C. Van Gelder and M. E. Hemels, “The progressive nature of atrial fibrillation: a rationale for early restoration and maintenance of sinus rhythm,” *Europace*, vol. 8, no. 11, pp. 943–949, 2006.
- [2] A. D. Ceornodolea, R. Bal, and J. L. Severens, “Epidemiology and management of atrial fibrillation and stroke: Review of data from four european countries,” *Stroke Research and Treatment*, vol. 2017, pp. 1–12, 2017.
- [3] M. K. Chung, L. L. Eckhardt, L. Y. Chen, H. M. Ahmed, R. Gopinathannair, J. A. Joglar, P. A. Noseworthy, Q. R. Pack, P. Sanders, K. M. Trulock, *et al.*, “Lifestyle and risk factor modification for reduction of atrial fibrillation: A scientific statement from the american heart association,” *Circulation*, vol. 141, no. 16, pp. e750–e772, 2020.
- [4] J. E. Hall and M. E. Hall, *Guyton and Hall textbook of medical physiology e-Book*. Elsevier Health Sciences, 2020.
- [5] A. Yaksh, L. J. van der Does, C. Kik, P. Knops, F. B. Oei, P. C. van de Woestijne, J. A. Bekkers, A. J. Bogers, M. A. Allessie, and N. M. de Groot, “A novel intra-operative, high-resolution atrial mapping approach,” *Journal of Interventional Cardiac Electrophysiology*, vol. 44, no. 3, pp. 221–225, 2015.
- [6] M. S. Guillem, A. M. Climent, M. Rodrigo, F. Fernández-Avilés, F. Atienza, and O. Berenfeld, “Presence and stability of rotors in atrial fibrillation: evidence and therapeutic implications,” *Cardiovascular research*, vol. 109, no. 4, pp. 480–492, 2016.
- [7] J. Jalife, O. Berenfeld, A. Skanes, and R. Mandapati, “Mechanisms of atrial fibrillation: mother rotors or multiple daughter wavelets, or both?,” *Journal of cardiovascular electrophysiology*, vol. 9, no. 8 Suppl, p. S2, 1998.
- [8] N. de Groot, L. van der Does, A. Yaksh, E. Lanters, C. Teuwen, P. Knops, P. van de Woestijne, J. Bekkers, C. Kik, A. Bogers, *et al.*, “Direct proof of endo-epicardial asynchrony of the atrial wall during atrial fibrillation in humans,” *Circulation: Arrhythmia and Electrophysiology*, vol. 9, no. 5, p. e003648, 2016.
- [9] J. W. Waks and M. E. Josephson, “Mechanisms of atrial fibrillation–reentry, rotors and reality,” *Arrhythmia & electrophysiology review*, vol. 3, no. 2, p. 90, 2014.
- [10] E. J. Ciaccio, A. B. Biviano, W. Whang, J. A. Vest, A. Gambhir, A. J. Einstein, and H. Garan, “Differences in repeating patterns of complex fractionated left atrial electrograms in longstanding persistent as compared with paroxysmal atrial fibrillation,” *Circulation: Arrhythmia and Electrophysiology*, vol. 4, pp. 470—477, 2011.

- [11] Y. Takahashi, M. D. O'Neill, M. Hocini, R. Dubois, S. Matsuo, S. Knecht, S. Mahapatra, K.-T. Lim, P. Jaïs, A. Jonsson, *et al.*, “Characterization of electrograms associated with termination of chronic atrial fibrillation by catheter ablation,” *Journal of the American College of Cardiology*, vol. 51, no. 10, pp. 1003–1010, 2008.
- [12] R. Plonsey and R. C. Barr, *Bioelectricity: a quantitative approach*. Springer Science & Business Media, 2007.
- [13] N. Virag, V. Jacquemet, C. Henriquez, S. Zozor, O. Blanc, J.-M. Vesin, E. Pruvot, and L. Kappenberger, “Study of atrial arrhythmias in a computer model based on magnetic resonance images of human atria,” *Chaos: An Interdisciplinary Journal of Nonlinear Science*, vol. 12, no. 3, pp. 754–763, 2002.
- [14] V. Jacquemet, N. Virag, Z. Ihara, L. Dang, O. Blanc, S. Zozor, J. Vesin, L. Kappenberger, and C. Henriquez, “Study of unipolar electrogram morphology in a computer model of atrial fibrillation,” *Journal of cardiovascular electrophysiology*, vol. 14, no. s10, pp. S172–S179, 2003.
- [15] S. Petrucci, J. Ng, G. M. Nijm, H. Al-Angari, S. Swiryn, and A. V. Sahakian, “Atrial fibrillation and waveform characterization,” *IEEE engineering in medicine and biology magazine*, vol. 25, no. 6, pp. 24–30, 2006.
- [16] V. Jacquemet, A. Van Oosterom, J.-M. Vesin, and L. Kappenberger, “Analysis of electrocardiograms during atrial fibrillation,” *IEEE engineering in medicine and biology magazine*, vol. 25, no. 6, pp. 79–88, 2006.
- [17] Wikipedia, “Heart — Wikipedia, the free encyclopedia.” <http://en.wikipedia.org/w/index.php?title=Heart&oldid=990279132>, 2020. [Online; accessed 06-December-2020].
- [18] Wikipedia, “Electrical conduction system of the heart — Wikipedia, the free encyclopedia.” <http://en.wikipedia.org/w/index.php?title=Electrical%20conduction%20system%20of%20the%20heart&oldid=990962552>, 2020. [Online; accessed 06-December-2020].
- [19] P. W. Macfarlane, A. Van Oosterom, O. Pahlm, P. Kligfield, M. Janse, and J. Camm, *Comprehensive electrocardiology*. Springer Science & Business Media, 2010.
- [20] T. of Cardiology, “Conduction system.” [https://www.textbookofcardiology.org/wiki/Cardiac\\_Arrhythmias](https://www.textbookofcardiology.org/wiki/Cardiac_Arrhythmias), note = “[Online; accessed 06-December-2020]”, 2020.
- [21] U. B. Tedrow and W. G. Stevenson, “Recording and interpreting unipolar electrograms to guide catheter ablation,” *Heart Rhythm*, vol. 8, no. 5, pp. 791–796, 2011.
- [22] S. L. Kopecky, B. J. Gersh, M. D. McGoon, J. P. Whisnant, D. R. Holmes Jr, D. M. Ilstrup, and R. L. Frye, “The natural history of lone atrial fibrillation,” *New England Journal of Medicine*, vol. 317, no. 11, pp. 669–674, 1987.

- [23] Wikipedia, “Atrial fibrillation — Wikipedia, the free encyclopedia.” <http://en.wikipedia.org/w/index.php?title=Atrial%20fibrillation&oldid=1024767233>, 2021. [Online; accessed 26-May-2021].
- [24] H. Calkins, K. H. Kuck, R. Cappato, J. Brugada, A. J. Camm, S.-A. Chen, H. J. Crijns, R. J. Damiano Jr, D. W. Davies, J. DiMarco, *et al.*, “2012 hrs/ehra/ecas expert consensus statement on catheter and surgical ablation of atrial fibrillation: recommendations for patient selection, procedural techniques, patient management and follow-up, definitions, endpoints, and research trial design: a report of the heart rhythm society (hrs) task force on catheter and surgical ablation of atrial fibrillation. developed in partnership with the european heart rhythm association (ehra), a registered branch of the european society of cardiology (esc) and the european cardiac arrhythmia society (ecas); and in collaboration with the american college of cardiology (acc), american heart association (aha), the asia pacific heart rhythm society (aphrs), and the society of thoracic surgeons (sts). endorsed by the governing bodies of the american college of cardiology foundation, the american heart association, the european cardiac arrhythmia society, the european heart rhythm association, the society of thoracic surgeons, the asia pacific heart rhythm society, and the heart rhythm society,” *Europace*, vol. 14, no. 4, pp. 528–606, 2012.
- [25] L. F. Tops, M. J. Schalij, E. R. Holman, L. van Erven, E. E. van der Wall, and J. J. Bax, “Right ventricular pacing can induce ventricular dyssynchrony in patients with atrial fibrillation after atrioventricular node ablation,” *Journal of the American College of Cardiology*, vol. 48, no. 8, pp. 1642–1648, 2006.
- [26] H. Kottkamp, G. Hindricks, R. üdiger Autschbach, B. Krauss, B. Strasser, P. Schirdewahn, A. Fabricius, G. Schuler, and F.-W. Mohr, “Specific linear left atrial lesions in atrial fibrillation: intraoperative radiofrequency ablation using minimally invasive surgical techniques,” *Journal of the American College of Cardiology*, vol. 40, no. 3, pp. 475–480, 2002.
- [27] T. Ashihara, R. Haraguchi, K. Nakazawa, T. Namba, T. Ikeda, Y. Nakazawa, T. Ozawa, M. Ito, M. Horie, and N. A. Trayanova, “The role of fibroblasts in complex fractionated electrograms during persistent/permanent atrial fibrillation: implications for electrogram-based catheter ablation,” *Circulation research*, vol. 110, no. 2, pp. 275–284, 2012.
- [28] D. L. Donoho and J. M. Johnstone, “Ideal spatial adaptation by wavelet shrinkage,” *biometrika*, vol. 81, no. 3, pp. 425–455, 1994.
- [29] C. D. Cantwell, C. H. Roney, F. S. Ng, J. H. Siggers, S. Sherwin, and N. S. Peters, “Techniques for automated local activation time annotation and conduction velocity estimation in cardiac mapping,” *Computers in biology and medicine*, vol. 65, pp. 229–242, 2015.
- [30] C. Kik, E. M. Mouws, A. J. Bogers, and N. M. S. de Groot, “Intra-operative mapping of the atria: the first step towards individualization of atrial fibrillation therapy?,” *Expert review of cardiovascular therapy*, vol. 15, no. 7, pp. 537–545, 2017.

- [31] L. J. van der Does and N. M. de Groot, "Inhomogeneity and complexity in defining fractionated electrograms," *Heart rhythm*, vol. 14, no. 4, pp. 616–624, 2017.
- [32] K. Nademanee, J. McKenzie, E. Kosar, M. Schwab, B. Sunsaneewitayakul, T. Vasavakul, C. Khunnawat, and T. Ngarmukos, "A new approach for catheter ablation of atrial fibrillation: mapping of the electrophysiologic substrate," *Journal of the American College of Cardiology*, vol. 43, no. 11, pp. 2044–2053, 2004.
- [33] M. Courtemanche, R. J. Ramirez, and S. Nattel, "Ionic mechanisms underlying human atrial action potential properties: insights from a mathematical model," *American Journal of Physiology-Heart and Circulatory Physiology*, vol. 275, no. 1, pp. H301–H321, 1998.
- [34] M. S. Spach, W. T. Miller, P. C. Dolber, J. M. Kootsey, J. R. Sommer, and C. E. Mosher, "The functional role of structural complexities in the propagation of depolarization in the atrium of the dog. cardiac conduction disturbances due to discontinuities of effective axial resistivity.," *Circulation research*, vol. 50, no. 2, pp. 175–191, 1982.
- [35] P. C. Franzzone, L. Guerri, M. Pennacchio, and B. Taccardi, "Anisotropic mechanisms for multiphasic unipolar electrograms: simulation studies and experimental recordings," *Annals of biomedical engineering*, vol. 28, no. 11, pp. 1326–1342, 2000.
- [36] J. J. Rieta and F. Hornero, "Comparative study of methods for ventricular activity cancellation in atrial electrograms of atrial fibrillation," *Physiological measurement*, vol. 28, no. 8, p. 925, 2007.
- [37] S. Shkurovich, A. V. Sahakian, and S. Swiryn, "Detection of atrial activity from high-voltage leads of implantable ventricular defibrillators using a cancellation technique," *IEEE Transactions on Biomedical Engineering*, vol. 45, no. 2, pp. 229–234, 1998.
- [38] J. J. Rieta, F. Castells, C. Sánchez, V. Zarzoso, and J. Millet, "Atrial activity extraction for atrial fibrillation analysis using blind source separation," *IEEE Transactions on Biomedical Engineering*, vol. 51, no. 7, pp. 1176–1186, 2004.
- [39] A. Ahmad, J. Salinet, P. Brown, J. H. Tuan, P. Stafford, G. A. Ng, and F. S. Schlindwein, "Qrs subtraction for atrial electrograms: flat, linear and spline interpolations," *Medical & biological engineering & computing*, vol. 49, no. 11, pp. 1321–1328, 2011.
- [40] A. V. Oppenheim, *Discrete-time signal processing*. Pearson Education India, 1999.
- [41] Y. Hu, D. Zhang, J. Ye, X. Li, and X. He, "Fast and accurate matrix completion via truncated nuclear norm regularization," *IEEE transactions on pattern analysis and machine intelligence*, vol. 35, no. 9, pp. 2117–2130, 2013.
- [42] S. Boyd, N. Parikh, E. Chu, B. Peleato, J. Eckstein, *et al.*, "Distributed optimization and statistical learning via the alternating direction method of multipliers," *Foundations and Trends® in Machine learning*, vol. 3, no. 1, pp. 1–122, 2011.

- [43] Z. Xue, J. Dong, Y. Zhao, C. Liu, and R. Chellali, “Low-rank and sparse matrix decomposition via the truncated nuclear norm and a sparse regularizer,” *The Visual Computer*, pp. 1–18, 2018.
- [44] V. G. Fast and A. G. Kléber, “Role of wavefront curvature in propagation of cardiac impulse,” *Cardiovascular research*, vol. 33, no. 2, pp. 258–271, 1997.
- [45] F. M. Weber, A. Luik, C. Schilling, G. Seemann, M. W. Krueger, C. Lorenz, C. Schmitt, and O. Dossel, “Conduction velocity restitution of the human atrium—an efficient measurement protocol for clinical electrophysiological studies,” *IEEE Transactions on Biomedical Engineering*, vol. 58, no. 9, pp. 2648–2655, 2011.
- [46] M. W. Krueger, K. S. Rhode, M. D. O’Neill, C. A. Rinaldi, J. Gill, R. Razavi, G. Seemann, and O. Doessel, “Patient-specific modeling of atrial fibrosis increases the accuracy of sinus rhythm simulations and may explain maintenance of atrial fibrillation,” *Journal of electrocardiology*, vol. 47, no. 3, pp. 324–328, 2014.
- [47] C. H. Roney, J. D. Bayer, S. Zahid, M. Meo, P. M. Boyle, N. A. Trayanova, M. Haïssaguerre, R. Dubois, H. Cochet, and E. J. Vigmond, “Modelling methodology of atrial fibrosis affects rotor dynamics and electrograms,” *EP Europace*, vol. 18, no. suppl\_4, pp. iv146–iv155, 2016.
- [48] E. Gilboa, P. S. La Rosa, and A. Nehorai, “Estimating electrical conductivity tensors of biological tissues using microelectrode arrays,” *Annals of biomedical engineering*, vol. 40, no. 10, pp. 2140–2155, 2012.
- [49] A. J. Pullan, K. A. Tomlinson, and P. J. Hunter, “A finite element method for an eikonal equation model of myocardial excitation wavefront propagation,” *SIAM Journal on Applied Mathematics*, vol. 63, no. 1, pp. 324–350, 2002.
- [50] P. Chinchapatnam, K. S. Rhode, M. Ginks, C. A. Rinaldi, P. Lambiase, R. Razavi, S. Arridge, and M. Sermesant, “Model-based imaging of cardiac apparent conductivity and local conduction velocity for diagnosis and planning of therapy,” *IEEE Transactions on Medical Imaging*, vol. 27, no. 11, pp. 1631–1642, 2008.
- [51] T. Goldstein and S. Osher, “The split bregman method for l1-regularized problems,” *SIAM journal on imaging sciences*, vol. 2, no. 2, pp. 323–343, 2009.
- [52] A. Gogna, A. Shukla, H. Agarwal, and A. Majumdar, “Split Bregman algorithms for sparse/joint-sparse and low-rank signal recovery: application in compressive hyperspectral imaging,” in *Image Processing (ICIP), 2014 IEEE International Conference on*, pp. 1302–1306, IEEE, 2014.
- [53] G. Salama, A. Kanai, and I. R. Efimov, “Subthreshold stimulation of purkinje fibers interrupts ventricular tachycardia in intact hearts. experimental study with voltage-sensitive dyes and imaging techniques.,” *Circulation research*, vol. 74, no. 4, pp. 604–619, 1994.

- 7
- [54] E. A. Lanters, A. Yaksh, C. P. Teuwen, L. J. van der Does, C. Kik, P. Knops, D. M. van Marion, B. J. Brundel, A. J. Bogers, M. A. Allessie, *et al.*, “Spatial distribution of conduction disorders during sinus rhythm,” *International journal of cardiology*, vol. 249, pp. 220–225, 2017.
  - [55] I. Chouvarda, N. Maglaveras, J. M. de Bakker, F. J. van Capelle, and C. Pappas, “Deconvolution and wavelet-based methods for membrane current estimation from simulated fractionated electrograms,” *IEEE transactions on biomedical engineering*, vol. 48, no. 3, pp. 294–301, 2001.
  - [56] M. S. Spach and P. C. Dolber, “Relating extracellular potentials and their derivatives to anisotropic propagation at a microscopic level in human cardiac muscle. evidence for electrical uncoupling of side-to-side fiber connections with increasing age.,” *Circulation research*, vol. 58, no. 3, pp. 356–371, 1986.
  - [57] B. Abdi, R. C. Hendriks, A.-J. van der Veen, and N. M. de Groot, “A compact matrix model for atrial electrograms for tissue conductivity estimation,” *Computers in biology and medicine*, vol. 107, pp. 284–291, 2019.
  - [58] E. J. Ciaccio, A. B. Biviano, W. Whang, A. Gambhir, and H. Garan, “Different characteristics of complex fractionated atrial electrograms in acute paroxysmal versus long-standing persistent atrial fibrillation,” *Heart Rhythm*, vol. 7, no. 9, pp. 1207–1215, 2010.
  - [59] S. M. Narayan, M. Wright, N. Derval, A. Jadidi, A. Forclaz, I. Nault, S. Miyazaki, F. Sacher, P. Bordachar, J. Clémenty, *et al.*, “Classifying fractionated electrograms in human atrial fibrillation using monophasic action potentials and activation mapping: evidence for localized drivers, rate acceleration, and nonlocal signal etiologies,” *Heart Rhythm*, vol. 8, no. 2, pp. 244–253, 2011.
  - [60] W. S. Ellis, S. J. Eisenberg, D. M. Auslander, M. W. Dae, A. Zakhor, and M. D. Lesh, “Deconvolution: A novel signal processing approach for determining activation time from fractionated electrograms and detecting infarcted tissue,” *Circulation*, vol. 94, no. 10, pp. 2633–2640, 1996.
  - [61] A. N. Tikhonov, A. Goncharsky, V. Stepanov, and A. G. Yagola, *Numerical methods for the solution of ill-posed problems*, vol. 328. Springer Science & Business Media, 2013.
  - [62] B. Abdi, R. C. Hendriks, A.-J. van der Veen, and N. M. de Groot, “Local activation time annotation in atrial electrogram arrays using deconvolution,” in *2019 Computing in Cardiology (CinC)*, pp. 1–4, IEEE, 2019.
  - [63] V. Jacquemet and C. S. Henriquez, “Genesis of complex fractionated atrial electrograms in zones of slow conduction: a computer model of microfibrosis,” *Heart rhythm*, vol. 6, no. 6, pp. 803–810, 2009.
  - [64] E. Vigmond, A. Pashaei, S. Amraoui, H. Cochet, and M. Hassaguerre, “Percolation as a mechanism to explain atrial fractionated electrograms and reentry in a fibrosis model based on imaging data,” *Heart rhythm*, vol. 13, no. 7, pp. 1536–1543, 2016.

- [65] B. B. Puniske, Q. Ni, R. L. Lux, R. S. MacLeod, P. R. Ershler, T. J. Dustman, M. J. Allison, and B. Taccardi, “Spatial methods of epicardial activation time determination in normal hearts,” *Annals of biomedical engineering*, vol. 31, no. 7, pp. 781–792, 2003.
- [66] J. M. Stinnett-Donnelly, N. Thompson, N. Habel, V. Petrov-Kondratov, D. D. C. de Sa, J. H. Bates, and P. S. Spector, “Effects of electrode size and spacing on the resolution of intracardiac electrograms,” *Coronary artery disease*, vol. 23, no. 2, pp. 126–132, 2012.
- [67] N. C. Thompson, J. Stinnett-Donnelly, N. Habel, B. Benson, J. H. Bates, B. E. Sobel, and P. S. Spector, “Improved spatial resolution and electrogram wave direction independence with the use of an orthogonal electrode configuration,” *Journal of clinical monitoring and computing*, vol. 28, no. 2, pp. 157–163, 2014.
- [68] R. Mizutani, R. Saiga, S. Takekoshi, C. Inomoto, N. Nakamura, M. Itokawa, M. Arai, K. Oshima, A. Takeuchi, K. Uesugi, *et al.*, “A method for estimating spatial resolution of real image in the fourier domain,” *Journal of microscopy*, vol. 261, no. 1, pp. 57–66, 2016.
- [69] T. F. Chan and C.-K. Wong, “Total variation blind deconvolution,” *IEEE transactions on Image Processing*, vol. 7, no. 3, pp. 370–375, 1998.
- [70] K. Anderson, R. Walker, P. Ershler, M. Fuller, T. Dustman, R. Menlove, S. Karwandee, and R. Lux, “Determination of local myocardial electrical activation for activation sequence mapping. a statistical approach,” *Circulation research*, vol. 69, no. 4, pp. 898–917, 1991.
- [71] J. M. De Bakker and F. H. Wittkampf, “The pathophysiologic basis of fractionated and complex electrograms and the impact of recording techniques on their detection and interpretation,” *Circulation: Arrhythmia and Electrophysiology*, vol. 3, no. 2, pp. 204–213, 2010.
- [72] K. T. Konings, J. L. Smeets, O. C. Penn, H. J. Wellens, and M. A. Allessie, “Configuration of unipolar atrial electrograms during electrically induced atrial fibrillation in humans,” *Circulation*, vol. 95, no. 5, pp. 1231–1241, 1997.
- [73] J. M. de Bakker, “Electrogram recording and analyzing techniques to optimize selection of target sites for ablation of cardiac arrhythmias,” *Pacing and Clinical Electrophysiology*, vol. 42, no. 12, pp. 1503–1516, 2019.
- [74] E. Anter, C. M. Tschabrunn, and M. E. Josephson, “High-resolution mapping of scar-related atrial arrhythmias using smaller electrodes with closer interelectrode spacing,” *Circulation: Arrhythmia and Electrophysiology*, vol. 8, no. 3, pp. 537–545, 2015.
- [75] M. Hwang, J. Kim, B. Lim, J.-S. Song, B. Joung, E. B. Shim, and H.-N. Pak, “Multiple factors influence the morphology of the bipolar electrogram: An in silico modeling study,” *PLoS computational biology*, vol. 15, no. 4, p. e1006765, 2019.

- [76] C.-Y. Lin, A. L. D. Te, Y.-J. Lin, S.-L. Chang, L.-W. Lo, Y.-F. Hu, F.-P. Chung, T.-C. Tuan, T.-F. Chao, J.-N. Liao, *et al.*, “High-resolution mapping of pulmonary vein potentials improved the successful pulmonary vein isolation using small electrodes and inter-electrode spacing catheter,” *International journal of cardiology*, vol. 272, pp. 90–96, 2018.
- [77] M. Huemer, D. Qaiyumi, P. Attanasio, A. Parwani, B. Pieske, F. Blaschke, L.-H. Boldt, W. Haverkamp, and A. Wutzler, “Does the extent of left atrial arrhythmogenic substrate depend on the electroanatomical mapping technique: impact of pulmonary vein mapping catheter vs. ablation catheter,” *Ep Europace*, vol. 19, no. 8, pp. 1293–1301, 2017.
- [78] M. Andronache, N. Drca, and G. Viola, “High-resolution mapping in patients with persistent af,” *Arrhythmia & electrophysiology review*, vol. 8, no. 2, p. 111, 2019.
- [79] D. D. Correa de Sa, N. Thompson, J. Stinnett-Donnelly, P. Znojkievicz, N. Habel, J. G. Müller, J. H. Bates, J. S. Buzas, and P. S. Spector, “Electrogram fractionation: the relationship between spatiotemporal variation of tissue excitation and electrode spatial resolution,” *Circulation: Arrhythmia and Electrophysiology*, vol. 4, no. 6, pp. 909–916, 2011.
- [80] P. R. Rocha, P. Schlett, U. Kintzel, V. Mailänder, L. K. Vandamme, G. Zeck, H. L. Gomes, F. Biscarini, and D. M. De Leeuw, “Electrochemical noise and impedance of au electrode/electrolyte interfaces enabling extracellular detection of glioma cell populations,” *Scientific reports*, vol. 6, p. 34843, 2016.
- [81] J. J. Wiley, R. E. Ideker, W. M. Smith, and A. E. Pollard, “Measuring surface potential components necessary for transmembrane current computation using microfabricated arrays,” *American Journal of Physiology-Heart and Circulatory Physiology*, vol. 289, no. 6, pp. H2468–H2477, 2005.
- [82] E. A. Lanters, D. M. van Marion, C. Kik, H. Steen, A. J. Bogers, M. A. Allessie, B. J. Brundel, and N. M. de Groot, “Halt & reverse: Hsf1 activators lower cardiomyocyt damage; towards a novel approach to reverse atrial fibrillation,” *Journal of translational medicine*, vol. 13, no. 1, p. 347, 2015.
- [83] L. J. van der Does, A. Yaksh, C. Kik, P. Knops, E. A. Lanters, C. P. Teuwen, F. B. Oei, P. C. van de Woestijne, J. A. Bekkers, A. J. Bogers, *et al.*, “Quest for the arrhythmogenic substrate of atrial fibrillation in patients undergoing cardiac surgery (quasar study): rationale and design,” *Journal of cardiovascular translational research*, vol. 9, no. 3, pp. 194–201, 2016.
- [84] E. M. Mouws, E. A. Lanters, C. P. Teuwen, L. J. van der Does, C. Kik, P. Knops, J. A. Bekkers, A. J. Bogers, and N. M. de Groot, “Epicardial breakthrough waves during sinus rhythm: depiction of the arrhythmogenic substrate?,” *Circulation: Arrhythmia and Electrophysiology*, vol. 10, no. 9, p. e005145, 2017.

- [85] C. P. Teuwen, A. Yaksh, E. A. Lanters, C. Kik, L. J. van der Does, P. Knops, Y. J. Taverne, P. C. van de Woestijne, F. B. Oei, J. A. Bekkers, *et al.*, “Relevance of conduction disorders in bachmann’s bundle during sinus rhythm in humans,” *Circulation: Arrhythmia and Electrophysiology*, vol. 9, no. 5, p. e003972, 2016.
- [86] M. S. van Schie, R. Starreveld, A. J. Bogers, and N. de Groot, “Sinus rhythm voltage fingerprinting in patients with mitral valve disease using a high-density epicardial mapping approach,” *EP Europace*, 2021.



# ACKNOWLEDGEMENTS

I take this opportunity to express my deepest gratitude to my colleagues, family, and friends without whom this work would not have been possible.

First, I would like to thank my supervisors Prof. Alle-Jan van der Veen, Dr. Richard Hendriks, and Prof. Natasja de Groot. Thank you for giving me the opportunity to contribute to this interesting project. You gave me the freedom and the trust to choose the direction of this project and supported me in my work while providing valuable guidance, constructive criticism, and suggestions. I would also like to thank the remaining members of the circuits and systems (CAS) group in TU Delft and the Cardiology Department in Erasmus MC, who made this a pleasurable experience and provided me with valuable help and feedback during my work. I also thank all the jury members for their time and effort spent to evaluate this thesis. And finally, thanks to my new group, EEE, for providing the friendly environment during the writing of this thesis. I look forward to our growth together.

Next, I would like to thank my parents, Eghbal and Shahla, and my brother Behzad. Thank you for your unconditional love, your sacrifices, and your high hopes for me. It would not have been possible for me to be where I am now without you. And I would also like to thank my dear husband, Aydin. I have always had your love, friendship, and support for the last 10 years, both as a colleague and as my only family here in the Netherlands. We have come a long way together, and it was mostly just the two of us, but you never let me feel lonely. You were there for me when I was feeling helpless and miserable, and you were there for me at the time of success and celebration. Thanks for being so thoughtful and reliable and for all the compromises you made in the way. Thank you, hubby!

Finally, many thanks to our Iranian friends who made us feel at home far from home. Elahe and Mehrdad, we started this journey together and you always step in to help us when we need it the most, thank you! Samira, Hanieh and Negin, when I think about things that I'm grateful for, you are always on the list. Jamal, Sina, Ghazaleh and Nima you made our life more enjoyable! Also, many thanks to Bahar, Saleh, Mohsen, Milad, Hoda, Bijan, Hanie for the wonderful memories we made together.



# CURRICULUM VITÆ



**Bahareh Abdi** was born in Tehran, Iran, in 1990. She obtained her B.Sc. in electrical engineering in 2012, and her M.Sc. in biomedical engineering in 2015, both from the University of Tehran. From 2010 till 2015, she was working as a part-time physics teacher. She then worked as an intern in the center of advance (CAS) science group in IBM, Amsterdam, in 2016. She started as a Ph.D. student in Technische Universiteit Delft in December 2016, working in a joint project between the Circuits and Systems group of the EEMCS faculty, and the Cardiology Department in Erasmus Medical Center. In her project, she focused on developing signal processing algorithms for analysing heart electrical activity for the early recognition of atrial fibrillation. She is currently working as a principal educator in the electrical engineering education group in TU Delft. Her research interests include biological signal and image processing, machine learning, system Identification and Modelling.